Fault slip-rates and Coulomb stress interactions in the intersection zone of the Hope, Kelly and Alpine Faults, South Island, New Zealand

Jessie L. Vermeer* [a], Mark C. Quigley [a], Robert R. Langridge [c], Brendan G. Duffy [a,b], Zoë K. Mildon [d], Manuel-Lukas Diercks [d]

* Corresponding author: JVermeer@student.unimelb.edu.au

[a] University of Melbourne, School of Geography, Earth and Atmospheric Sciences, Parkville, Victoria 3010, Australia

[b] GHD Pty Ltd, 180 Lonsdale Street, Melbourne, Victoria 3000, Australia

[c] GNS Science, Lower Hutt, New Zealand

[d] University of Plymouth, Plymouth, Devon, PL4 8AA, United Kingdom

This is a non-peer reviewed manuscript submitted to EarthArXiv. The manuscript has been submitted to *Tectonophysics*.

Abstract

The Hope Fault is a major strike-slip plate boundary fault in the Marlborough Fault Zone of New Zealand's South Island that transfers slip between the Alpine Fault and Hikurangi subduction zone. We use lidar-based geomorphic and fault mapping, and optically stimulated luminescence (OSL; quartz) and infrared stimulated luminescence (IRSL; feldspar) dating of fault-proximal sedimentary deposits to constrain post-last glacial slip-rates for the Taramakau section of the Hope Fault and the Kelly Fault. Dextral slip-rates on the central Hope Fault (12-15 mm/yr) decrease westward from 5.6 (+2.0/-0.8) mm/yr to 1.7 (+1.0/-0.5) mm/yr. Dextral slip-rates on the Kelly Fault range from 6.2 (+7.6/-1.4) mm/yr to 1.7 (+2.1/-0.4) mm/yr. Linking, incipient subsidiary faults have minimum slip-rates of 1.3 (+0.1/-0.4) mm/yr. Proposed causes of spatial variations in slip-rates include (i) complexities in diffusive slip localization and transfer across the deformation zone, (ii) undocumented slip on faults including buried or otherwise unrecognized traces, and (iii) possible transience in slip behaviours. Paleoseismic trenching and radiocarbon (^{14}C) ages are used to constrain the timing of most recent surface rupture on the western Hope Fault (Taramakau section) to ca. 1680 and 1840 CE, with a preferred age of ca. 1800-1840 CE. Coulomb stress modelling of scenario earthquakes on individual faults in the Alpine-Hope-Kelly Fault network is used to explore physical drivers for understanding slip-rate variations across the network. Source fault ruptures on the central Alpine Fault impart positive stress changes on the Hope-Kelly receiver faults in excess of 5-10 bars, and vice versa. Northern Alpine Fault earthquakes reduce Coulomb stresses on the Hope-Kelly receiver faults, and vice versa. Earthquake spatio-temporal clustering is an important consideration in evaluating earthquake hazards in this region.

Keywords: Alpine fault, Hope fault, slip-rate, Coulomb stress modeling, fault intersection zone

1. Introduction

Fault slip-rates are important parameters in evaluating earthquake spatio-temporal patterns (e.g., Langridge et al., 2017; Elliot et al., 2018; Zinke et al., 2019; Zinke et al., 2021; Hatem et al., 2020) and undertaking probabilistic seismic hazard and fault displacement hazard analyses (e.g., Stirling et al., 2012; Moss and Ross, 2011). Continental plate boundaries commonly include hierarchical networks of large, fast-slipping (>10 mm yr-1) faults and secondary, slower-slipping (ca. 1-10 mm yr-1) faults that interact to accommodate tectonic strain transfer. Faults may exhibit significant slip-rate variations in time (Gold and Cowgill, 2011) that reflect a variety of factors including stress shadowing (e.g., Nicol et al., 2006; Khajavi et al., 2018; Ninis et al., 2013, Gauriau and Dolan, 2021), temporal changes in fault strength (e.g. Dolan et al., 2016), and temporal earthquake clustering (e.g. Rockwell et al., 2000; Dolan et al, 2007). Derivation of fault slip-rates, faulting kinematics, and earthquake chronologies across diverse time-scales provide opportunities to advance our understanding of the nature and mechanics of fault interactions in plate boundaries.

The geometric connectivity of interacting faults within a fault network can impart important controls on how slip is transferred through the fault system in individual earthquakes (i.e., coseismic rupture propagation) and over geological time-scales incorporating many diverse earthquake scenarios (e.g., Parsons et al., 2012; Quigley et al., 2019). Although the timing of earthquakes on individual faults inferred from paleoseismic data may be used to investigate earthquake spatial-temporal clustering via fault interaction, for fast-slipping faults with short

recurrence intervals, it may often be difficult to discriminate between clustered events with a common underlying causal mechanism from random earthquake events, particularly if the timing of past earthquakes is not precisely constrained. This is important to resolve in seismic hazard analysis because (i) co-seismic rupture propagation across many faults can increase the moment magnitude (Mw) of the earthquake and (ii) stress transfer across diverse faults in a network may influence the subsequent hazard following a major earthquake, and the longer-term hazard associated with fault slip-rate variability. Modelling of Coulomb stress changes imparted by earthquake source faults on receiver faults within a fault network can provide important insights into how the structure of a fault network may promote or inhibit various rupture scenarios amongst proximate faults (e.g., Parsons et al., 2012; Quigley et al., 2019; Mohammadi et al., 2019).

The Marlborough Fault System (MFS) in the northern South Island (Figure 1) consists of a series of large dextral strike-slip faults and interspersed secondary faults that transfer plate boundary strain from the Hikurangi subduction zone through to the Alpine Fault (Van Dissen and Yeats, 1991; Barnes and Audru, 1999; Norris and Cooper, 2001; Langridge et al., 2010; Langridge et al., 2003; Yang, 1991; Khajavi et al., 2016; Cowan and McGlone, 1991; Cowan, 1990; Khajavi et al., 2018; Langridge and Berryman, 2005). This study focuses on a particularly structurally complex region of the MFS, where the southernmost and fastest-slipping fault in the MFS (Hope Fault, 12-23 mm/yr, see references in Figure 1) diverges from a principal fault trace into several interacting splay faults (Vermeer et al., 2021). The primary objective is to obtain new fault slip-rate data from a sparsely-studied area of the MFS to compare with emerging datasets from other parts of the MFS (Khajavi et al., 2018; Hatem et al., 2020; Zinke et al., 2021) and the Alpine Fault (Langridge et al., 2017; Howarth et al., 2018, 2021) to enhance our understanding of the rates and mechanics of Late Quaternary faulting in this region. Using a combined approach of structural-

geomorphic mapping, dating of fault-associated sediments and landforms, and Coulomb stress modelling scenarios, we characterise earthquake behaviours and fault interactions in this incipient plate boundary fault interaction zone. The results are relevant to understanding seismic hazard (Stirling et al., 2012) and faulting in this region (e.g., Litchfield et al., 2014; Langridge et al., 2016) and analogous regions globally.

2. Geologic Setting

The northern South Island of New Zealand straddles a section of the Australian-Pacific plate boundary where the main structures are the Alpine Fault and the Marlborough Fault System (MFS). These dextral strike-slip fault zones host approximately 80% of the total AUS-PAC relative plate velocity (Figure 1; Norris and Cooper, 2001; Sutherland et al., 2007; Wallace et al., 2007; Barth et al., 2013; Howarth et al., 2018). The NE-striking Alpine Fault extends along the west side of the South Island and is a dextral-reverse fault with a straight surface trace and moderate to shallow south-eastward dip (Berryman et al., 1992; Norris and Cooper, 2001; Barth et al., 2013; Howarth et al., 2018). Slip-rates vary along its length. The central section has a maximum of 28 ±4 mm/yr dextral and up to >12 mm/yr of reverse slip and northern section has a slip rate that decreases from 14 ±2 mm/yr at the southern end to 10 ±2 mm/yr at the northern end (Norris and Cooper, 2001; Langridge et al., 2010; Langridge et al., 2017; Howarth et al., 2018). The Hope Fault is the southernmost fault in the MFS. It extends from the central-northern section boundary of the Alpine Fault to the NE coast of the South Island where it interacts with the Hikurangi subduction zone (Nicol and Van Dissen, 2002; Langridge and Berryman, 2005; Barth et al., 2013). The ENE-striking Hope Fault is primarily dextral slip and is divided into five geometric segments with two branching faults (the Kakapo and the Kelly) and one large stepover (Hanmer Basin) (Figure 1) (Freund, 1971; Langridge and Berryman, 2005). The slip-rate varies

along the fault (Figure 1 and references therein). Balancing the horizontal slip vector shows that the central Hope Fault (Hurunui segment plus Kakapo fault) accommodates the same amount and direction of slip as the decrease on Alpine Fault at the central-northern transition (Langridge et al., 2010). The slip transfers between the Alpine and Hope Faults via the Hope-Kelly Fault system, made of the Taramakau section of the Hope Fault, the branching Kelly Fault, and all intervening faults. The Hope-Kelly Fault system is a horsetail like structure of north dipping dextral-normal oblique faults and south dipping normal faults that abut the Alpine Fault on the west side and converge eastward into the narrow dextral fault zone of the central Hope Fault (Vermeer et al., 2021).

The rupture record of the Alpine Fault is well known from on- and off-fault paleoseismic studies (De Pascale et al., 2014; Howarth et al., 2018 and studies therein), that define a recurrence interval of less than 300 years (Howarth et al., 2021; Cochran et al., 2017). Nevertheless, the Alpine Fault has not had a historic surface rupture (i.e., since c. 1840 CE). Paleoseismic studies indicate that in about 1717 CE the Alpine Fault hosted a very large to great (M >8) earthquake that ruptured the southern, central, and part of the northern segment (Wells et al., 1999; Howarth et al., 2018). At the central-northern section boundary a more recent faulting event has been identified as occurring in 1813-1840, shortly before the historic period (Langridge et al., 2021). This event is co-temporal with a turbidite in Lake Kaniere (Howarth et al., 2021), but not in Lake Brunner or lakes to the south , suggesting that this earthquake may have involved only a small length of the Alpine Fault.

The Hope Fault has had one historic surface rupturing earthquake, the Mw ~7.1 Amuri earthquake in 1888 CE, the extent of which is shown in Figure 1 (McKay, 1890; Khajavi et al., 2016). The eastern sections of the Hope Fault did not have surface rupture in the 2016 Kaikoura

earthquake (Litchfield et al., 2018). The dates of the most recent surface rupture and the penultimate surface rupture at paleoseismic sites on the Hope Fault to date are shown in Figure 1. There has been no previous paleoseismic data for the Taramakau section or the Kelly Fault.

Vermeer et al. (2021) recently studied the Hope and Kelly Faults west of the Main Divide using lidar and field mapping of surrounding landforms. They identified sections of principal slip zones along the faults, where individual fault traces have accumulated displacement from multiple surface ruptures. In this study, we examine some of these PSZ fault scarps in more detail, present OSL and radiocarbon ages for some landforms from hand-dug pits and outcrops, conduct paleoseismic investigations, and determine slip-rates.

The most recent glaciation in New Zealand, the Otiran glaciation, occurred during MIS stages 2-4 with up to 8 glacial advances identified during that time (Shulmeister et al., 2019). The Taramakau glacier had three advances during the glacial interval 26-17 ka (Barrell et al., 2011; Barrows et al., 2013). The oldest MIS-2 advance of the Taramakau glacier is 24.9 ± 0.8 ka (Figure 2 Kumara-2_1 advance, Loopline Formation moraine, Barrell et al., 2011; Barrows et al., 2013). East of the Main Divide, downvalley glacial deposits in the Waimakariri River valley are as old as 26 ka (Rother et al., 2015), indicating the upper parts of the Taramakau Valley were probably also glaciated by that time. The Kumara-2_1 advance was followed by a short recession with an unknown amount of glacial retreat, and a readvance at 20.8-20 ka (Figure 2 Kumara-2_2 advance, Larrikins Formation moraine, Barrell et al., 2011; Barrows et al., 2013). Glaciofluvial sediments in the Rangitata valley (20-26 ka, Shulmeister et al., 2018), fluvial sand in Otago (24.8 ±2.7 ka, Stahl et al., 2016), outwash sediments in the Grey River valley (21.3-23.9 ka, Hormes et al., 2003), and alluvial sediments in the Hope River valley (23.9 ±1.5 ka, Khajavi et al., 2016), indicating a regional pulse of outwash/alluvial sedimentation between the 26-24 ka advance and the ~20 ka

advance in catchments surrounding the Taramakau River. The latest ice deposited features on the coastal plain are Moana Formation moraines (Kumara-3, Barrell et al., 2011; Barrows et al., 2013), dated at 17.3 ±0.5 ka at Lake Brunner, indicating at that time the Taramakau River valley and tributary catchments (Otira and Otehake rivers) were fully glaciated. End moraines at Arthurs Pass are 15.2 ± 0.8 ka (Eaves et al., 2017). The sites of interest in this study are all well below the elevation of the Arthurs Pass end moraines, so by inference they were ice-free before 15.2 ±0.8 ka. Thus, the last deglaciation of the Taramakau River valley occurred no earlier than 17.3 ±0.5 ka and was complete by 15.2 ±0.8 ka.

3. Fault slip-rates and site investigations

3.1. Methods

3.1.1. Lidar and field based site mapping and interpretation

The investigations and measurements presented in this paper are primarily based on analysis of lidar-derived bare-earth DEMs and field verification. This study expands on the work presented in Vermeer et al. (2021). The lidar was flown in September 2015 by AAM (http://www.aamgroup.com/) using a Riegl Q1560 at 390-400 kHz pulse rate. Vertical accuracy of the ground points is ±0.15 m and horizontal accuracy is ±0.50 m with laser footprint size 0.24-0.39 m. The data was delivered as LAS datasets classified as ground and non-ground returns; classification was completed by AAM using algorithms appropriate for the vegetation type then manually checked. The DEMs were produced using nearest neighbour interpolation of the ground classified points. Suitable grid size was determined using the formula in Langridge et al. (2014): *"s = sqrt(A/n) where s is the cell size, n is the number of sample points and A is the area containing the sample points.*" For all sites presented here, the lidar data was of suitable point density to grid at 0.5 m with the exception of blank spots where large (1+ m diameter) trees were standing which

produce some artifacts in the DEMs. Terrain analysis of the bare earth DEMs was done using ESRI ArcMap by producing slope, aspect, hillshade and contour maps.

Detailed geomorphic mapping reveals surfaces and features such as alluvial terraces, alluvial fans, landslides, and faults that cut and displace these features. The geomorphic mapping does not necessarily indicate the origin of the underlying substrate (i.e., a terrace may be underlain by accumulated alluvial sediment or bedrock if it is a strath terrace), which was determined in critical locations by field observation of local stratigraphy in natural exposures, pits and trenches. The mapping and stratigraphy, combined with absolute age control described below, was used to determine the sequence of events which produced the present morphology of each site. Geomorphic surfaces are numbered in the order of formation, so the oldest identified surface is "1" and the numbers increase with decreasing age. The sequence of erosional and depositional events interpreted from the surface morphology and stratigraphy is referred to as a geomorphic formation timeline. Timelines are used to understand the formation, significance, and uncertainty of features that are dated, and how they relate to features that are displaced by the faults. By combining the geomorphic development timelines, fault displacement, and absolute dating of surfaces we calculated slip-rates for the faults.

3.1.2 Displacement measurements

3.1.2.1 Horizontal displacement

To measure lateral displacements, we identified correlative landscape features spanning fault traces (following Cowgill, 2007; Zielke et al., 2015; Khajavi et al., 2016; Mackenzie and Elliott, 2017; Zinke et al., 2017; Khajavi et al., 2018; Zielke 2018; Zinke et al., 2021) from DEMs and derivatives, 2D topographic profiles, and 3D inspection of the ground classified point clouds.

Features that do not directly intersect the fault scarp were projected to the edge of the scarp accounting for a range of possible geometries, based on the geometry of the observed feature. Displacement measurements were made parallel to the strike of the fault. Preferred displacements are based on offsets from preferred projections on each side, minimum displacements are the distance between the most proximate projections on each side of the fault, and maximums are the furthest projections. If the local trace of the fault crosses moderate to steep topography, the strike of the fault is determined using either 3-point problem or by fitting a 3D plane to the fault trace in Leapfrog Geo.

3.1.2.2 Vertical displacement

Vertical displacements are measured using scarp parallel topographic profiles to match geomorphic surfaces and features across the fault (e.g., Khajavi et al., 2016). In many cases, the fault parallel profiles are set back from the fault trace to avoid scarp degradation and scarp-proximate deposition and to capture the shape of pre-faulting landforms. On sloped landscapes, the horizontal distance between fault parallel profiles means there is an expected amount of elevation difference between the profiles; this is the expected vertical offset of the profiles. Fault-perpendicular topographic profiles are used to determine the pre-faulting landform slope and calculate the expected pre-faulting vertical offset of the scarp parallel profiles. Graphical shifting (i.e., restoration) of the fault parallel profiles is undertaken to evaluate how they match and to determine the present elevations of correlative features on each profile to find the actual vertical offset of the profiles. The difference between the expected vertical offset and the actual vertical offset of the profiles is the vertical displacement of the fault.

3.1.3 Trenching and outcrop investigations

A hand dug trench (Figure 2 site 1) was excavated across the fault where a discrete fault scarp and local geomorphic environment was favourable for potential preservation of faulted stratigraphy. As opportunities presented, favourable natural outcrops that exposed faulting and stratigraphy were investigated and analysed.

3.1.4 OSL/IRSL sediment sampling Methods

OSL/IRSL samples were obtained from excavated and cleaned outcrops, trench walls, and pits to determine the depositional age of sediments in the study sites. Samples were obtained using opaque metal tubes (5cm diameter, 15cm long) hammered into cleaned sediment faces and capped with light-impermeable foil and black tape. Samples were analysed by the Nordic Laboratory for Luminescence Dating at Aarhus University and DTU Physics in Denmark, following the method of Sohbati et al. (2016) for OSL, IR50 and pIRIR. The quartz OSL age is used as the absolute age for the sediment deposition. IR50 and pIRIR ages are used to evaluate the bleaching characteristics of the sediment, as described in the next section.

3.1.5 Background and theoretical framework for understanding uncertainty with OSL/IRSL luminescence ages

Quartz from the New Zealand Southern Alps west of the Main Divide commonly exhibits dim luminescence signals that may be manifested as decreased precision in OSL measurements (Preusser et al., 2006). These authors suggested that Westland quartz may be unsuitable for luminescence dating; samples sourced from west of the Alpine Fault were from the schistose rocks exposed within ~10-15 km east of the Alpine Fault. However, the majority of the samples are located >10 km from the Alpine Fault and the provenance of the sediment is from greywacke rocks in the Rakaia terrane, part of the Torlesse composite terrane. Greywacke-sourced sediment has

been used successfully in other studies from alluvial settings on the eastern side of the Southern Alps, especially when the samples were chosen carefully from ice-distal, fluvial or aeolian depositional environments (e.g., Hormes et al., 2003; Sohbati et al., 2016; Khajavi et al., 2016; Shulmeister et al., 2018). Feldspar IRSL has also been used commonly in the South Island of New Zealand to date glacial and interglacial deposits, but the age determinations are generally less precise than quartz OSL (Rother et al., 2006; 2010; Rowan et al., 2012; Stahl et al., 2016; Zinke et al., 2017).

In the study area, the depositional characteristics of the sediments sampled for OSL were difficult to assess due to extensive weathering and/or small exposure size. The likelihood that the quartz OSL age was well-bleached and the resulting age is representative of deposition is evaluated using the ratio of the OSL age to two components of feldspar IRSL age (Sohbati et al., 2016; Murray et al., 2012). Feldspar IR50 signals are more difficult to reset than OSL, and experiences loss of charge over time (anomalous fading), so if both quartz and IR50 were fully reset, IR50 will return a younger age than the quartz OSL (IR50/OSL $\leq$1) (Shobati et al., 2016; Murray et al., 2012). Feldspar pIRIR signal is the most difficult to bleach, requiring the most time in the highest intensity sunlight to be fully reset. pIRIR is also resistant to fading but yields less precise ages than quartz OSL. If the quartz OSL age and the feldspar pIRIR age are similar (pIRIR/OSL $\approx$1) it provides confidence that the quartz is fully reset and giving an accurate age for sediment deposition (Shobati et al., 2016; Murray et al., 2012). Because quartz is the easier mineral to reset, if the quartz OSL age is less than both the feldspar IR50 and pIRIR, it may or may not have been fully bleached prior to the last depositional event, so the measured age may overestimate the age of the deposit. Incomplete bleaching will not cause underestimation of the deposit age.

3.1.6 Radiocarbon sediment ages

Radiocarbon dating (^{14}C) of organic material in sediments is used to constrain their depositional age using the Southern Hemisphere calibration model of Hogg et al. (2020). Radiocarbon analysis was undertaken at the GNS Science Rafter Radiocarbon Lab in New Zealand. The measurements were conducted using Accelerator Mass Spectrometry. We selected samples with a preference for material that is clearly detrital, such as seeds, leaves or charcoal. Charcoal may have significant inherited age, making it less desirable than seeds or leaves (Howarth et al., 2013). Twigs may be detrital but may not be readily distinguishable from rootlets that could be significantly younger than the age of the sediment. The precision of radiocarbon ages is largely dependent on the shape of the radiocarbon calibration curve; when the calibration curve is very flat, a radiocarbon measured age can have a wide range in calibrated age. Ages that fall in these ranges when the calibration curve is flat can have precision increased by modelling multiple ages in OxCal with a stratigraphic order which shaves the age ranges using bayesian statistics (Biasi et al., 2002; Ramsey, 2009). However, if there are no other ages with stratigraphic context or other constraints, there is no way to decrease the calibrated age range of a ^{14}C sample.

3.1.7 Slip-rate calculations

Slip-rates were estimated using displacements, relative geomorphic ages, and absolute ages from OSL, IRSL, and ^{14}C ages (see section 3.1). We used @RISK to conduct Monte Carlo simulations that take into account a defined probability distribution (PDF) for each source of identified uncertainty, including the age, displacement, and fault orientation (e.g., Zechar and Frankel, 2009). The probability distribution was chosen according to the characteristics of the value, for instance displacement measurements were often represented by a PERT (continuous probability distribution defined by a minimum, maximum and preferred value) or triangular

distribution with the minimum and maximum displacement values representing the 95% confidence interval of the distribution and the peak at the preferred measurement. OSL/IRSL ages were represented by a normal distribution with the mean and standard deviation defined by the age and standard error returned from the lab. The @RISK calculation sheet, variable PDFs and final slip-rate values and distributions are presented in Appendix A.

3.1.8 Tree death ages

Strong shaking in moderate to large earthquakes can cause large-scale landscape change such as landslides and rockfalls (Keefer, 1984; Rosser and Carey, 2017; Quigley et al., 2016). These sedimentation events may or may not be coseismic, but if multiple events occur in different catchments within a short period of time, it may be inferred that there was some forcing event, such as a nearby earthquake. We identified sites in the study area where large sedimentation events caused the death of trees. We then used radiocarbon dates of outer rings of trees with OxCal analysis (OxCal 4.4; Bronk Ramsey, 2009; Hogg et al., 2020) to model the time of death of the trees. Some species of trees can live for decades in unfavourable conditions, so death ages are inferred to indicate the timing of the sedimentation event within ±20 years (Langridge et al., 2012). If trees in multiple locations are killed by geographically unrelated sedimentation events within a short period of time it suggests that these sedimentation events may have been the result of a local earthquake, thus helping to identify the date of the earthquake.

3.2 Results

In this section, each slip-rate site is presented individually, with site-level interpretations included. The system-scale interpretations are presented in the Discussion. Appendix A shows all the displacement and age PDF's imputed and outputted by @Risk in the slip-rate calculations. Appendix B includes ^{14}C dating results that were completed but did not contribute to site

interpretations. Appendix C has an additional slip-rate measurement from the Locke Stream site. Appendix D includes an additional dead tree site where we completed ^{14}C dating, but personal communications (included in the Appendix D) could not confirm if the trees were cut down before or after death and the ^{14}C dating did not determine the timing of tree death with enough precision to contribute to the paleoseismic history.

3.2.1 Site 1 Michael Creek fan

3.2.1.1 Geomorphic mapping

On the Hope Fault, we identified a suite of faulted and progressively displaced terraces at Michael Creek, a tributary that enters the Taramakau River from the north (Figure 3). This site is at a major bend in the Taramakau River valley (Figure 2 Site 1), east and upstream of this site, the Taramakau River valley trends ~070°, parallel to the Hope Fault, and west of this site the valley bends to ~090°. The Hope Fault is inferred to also bend and follow this trend, though no surface expression of the Hope Fault has been identified west of the Michael Creek fan (Vermeer et al., 2021). The Hope Fault is proposed to become an oblique extensional fault to the west, while most of the strike-slip motion is transferred south onto the Kelly Fault via NNE-striking linking faults (Vermeer et al., 2021).

On the west side of the active creek, one main fault trace has been identified, which splits into two traces on the west side of the fan (Figure 3A, location i). The fault here is south side up, with small pop-ups on the south side. On the west side of the fan where the fault has two traces (Figure 3A location i) the terrace risers are oblique to the fault and displacements are smaller on each fault splay. Secondary faults with NE strikes expected of Riedel shears extend from the main fault primarily to the north, but possibly also to the south, though these are less well defined (Figure

3A location ii). East of the active creek, the fault is only well defined on the highest surface (MC1e), where it has 4 splays in a horsetail formation. The fault likely also cuts the lower eastern terraces (MC8e, Figure 3 location iii), but the scarps are poorly defined.

A suite of 8 alluvial surfaces are mapped at the Michael Creek fan (Figure 3). Surface MC1 is the oldest and has remnants on both the east and west side of the creek. These remnants are interpreted to constitute part of the same, older and now mostly eroded, alluvial fan because the elevation and slope of both remnants can be matched by a single conical shape along smooth arcuate inferred pre-erosion contours, typical of alluvial fans (Figure 3A). The toe of this fan has been extensively cut back by the Taramakau River, so the eastern remnant only preserves the highest part of the fan. The western remnant preserves more of the distal fan, showing it graded to a local base level no more than 10 m above the current local base level (Figure 3A, location iv). Subsequently, Michael Creek has incised and deposited the younger terraces. Surfaces MC2, MC3, and MC4/6s all slope SW, following a roughly fan-like conical shape. Similar incisional, but conical, surfaces can be observed at other tributaries in the Taramakau River valley. The MC2 surface has a small mid-tread riser, but it is not well defined enough to confidently separate the MC2 into two separate surfaces. North of the fault, the MC3n and MC4n surfaces are distinct with a well-defined riser, but they cannot be traced to the fault scarp due to the infilling of the bog against the fault scarp. MC4n is sloped south, not southwest, thus it has been mapped as being included morphologically with MC8-4. South of the fault, MC3 and MC4 are less distinct and the riser separating them is much smaller than north of the fault.

Terraces MC4n and MC5n-MC8 are surfaces that slope south and are planar, suggesting a different formation process than the higher elevation, SW sloping, conical surfaces of MC4s, and MC1-3. The correlations of treads and risers across the fault are more confident in these terraces

than in the higher terraces. MC5 has a distinctive channel which is matched across the fault with high confidence. MC6 has correlative surfaces across the fault. MC7 is only present on the south (upthrown) side of the fault. MC8 is barely offset across the fault, there is a small (~10 cm) south-side-up scarp, but the tread is not displaced enough to make a confident measurement of offset because it is a similar magnitude as the roughness of the surface. The west edge of MC8 has a left step across the fault because the surface on the north side of the fault was not abandoned after the displacement event(s) which uplifted MC7, so MC7 has no direct correlative surface across the fault. MC8 is the youngest inactive terrace on the west side of the creek, and the eastern riser defines the edge of the active stream channel. MC8 has multiple shallowly incised channels on the south side of the fault, and small risers on the north side of the fault. These features are discontinuous, small in height, and disrupted by small displacements on secondary Riedel faults. The channels on the south side of the fault which are not matched by channels on the north side indicate that the stream continued to occupy this surface through one or more surface ruptures and displacements, promoting some infilling north of the fault (resulting in surface with few coherent fluvial features) and incision south of the fault (forming the multiple, anastomosing channels). The south end of MC8 is cut off by a much lower terrace of the Taramakau River, but just west there is a higher Taramakau terrace remnant, MC8b. Although these terraces are not continuous because of erosion, accounting for the downstream slope of MC8 formed by Michael Creek, versus that of MC8b formed by the Taramakau River, MC8 and MC8b likely were continuous and formed around the same time, at the same river level.

3.2.1.2 Trench on Michael Creek Fan

We hand-dug a trench across the Hope Fault at site J134 (Figure 3B, Figure 4). On the upthrown (south) side, the lowest unit is matrix rich, poorly sorted, sandy gravel with clasts up to

boulder size, within a reddish-brown, lightly indurated matrix (RS) (Figure 4). RS has a sharp upper contact and is directly overlain by TC, which is a tan coloured, poorly sorted sandy gravel that is a slightly more orange in colour than RC and has a loose in-situ texture. TC is interpreted as re-worked RS, of likely colluvial origin. On the downthrown (north) side of the trench, the lowest exposed unit is GS, a light grey silty clay matrix-supported gravel with very angular clasts up to pebble size. GS is tightly packed with little pore space, but it is soft and malleable indicating high water content. GS has a sharp, nearly horizontal upper contact with unit P, a mass of organic material that may be a decaying root ball or decaying fibrous plant material that extends into the peat bog. P has an irregular, subvertical contact with TC. Unit FF is a ~40 cm wide subvertical zone of loose granular particles of matrix and clasts from both RS and GS in a limonite rich matrix. The quantities of RS and GS particles in FF are laterally gradational so each particle type dominates on the side nearest the source unit. we interpret FF as the fault zone. The south edge of the fault zone strikes 082° and dips 62° S. FF is overlain by TC with an irregular but nearly horizontal contact that has limonite staining where it is sharp. The triple contact between RS, TC and FF in the central/south part of the trench is a diffuse irregular contact (Figure 4 pic). Part of unit TC is beneath RS, which we interpret as TC infilling a pocket/irregularity in the surface topography formed by the most recent surface rupture. Because TC appears unfaulted and is not mixed into FF, we interpret it as a post-faulting unit.

In the trench, we sampled unit GS for ^{14}C and OSL, RS for OSL and TC for ^{14}C. The TC ^{14}C material (sample J134D) comprised small twigs or roots, which yielded modern ages (Figure 4). These as roots are inferred to have grown into (and subsequently been dismembered within) the sediment after deposition. The GS ^{14}C material (sample J134A) of small charcoal fragments yields an ^{14}C age of 242 ± 19 radiocarbon years (Figure 4 inset ^{14}C calibrated age curve). Its

calibrated age range is 1653-1677 (22.5%) or 1735-1800 (73.0%) Cal AD. The charcoal is not interpreted as being burned in situ and therefore represents a depositional age. The GS OSL age (J134B) is 16.1 ±1.0 ka and the RG OSL age (J134C) is 9 ±2 ka (Figure 4 and Table 1).

3.2.1.3 Stratigraphy and OSL/IRSL samples

To understand the development of the terraces, we dug pits to observe the physical characteristics of the sediments and collect samples for dating. Stratigraphic logs of the sampling pits and photos are in Figure 5, and the locations of luminescence samples are in Figure 3. We observed some similarities in physical characteristics of the sediments across the pits and have identified clusters of luminescence ages that we used to estimate absolute ages of geomorphic and sedimentological features and events.

J106 and J22, on MC1 and MC4, had similar stratigraphy of an organic rich soil, overlying a lilac-grey coloured clay rich gravel horizon, over pebble to cobble gravel, with red-orange clay rich matrix and cobbles with up to 1 cm weathering rinds. The OSL samples taken from within this deeply weathered cobble gravel at J22 and J106 are 24.9 ±1.5 ka and 28 ±2 ka respectively. The pIRIR/OSL ratio and IR50/OSL ratio indicate that J106 is well bleached and J22 is likely well bleached (see OSL dating background section). We observed similar sediment in the base of the pit at J36 on MC6, but this sample did not yield a luminescence signal.

Samples J35, J36 and J134C are all from slightly weathered sediments (Figure 5). J35 is from a sandy lens near the base of a lightly weathered grey loose sandy cobble gravel underlying surface MC8 exposed in the cutbank on the west edge of Michael Creek (Figure 3). The sampled unit underlies a lightly weathered dark grey sandy cobble gravel with angular clasts and overlies a brown medium sand. Sample J36 is from a 20 cm thick bluish grey silt with no discernible sedimentary structure that overlies a deeply weathered orange cobble gravel with clay rich matrix

that is similar to the sediment sampled at J106 and J22 (Figure 5). J134C is from the downthrown side of the trench, in the light grey pebbly silt which underlies the bog. The OSL ages of these three samples are J35 (15.3 ±1.1 ka), J36 (11.5 ±1.0 ka) and J134B (16.1 ±1.0 ka) (Table 3.1). For J35 and J36, the IR50/OSL ratio is ~1, but the pIRIR/OSL ratio is greater than 1, meaning these samples likely have bleached quartz, but incomplete pIRIR bleaching. Sample J134B has IR50 and pIRIR ages much older than the OSL age (IR50/OSL > 1 and pIRIR/OSL > 1), leaving uncertainty about whether this sample was fully bleached, so the OSL age may be older than the last deposition. We interpret these sediments as postglacial material, which may or may not have been reworked during incision of the terraces but was last bleached so that it retains the early post-glacial depositional age.

At J134C and J133 (Figure 3 and Figure 4 and Figure 5) the sediment is moderately weathered gravel (clast weathering rinds <10 mm and mostly <5 mm) with a moderate amount of clay in the matrix. Sample J134C was taken from unit RS on the upthrown south side of the fault in the trench and yielded an OSL age of 9 ±2 ka (Figure 4 and Table 1). J133 was taken from the root ball of a fallen tree on MC6, which would have placed the sample at 1-1.5 m depth until the tree fell. The tree had fallen recently, shown by the mix of dead and live leaves both on the tree and on the surrounding damaged vegetation. J133 yields an OSL age of 7.8 ± 0.5 ka (Table 1). Both J134C and J133 have IR50/OSL >1 and pIRIR/OSL >1, so we cannot be sure the OSL was completely bleached during deposition and may have inherited age.

Sample J29 is from a light grey sandy silt unit overlying a medium brown cobble gravel, representing deposition of/on MC8b. The OSL age of J29 is 2.8 ±0.3 ka (Figure 5 and Table 1).

The relative ages of the geomorphic surfaces and the absolute ages of the underlying sediments do not directly correlate in most instances at Michael Creek fan (Figure 6). The oldest

sediments (J106 and J22) were collected from the oldest surfaces, but they are both pre-last glacial advance, which is constrained by the age of moraines on the coastal plain at Lake Brunner (Figure 2 Moana formation, Kumara-3 glacial advance, 17.3 ±0.5 ka, Barrows et al., 2013). It is unlikely that geomorphic surfaces near the valley floor would have survived beneath the ice, so these sediment ages are unrelated to the formation ages of the MC1 and MC4 surfaces from which they were collected. We interpret samples J106 and J22 to be from sediment which was not scoured out of the valley during the last glacial advance and was deposited sometime prior to that. Taken at face value, the sediments in sample J106 are 28 ±2 ka, which would correlate with deposition during the pre-Kumara-1 interglacial time. The OSL age for J22 is 24.9 ±1.5 ka, potentially between the Kumara-2_2 (~24.5-21.5 ka, Suggate and Almond, 2005) and Kumara-2_1 (~34 – 28 ka)). Although the Taramakau glacier recession between Kumara-2_2 and Kumara-2_1 is only 4kyr long, the recession of the ice from the Moana moraines on the coastal plain (17.3 ±0.5 ka, Barrows et al., 2013) to Arthurs Pass (15.2 ±0.8 ka, Eaves et al., 2017) took only 1-2 kyr, leaving the possibility that the Michael Creek site could have been deglaciated and re-glaciated during the time between the Kumara-2_2 and Kumara-2_1.

The 11-16 ka sediments (Samples J35, J36 and J134C) are interpreted as early post-glacial sediment that was deposited as the last ice retreated and formed the MC1 fan (Figure 6). These sediments were deposited on top of the ~24-28 ka pre-last glacial sediment, which was then exposed on the upthrown side of the fault (J106, Figure 3 and Figure 5) and by incision of the MC2-8 surfaces (Figure 6). Early post-glacial sediments are only observed on the north (downthrown) side of the fault, while pits on the south (upthrown) side of the fault expose the older, more heavily weathered sediments. This may result from removal of the early post-glacial

sediments from the upthrown side of the fault and preservation of small amounts on the downthrown, upstream side of the fault (Figure 3 and Figure 5).

The intermediate age samples, J134C 9 ± 2 ka and J133 7.8 ± 0.5 ka are interpreted to represent the ages of MC4 and MC6, respectively (Figure 6). These sediments are both younger than the early post-glacial sediment, however they are more weathered (weathering rinds on the clasts, red-orange clay in the matrix, Figure 5), which we attribute to the incorporation of the highly weathered pre-last-glacial sediments into the early Holocene terrace sediments as they were incised.

As presented earlier, geomorphically the MC8b and MC8 terrace surfaces are likely the same age (Figure 3). Although the sample at J35 underlying MC8 was 15.3 ± 1.1 ka, we consider it unlikely that the surface with the youngest relative age could be realistically represented by this sample for two reasons. First, this terrace is geomorphically younger than the surfaces where early Holocene OSL ages were sampled (J134C and J133 on MC4 and MC6). Second, MC8 and MC8b are likely of similar age and deposited during the same local base level, and MC8b is dated by OSL sample J29, which is only 2.8 ± 0.3 ka. For these two reasons, we consider the OSL age of J35 to be inherited from early-post glacial deposition, and the formation age of the MC8 surface to be more accurately represented by the late Holocene age at J29.

It is unlikely that a terrace surface like MC8, this low in the valley and geomorphically younger than surfaces dated at a maximum of 9 ± 2 ka, could have depositional ages separated by >10 kyr. We propose that this discrepancy between J29 and J35 could be because the quartz grains did not have enough sunlight time during mid-late Holocene re-working of early postglacial sediment within a tributary stream to re-bleach the quartz. However, in the Taramakau River, the travel distance of any particular grain is likely much longer and less dependent on short duration,

high energy transport events, giving it more potential sunlight time to be re-bleached and attain an accurate age for the deposition and terrace formation. Thus, 15.3 ±1.1 ka is a maximum, but inaccurate age for formation of the MC8 terrace tread, which is closer to the minimum age of 2.8 ±0.3ka. It is possible that J133 and J134B may also not have been fully bleached upon re-working, making the age of 9 ± 2 ka a maximum age for the MC5 terrace tread.

3.2.1.4 Slip-rate

On the Michael Creek fan (Figure 3), there are three terrace risers (R4/5, R5/6, R6/7) and one terrace tread channel (MC5t) that can be correlated across the fault. R4/5 has a minimum right-lateral displacement of 9.4 m and a maximum of 12.1 m, the preferred displacement is equal to the maximum displacement. The south-side-up vertical displacement is 2.0-2.3, with the preferred vertical displacement being 2.3 m. R5/6 has minimum right-lateral displacement of 5.2 m, maximum of 11.4 m and preferred displacement 8.5 m. The vertical displacement is south side up, minimum 1.3 m, which is also preferred, and maximum of 2.0 m. we have matched MC5t, the channel on terrace MC5, across the fault based on the thalweg of the channel. The minimum lateral displacement is 3.1 m, the preferred is 6.7 m and the maximum is 10.5 m. The vertical displacement is 2.0 m south side up. Riser R6/8 north of the fault correlated with R6/7 south of the fault. The minimum displacement is 0.6 m, the preferred is 0.8 m and the maximum is 2.4 m. The south-side-up vertical displacement is minimum 0 m, preferred 0.3 m and maximum 0.8 m.

The OSL sample J134C constrains the formation age of MC4 by representing when the surface was active, and the sediment was deposited or reworked and re-bleached. Sample J133 constrains the formation age of surface MC6 by representing when the surface was active, and the sediment was re-worked and re-bleached. As discussed earlier, these samples are of bleaching quality 3, so they may have some or much inherited age. The minimum age for the suite of terraces

is constrained by J29 which dates MC8. These three ages constrain the age of displaced features R4/5, MC5t, and R5/6 with a probability distribution defined by the probability distributions of the OSL samples in each Monte Carlo simulation. J134C represents the maximum age for any of these features, as it is a maximum age for the sediment on the highest relevant surface. Thus, the age PDF of J134C is used to define the maximum age for the features. J133 is used as the likely mean age for the features, and the mean of the feature age PDF is chosen from this sample's PDF. J29 is used to select the minimum age for the samples in each simulation. Because the three displacement measurements are slightly different but evaluated with the same age constraint, they produce a range of slip-rates that decrease with decreasing relative age. R4/5 has the fastest slip-rate at 1.7 (+1.1/-0.4) mm/yr, MC5t is 0.9 (+0.9/-0.4) mm/yr and R6/5 is 1.1 (+0.9/-0.5) mm/yr (Table 3.3). This is not indicative of a slip-rate that changes through time, rather an artifact of using the same age range (7.3 ± 1.4 ka) for three different features that likely have different ages that cannot be resolved with the current age control. We consider the R4/5 slip-rate of 1.7 (+1.1/-0.4) mm/yr to be the most robust, because if the OSL ages do have some inherited age, the slip-rate derived from the oldest displacement would be the least affected and closest to the true slip-rate.

3.2.1.5 Paleoseismic age control

In the Michael Creek fan trench at J134, we collected two radiocarbon samples (Figure 4). Radiocarbon sample J134D from TC, the unfaulted colluvial deposit, was organic poor, and the sampled material of twigs (possible roots) returned a modern age (post-1950). This may represent the age of the deposit or that the sampled material is fragments of infiltrated roots that have no relation to the depositional age of the sediment. The material sampled for J134A from GS, the grey silt north of the fault was small delicate woody (possibly bark) fragments, considered to be detrital

and emplaced during deposition of the sediment because the sediment was coherent in-situ material with no observed root infiltration or bioturbation. Radiocarbon sample J134A yielded a CRA of 242 ±19 yr BP, giving a calendar age at 2σ confidence of 1653-1677 CE (22.5%) or 1735-1800 CE (73%). This is from the same deposit as J134B, the OSL sample which returned an age of 16.1 ±1 ka. Considering the order of magnitude difference between the 14C and OSL ages, and the grade 3 OSL bleaching certainty, we interpret this deposit as re-worked older sediment that was not OSL reset prior to re-deposition in unit GS. Thus, we consider the radiocarbon age of sample J134A to be representative of the depositional age of unit GS.

Because GS is faulted, the radiocarbon age provides a maximum age for the last surface rupture at this site of 1653 CE, but it could potentially be as young as 1848 CE, when a historic surface rupturing earthquake would have been unlikely to go unnoticed (Langridge et al., 2020). The modern radiocarbon age of J134D in TC, the colluvial unit, does not constrain the age of the last surface rupture because 1) the dated material may not represent the depositional age of the sediment and 2) there has been no historically recorded (i.e. ca. 1848 to present) surface rupture on this fault.

3.2.2 Site 2: Yeo Creek fan

3.2.2.1 Mapping

In the upper Taramakau River valley, Yeo Creek and Joseph Creek flow from the north and form a complex suite of alluvial fans that are trimmed by the Taramakau River and inset alluvial terrace surfaces (Figure 2 and Figure 7). The Hope Fault cuts these landforms with a single main trace with some discontinuous Riedel shears extending off the north side of the main trace. The strike of the main trace turns from 85° between Yeo and Joseph creeks to 70° west of Joseph

Creek; the bend is within the active channel and young alluvial features of Joseph Creek (Figure 7). Where the fault trace crosses topography, the deformation zone is too wide to determine the fault dip, so we assume the fault is vertical. The fault forms an uphill (north) facing scarp that is ~1m high on the lowest terrace surface (YC2b)), the scarp is higher on the older fan between Yeo and Joseph creeks where it juxtaposes younger incised surfaces with high remnant fan surfaces. The remnants of the high fans south of the fault are small and discontinuous. The fan surfaces west of Joseph Creek have been deeply incised, revealing they are composed of coarse (up to 30 cm diameter), angular, poorly sorted, slightly stratified gravel.

The geomorphic development of this site from oldest to youngest is determined using relations between preserved surfaces, erosional features, and local base level set by the Taramakau River. The highest and therefore likely oldest surfaces are YC1 (Yeo Creek surface 1), JC1 (Joseph Creek surface 1), and UC1 (unnamed creek surface 1), these surfaces have trimmed toes, and projection of the surfaces indicate they graded to a local base level 0-40 m higher than the current base level (Figure 7B). Lateral migration of the Taramakau River may impact on the apparent base level the fans have graded to; if the river was on the far side of the valley, it could have been at the same elevation it is now, and the fans would have formed the preserved high surfaces. However, similarly high fan surfaces could have formed if the main river was flowing on the north side of the valley and the valley bottom was up to 40 m higher than it is now. We favour the former interpretation but determining which is not critical to understanding the rest of the geomorphic development.

After deposition of the highest, oldest fans, the Taramakau River meandered north and cut the toe of the fans between Yeo and Joseph creeks (Figure 7 marker i, YC1 and JC1). At this time it may have also trimmed the toes of the fans west of Joseph Creek (UC1), but lack of younger

surfaces does not constrain the timing for them. After the toe of JC1 and YC1 was trimmed, subsequent sedimentation emanating from Joseph Creek was deposited over the older fan surface, and JC2 was deposited on the trimmed toe of the old fan. This created a surface with the upper slope similar to the old fan, but that formed a steeper small fan cascading over and curving around the toe of JC1 (Figure 7 marker ii). The west side of JC2 is incised ~2m by surface JC3 (forming R2/3), and both are cut back by the main river (Figure 7, marker iii, iv). After the JC2 and JC3 were cut back, Yeo Creek incised the old fan surface (YC1) and formed a younger terrace/fan surface (YC2) which also wraps around the old toe (Figure 7, marker i). There is not a sharp delineation between YC2 and YC2b, but YC2b slopes west and wraps around the cut toe of JC2 (Figure 7 marker iii). Because the Yeo-sourced surface wraps around the cut toe of JC2, it indicates that the final formation of YC2 surface is younger than the deposition and toe trimming of JC2, although the incision of YC1 may have been occurring during formation of JC2 and JC3. After formation and during toe trimming of JC2 and JC3 (Figure 7 marker iii, iv), deeper incision of JC began which eventually formed JC4 and JC5 and around this time the fault started to displace the east side of the channel. As displacement accumulated, it is possible that the east side of the channel on the south side of the fault (Figure 7 marker vi) was eroded eastward, but there are insufficient landforms to determine the extent to which this happened.

3.2.2.2. Displacement measurements

The east edge of Joseph Creek on the south side of the fault can be matched to the riser between JC3 and JC4 (R3/4) (Figure 8A and B). This implies that the remnant surface south of the fault corresponds with JC3 north of the fault. The remnant surface south of the fault is too small to confidently match the morphology to any surface north of the fault. The maximum elevation of the knob is higher than expected for a downslope projection of JC3 or JC2, indicating there has

been some south side up displacement on the fault (Figure 8D). The arcuate shape of the trimmed toe (v) matches up with the toe of JC2 (iii) if the fault is back-slipped so the west edge of the southern remnant (vi) is aligned with the west edge of JC3 (R3/4), implying that the toe of JC3 (iv) is actually formed by the fault cutting the fan surface. If the fault is back-slipped so the west edge of the southern remnant aligns with the west edge of JC2 (R2/3), then the arcuate cut of the toes does not line up. It is possible that that toe trimming happened after the fault had begun displacing the fan surfaces before the toe was cut, in which case the southern remnant could have originally been part of JC2.

Because of the uncertainty whether the southern remnant was ever part of JC2, we have measured the displacement between the western edge of the southern remnant (vi) and the western edge of JC3 (R3/4), resulting in 65 (+3/-5) m displacement (Figure 8C). This is a minimum displacement, because the western edge of the southern remnant (iv) could be eroded eastward by the active stream.

3.2.2.3 Age constraints

At the Yeo Creek site, sample J82 was taken from sediments underlying the YC2b surface, accessed from the southern riser down to the T1 surface (Figure 5 and Figure 7 A and C). The OSL age of J82 is 14.2 ± 1.0 ka (Table 3.1). The YC2b surface is 2 ± 0.2 m above the local Taramakau River main channel, while the MC8b surface at Michael Creek overlying sample J29 is 4 ± 0.3 m above the main Taramakau River channel, and J29 is only 2.8 ± 0.3 ka (Figure 7 Table 1). Although possible, it is unlikely that the Yeo Creek T1 surface is truly 10 kyr older than the geomorphically slightly higher terrace at Michael Creek. If we reject that the luminescence age of J82 could truly represent the formation age for the overlying surface (YC2b), then the luminescence age must be fully or partially inherited through re-working of older sediments without bleaching and re-setting

the age (Figure 7C). Because the sediment source is likely the sediments underlying the upstream surfaces (YC2, YC1, JC2), the sediment depositional age must be older than those surfaces. If there has not been any partial resetting of the luminescence age, then the J82 age of 14.2 ± 1.0 ka is a maximum age for YC2, YC1 and JC2, and all incised surfaces.

3.2.2.4 Derived slip-rate

The displacement was calculated using a triangular distribution where the 5% and 95% confidence intervals are 60 m and 68 m respectively and the peak is at 65 m. For the age of this displacement, we use a PERT distribution where the minimum is 9 ± 2 ka based on the oldest incised post-glacial sediment at Michael Creek. We chose this minimum age because before this time the valley went from early postglacial sedimentation to stabilization and fluvial incision on the tributaries. For the maximum age, we use the sample J82 (14.2 ± 1 ka) because it represents the age of the early postglacial Yeo/Joseph Creek sediments and thus any incisional surfaces must be younger. We set the peak for the distribution using J36 (11.5 ± 1 ka) because it is the youngest un-reset post-glacial sediment in the valley, so around this time was likely when incision began. These constraints yield a slip-rate of 5.6 (+2.1/-0.7) mm/yr (Table 3).

3.2.3 Site 3: Locke Stream fan

3.2.3.1 Mapping

On the east side of Locke Stream are two large fans (LS1 and LS2) and three alluvial terraces (LS3, LS4, LS5) (Figure 9). The highest fan (LS1) is composed of coarse angular poorly sorted gravel with a silt rich bluish grey matrix. The fan surface is sloped ~13° N with arcuate contours, and it hosts small stream channel features. The fan surface is cut and displaced by the Kelly Fault, resulting in an uphill (south) facing scarp. The fault splays at the western side of the

fan, producing a series of fault scarps which fan out to the NW that terminate at the edge of the fan (Figure 9 location i). The east edge of the upper fan is delineated by a deeply incised, active stream channel which has a right bend where it crosses the fault (Figure 9 location ii). East of this stream, some remnant surfaces may correlate to the large fan. The north edge of the fan is cut by the Taramakau River, resulting in a 40 m high riser. The west and northwest side of the fan is defined by a riser which drops down to a lower fan (LS2) that emanates from Locke Stream and has a much lower slope than the high fan. LS2 extends nearly across the main river valley. There is no surface morphology that is indicative of a fault scarp on this surface. This fan is incised by the active Locke Stream, which has formed a series of terrace surfaces (LS3-5) at the distal end of the fan where the stream meets the Taramakau River.

Fan LS1 emanates from a small catchment east of the Locke Stream catchment (Figure 9 location iii). The top edges of this catchment are sharp and the valley morphology upstream of the fan is rough. The steep gradient of the fan surface and the nature of the sediment (coarse, angular, high sandy silt matrix content) suggest that this fan may be the result of a large slope failure and subsequent deposition of the material within the Taramakau River valley. If it is, then the fan surface was likely not active for very long, as the flow from Locke Stream probably quickly dominated and cut the west side of the fan. The local base level when this fan formed was between 10-40 m above the current river level, based on a linear projection of the fan surface across the Taramakau valley.

After formation of LS1, Locke Stream cut back the western edge of the high fan and deposited LS2. This fan has a slightly lower gradient than the high fan, and a smooth almost featureless surface. The contour arcs of LS2 east of Locke Stream do not match with LS3 west of Locke Stream, which is slightly lower, indicating that LS3 is younger than LS2. The relative age

of LS3 is likely related to the incisional terraces east of the stream (LS4-5). These younger fan and terrace surfaces are located north of the projection of the LS1 fault trace, and none show any morphologic evidence of being faulted.

3.2.3.2 Displacement measurements

Displacements on the Kelly Fault at Locke Stream were estimated by correlating small channel and ridge features on the high fan surface (LS1) (Figure 9 and Figure 10). The channels and ridges formed while the fan surface was active and they were preserved when the fan surface was abandoned, then the measured offsets occurred after abandonment. We identified two possible reconstructions of the LS1 surface. The preferred reconstruction (KF1a) results in 91 ± 13 m dextral displacement and 6 ± 0.5 m vertical, south side up (Figure 10). The second possible reconstruction (KF1b) results in 51 ± 11 m of dextral displacement and 8.5 ± 0.5 m vertical, south side up displacement (Appendix C).

Displacements were not estimated using the incised stream channel at the east side of the fan (Figure 9 location ii) because it is still active, the deep incision indicates it is highly erosive, the original geometry is unknown, and the channel has a different trend on either side of the fault. The western edge of the fan is not measured because if the entire right step was formed by displacement on the fault, at least some of that displacement would have occurred after the formation of LS2, but no evidence of fault related deformation extended from any trace of the fault on LS1. This doesn’t preclude any faulting of LS2, but there hasn't been enough displacement to form identifiable scarps in the time since the fan surface has been inactive. The main trace of the fault here has nearly pure strike-slip displacement, so it may not form a vertical scarp, however the splays (Figure 9 location i) have oblique displacement on LS1, so they should have also formed scarps on LS2. Instead, we interpret the right step in the western edge of LS1 (Figure 9 location i)

to primarily reflect slope collapse in the area weakened by the fanning fault splays. This slope collapse is proposed to have occurred prior to the last activity of LS2 because the amount of colluvial material presently on LS2 is significantly less than the volume of material missing from the slope collapse scar, so it was likely washed out while the surface was still active. This sequence of events can explain how the magnitude of the right step is similar to displacement LS1, without having all the observed fault displacement occur in the time between the abandonment of LS1 and abandonment of LS2. If some of the apparent displacement of the western edge is due to slope collapse, the accumulated slip on LS2 can be less than on LS1, explaining the absence of scarps on LS2 without necessarily requiring a temporally variable slip-rate.

3.2.3.3 Age constraints

Because the sediments in the LS1 fan (Figure 9) are very poorly sorted with an abundance of large angular cobbles, we were unable to retrieve an OSL sample from this fan. Because we lack local age control for this fan, we infer its maximum age based on timing of glacial retreat determined in other nearby sites that opened the valley to sedimentation, and the timing of base level drop that initiated formation of the middle fan. Because LS1 is the oldest post-glacial deposit at the Locke Stream site, and slope instability is common during and after glacial retreat (e.g., Holm et al., 2004; Allen et al., 2011; Kos et al., 2016), we assume that LS1 is an early post-glacial feature. As discussed in section 2, the age of the moraines on the coastal plain (Figure 2 17.3 ± 0.5 ka, Barrows et al., 2013), indicates the valley was still occupied by ice at that time so the fan must be younger than that. we also have OSL ages of alluvial sediments downstream in the Taramakau valley at Michael Creek that provide intermediate ages for the ice retreat, when ice was gone from Michael Creek area but may have been still occupying the valley further upstream (oldest is J134B 16.1 ± 1 ka, but this sediment might not be alluvial; the oldest clearly alluvial sediment sampled

is J35 15.3 ± 1.1 ka). Finally, ages of end moraines in Arthurs Pass (15.2 ± 0.8 ka, Eaves et al., 2017) indicate the time when ice was limited to the cirques and high elevations indicating the lower valleys (including the Locke Stream area) should have been completely free of ice. Thus, the maximum age limit for the fans at Locke Stream is 17.3 ±0.5 ka, and the preferred age is 15.2 ± 0.8 ka.

The minimum age for the Locke Stream fans is more difficult to constrain. Downstream, the Yeo/Joseph creek and Michael Creek sites indicate that there has been 0 to 20 m of local base level drop since those fans formed, while LS2 at Locke Stream indicates 10 to 20 m of local base level drop has occurred since it was formed. This may indicate that LS2 is older than the fans downstream, or it may indicate a different local geomorphic environment where the confined Taramakau River has down cut more than the wide braided river downstream. At Michael Creek, incision of the early post-glacial fan was well underway at 9 ±2 ka, so we use this for the minimum age of LS1.

3.2.3.4 Derived slip-rates

To derive slip-rates, we use the lateral and vertical displacements with a steeply north dipping fault. We set the maximum age for the fan as 17.3 ± 0.5 ka because at that time ice occupied the valley. The minimum age is 9 ± 2 ka, because by this time incision was underway at Michael Creek so the LS1 fan was likely also incised and abandoned. This yields a net slip-rate of 6.2 (+2.4/-1.0) mm/yr for the preferred displacement of KF1 (Table 3.3).

3.2.4 Site 4: KF2

3.2.4.1 Mapping

East of the Otehake River, the Kelly Fault PSZ cuts and displaces a hill spur (Figure 11A location i). The fault trace cannot be precisely identified west of the spur where it crosses alluvial fans (Figure 11A location ii). Some secondary faults of the Kelly Fault DDZ have been mapped on the hillside south of this fault trace (Figure 11A location iii), but these faults do not cut and displace features that can be correlated across the fault trace.

3.2.4.2 Displacement measurement

To measure fault displacement here, we match the displaced ridge across one prominent trace of the Kelly Fault (Figure 11B and C). The fault strike here is 070 ±3°. The strike-slip displacement is 16 ± 6 m. The vertical fault displacement is measured by matching the fault parallel topographic profiles and finding the difference between the actual observed vertical offset and the expected vertical offset based on the slope of the ridge (Figure 11D). The vertical fault displacement is 16.5 ± 1.5m, north side up.

3.2.4.3 Age control

No direct age control is available at this site. The maximum age of the ridge is no older than when ice occupied the valley. There is no constraint on the minimum age of the landforms. The age distribution used to calculate the slip-rate has an absolute maximum of 17.3 ± 0.5 ka, peak probability at ~15 ka, when the valley was definitely ice-free (based on age of end-moraines in Arthurs Pass, Eaves et al., 2017), and extends to present with low probability, so the minimum age is 0 ka. We select the peak probability as 15 ka under the assumption that the features are likely formed during the early postglacial landscape settling.

3.2.4.3 Slip-rate

Using the displacement and age as discussed, a net slip-rate of 1.8 (+2.3/-0.3) mm/yr with a SS:DS ratio of 1:1 is estimated (Table 3.3). This slip-rate is produced by giving preference to an early postglacial age to the displaced ridge. However, ridges are an erosional feature and may be continually refreshed. Where there is a fault scarp, the fault displacement is outpacing the erosional refreshing of the landform.

3.2.5 Site 5: KF3

3.2.5.1 Mapping

West of Lake Kaurapataka, the Kelly Fault PSZ cuts a hill spur forming an uphill facing scarp (Figure 11E). The slope has a channel remnant which trends perpendicular to the fault scarp and can be identified on both sides of the fault (Figure 11F). This channel has similar cross-sectional morphology, longitudinal slope, and planform trend on both sides of the fault (Figure 11F and H). On the south side of the fault, the upstream side, the channel is obscured by deposition against the fault scarp (Figure 11F). North of the fault, the channel does not reach to the top of the scarp, likely due to scarp degradation.

3.2.5.2 Displacement measurement

Figure 11E shows the landscape around the displacement measurement laterally restored. Not only does the identified channel correlate across the fault, subtler features just west of the channel also correlate with the same amount of fault displacement. The lateral displacement of the channel is 80 m (+18 m/-17 m), with most of the uncertainty being from the projection of the channel to the fault scarp. Since both channel remnants have the same trend and slope and are

almost straight, we prefer the straight projection of the southern channel remnant to the fault. We measured the lateral displacement parallel to the apparent strike of the fault.

The vertical fault displacement is estimated using a combination of fault parallel and fault perpendicular topographic profiles (Figure 11G and H). The landscape slope is used to calculate the slope of the landscape that is used to calculate the expected vertical offset of the fault parallel profiles, if there had been no faulting (Figure 11G). Next, we shift the downslope fault parallel profile to see how it matches with the upslope profile and to determine where correlative features are located (Figure 11H). Once the profiles are matched, we can measure the actual vertical offset of the two profiles by finding the difference in elevation between the same point on the original downslope profile and the shifted profile. We then subtract the expected vertical offset based on the landscape slope and horizontal distance between the profiles to find the amount of vertical offset that is the result of fault displacement, which is 17.5 ± 2.5 m (Figure 11H).

3.2.5.3 Age control

No direct age control exists for this site. The maximum age of the channel is no older than when ice occupied the valley. we have no constraint on the minimum age of the landforms. The age distribution used to calculate the slip-rate has an absolute maximum of 17.3 ± 0.5 ka, peak probability at ~15 ka, when the valley was definitely deglaciated, and extends to present with low probability, so the minimum age is 0 ka. We chose the peak probability as 15 ka under the assumption that the features are likely formed during the early postglacial landscape settling.

3.2.5.4 slip-rate

From the displacement and age assumptions the net slip-rate for the Kelly Fault at KF3 is 6.2 (+7.8/-1.2) mm/yr (Table 3.3).

3.2.6 Site 6: Sackung Hill

Vermeer et al. (2021) presented an overview of the structure and geometry of Sackung Hill and identified two sets of tectonic faults among the gravitational fault network (Figure 12). These faults are postulated to transfer tectonic slip from the Hope Fault near Michael Creek to the Kelly Fault south of Sackung Hill. Alternatively, the Sackung Hill tectonic faults may be part of a distributed deformation zone between the Hope and Kelly Faults. The significance of each interpretation is presented in the Discussion below. One site on each tectonic fault set is selected to determine a minimum tectonic slip-rate based on displacement of glacial striations (Figure 12).

3.2.6.1 Age control

The glacial striations on Sackung Hill formed when there was ice filling the valley. Moraines at Lake Brunner indicate the whole valley was under ice at 17.3 ± 0.5 ka when they were formed. At 15.2 ±0.8 ka the end moraines at Arthurs Pass formed, indicating that the ice had retreated from the valleys by this time. Thus, the striations were formed between ~17 ka and ~15 ka. This glacial retreat age is supported by the OSL ages from fluvial or alluvial deposits upstream, which indicate that by 14-15 ka the upper Taramakau valley was free of ice. Based on these constraints on the timing of glacial retreat, we set the age of the glacial striations as 16 ± 1 ka with a normal distribution.

3.2.6.2 Site 6a

This glacial striation is low on the NW corner of Sackung Hill (Figure 12). It is cut by a NNE striking, steeply west dipping fault interpreted by Vermeer et al. (2021) as a tectonic fault. We use the crest of one striation as a linear piercing point to measure lateral and vertical displacement (Figure 12a). We measure 22 (+1/-5) m of lateral displacement. Fault-parallel profiles are used to match the striations, and fault-perpendicular profiles to determine the expected

vertical offset of the fault parallel profiles before faulting (Figure 12 profiles), yielding 1.2 ± 0.2 m west side up vertical fault displacement (Figure 12D). The net slip-rate is 1.3 (+0.1/-0.4) mm/yr, with primarily dextral displacement (Table 3).

3.2.6.3 Site 6b

This displacement site is located on an E-W striking sub-vertical fault between two NNE-striking faults. The identified striation and trough match across the fault, and the slope change shown by the yellow line in Figure 12B is used as the piercing line. The feature is at about the same elevation on both sides of the fault, the height of the scarp is produced by laterally displaced topography. We measured 22 (+6/-3) m of dextral displacement and <0.5 m of vertical displacement. This yields a net slip-rate of 1.3 (+0.1/-0.4) mm/yr (Table 3.3).

3.2.6.4 Discussion of Sackung Hill slip-rates

The extensive fault network on Sackung Hill has been interpreted as a combination of gravitational and tectonic faults (Vermeer et al., 2021). These measured displacements show offsets that exceed plausible single event displacements for tectonic faults, indicating these faults have been active in multiple earthquakes. These sites and others on Sackung Hill have depocenters against the faults, giving them potential for yielding earthquake timing via paleoseismic investigations.

There are many displacements of the glacial striations that could be measured, however untangling how the displacements relate to tectonic versus gravitational stresses is difficult. Both sites have primarily dextral displacements, and gravitational displacements are usually normal. Also, these faults do not strike parallel to the slope like gravitational faults. There are multiple NNE-striking faults that are similarly continuous to the fault we measured the displacement on,

but there are not similar displaced features that we can confidently match across the faults. The total tectonic slip transfer through these faults is greater than the slip-rate presented here, thus this is a minimum slip-rate for the Hope-Kelly transfer faults.

3.2.7 Site 7: J6

One Shot Hill (Figure 2 Site 7), west of Sackung Hill, was also identified as having extensive sackung faulting, but with less lidar coverage and heavy vegetation (Vermeer et al., 2021). At the northern base of this hill the low elevation inactive terraces are deposited against the base of the hill (Figure 13). The NW corner of the hill appears to be faulted, with an uphill facing scarp on the north side that rises from the base of the hill and the curves around the west side of the hill before decreasing in apparent displacement to the point of being unidentifiable with topographic data. Extending east from the hillside scarp, the alluvial sediments abutting the hill are deformed within 100 m of the base of the hill. A small stream with abundant water flow runs along the base of the hill, incising the deformed terrace sediments. The trees growing on this bulged terrace surface are tilted uniformly ~10° to the N (Figure 13, pic 2 looking west). Assuming the trees grew vertically, their tilt suggests some ground deformation has occurred within their lifetimes.

An OSL date from the sediments underlying the deformed alluvial surface is 3.1 ± 0.2 ka (Figure 5, Table 1). This Late Holocene age indicates that gravitational faulting is not limited to the early postglacial time but continues for thousands of years after ice retreat. The tilting of the trees, which are likely less than 200 years old, suggests they grew vertically and have been tilted within their lifetime, indicating that some of the deformation is recent. The extension related to the sackung process may be activated or increased by proximal shaking from earthquakes. The

data does not permit determination whether sackung slip occurs co-seismically or interseismically (i.e., creep), or to correlate deformation to an individual earthquake.

3.2.8 Site 8: Styx River

3.2.8.1 Mapping

The Styx site is located between the Styx and Kokatahi rivers where they converge and at the base of the range front along the Alpine Fault (Figure 2, site 8). The range front has a small saddle (Figure 14, location i) south of the Styx River which has been previously mapped as the location of a splay of the Kelly Fault (Langridge et al., 2016). Between the two rivers there is a large smooth arcuate alluvial fan (Figure 14, surface S1). In the centre of the fan, a secondary overtopping fan surface emanates from the range front saddle (Figure 14, surface S2). The stream (Figure 14, location ii) which deposited this top fan flows west and has incised deeply to meet the Styx River. The western edge of S1 is uplifted and deformed by the Alpine Fault (Figure 14, AFs and AFn), which has a ~300m wide left step as inferred from the fault trace normal distance between adjacent strands of the Alpine Fault PSZ (AFn and AFs). The left step has formed a pop-up structure (Figure 14, location iii), which deforms the western portion of the smooth S1 fan surface. West of the Alpine Fault, a fan surface remnant (Figure 14, surface S1b, location x), which is covered with ~N trending lineaments of unknown origin, may be correlative to the S1 surface east of the fault.

East of the Alpine Fault, on the north side of the S1 and S2 surfaces, a splay of the Kelly Fault strikes ~E-W and creates a 2-3 m high north facing scarp (Figure 14, location iv). North of this Kelly Fault scarp, a river cut forms the ~35 m high riser (Figure 14, location v) between the upper fan surface and a low relief fluvial terrace of the Styx River (Figure 14, surface S3). Where

the Kelly Fault splay meets the pop-up (Figure 14, location vi) the interacting faults form a series of steps that are likely fault scarps but also modified by low flow stream channels. There is a second E-W striking splay of the Kelly Fault crossing S2 expressed as a very small scarp (Figure 14, location vii). The south side of S1 is incised by a series of three fluvial terraces formed by the Kokatahi River which step down to the current river level (Figure 14, location viii).

In three locations we documented faulting of this fan and took some OSL and radiocarbon age control samples. These sites are individually described below.

3.2.8.2 1277 trench

The trench at 1277 is 2 m long and 1.5 m deep and trends 010° to expose the Kelly Fault splay and faulted stratigraphy (Figure 14 and Figure 15A). The lowest unit (gg) exposed is a gravel with rounded lenticular schist clasts, grey sandy silt matrix with imbricated clasts (Figure 15A). The imbrication orientation varies along the trench in three distinct sections: the northern section on the downhill end of the trench (ggN) has the long axis of the cobbles oriented with trend 130° plunge ~25° to the south, the middle section (ggM) has clasts with no preferred orientation, and the southern section (ggS) on the uphill side of the trench has average clast long axis trend 040° plunge 20°N. The top of unit gg is higher on the south (uphill) end than on the north (downhill end) and the central section is lower than either end. We interpret the central section as a fault zone. The disorganized clasts and disrupted top contact are attributed to disturbance of the sedimentary structure and shearing by the fault. Against the step between ggM and ggS, there is a small triangular section of sediment with clasts similar to gg that are completely disorganized and more fine sediment than gg below it (Figure 15A, location i). Above gg is rg, a reddish coloured pebble to cobble gravel with well rounded, spherical clasts and sparse matrix. Rg is present along the entire trench length, but the thickness is variable, and the top is very irregular (Figure 15A,

location ii). Because the clasts are mostly well rounded and spherical (rather than lenticular like in unit gg), no imbrication or any sedimentary structure could be identified, so it is unclear if this unit has been faulted, though the undulating top contact suggests it may have been disturbed by post-depositional faulting. Above the rg is tc, a tan clayey matrix rich unit with sparse clasts up to 5cm diameter. This unit drapes over the step in gg and rg, it pinches out at the south end of the trench and is thickest in the middle and thins again at the north end. The top unit in the trench is gs, a grey silt with ~20% clasts. It has a sharp lower contact with tc and rg where tc has pinched out at the south end. In the middle of the trench, the lower contact is obscured by slumping that occurred while digging the trench. This trench shows evidence of faulting, indicating that the scarp is formed by a fault and not a fluvially formed scarp feature.

3.2.8.3 1370 exposure

This natural exposure is in the north bank of the large stream channel at the base of the west edge of the fan (Figure 14 and Figure 15B). The east side of the exposure has highly sheared rock - unit b1 is hard and not easily scraped, while b2 is much softer and can be easily scraped, but they have similar grey colour and sheared texture. Gray clay gouge 1-3 cm wide (Figure 15B) separates the sheared rock from gravel on the west side of the exposure. The g1 gravel is coarse, poorly sorted, very angular, moderately weathered with reddish coloured matrix. The fault strikes 032° and dips 67° SE, so the sheared bedrock is thrust over the g1 gravel. Above the g1 reddish gravel is a lilac grey coloured sandy silt (g2) that we sampled for OSL (sample 1370B, Table 1, 6.4 ± 0.5 ka). This sediment is darker at the top, possibly indicating more organic material; we sampled the darker section for 14C (sample 1370C 1633-1805 CE, Figure 15C). Unit g2 is faulted, and between it and the bedrock there is a 10cm wide section of deformation where g1 and g2 sediments are mixed (g1d). Above g1 and g2 is g3, a coarse, poorly sorted gravel with grey silty

sand matrix with some brown mottling. Unit g3 also overlies the bedrock on the east side of the fault and does not appear faulted (Figure 15B location i). Overlying g3 and the bedrock is g4, a coarse well sorted uncemented sand with stratification that is roughly horizontal. This unit is partially obscured by vegetation, but it does not appear faulted. The base of the unit extends lower down into b2 (Figure 15B location i), which we interpret as being fluvial sand deposited within pre-existing surface topography, because the sand layers in the swale are parallel with the layers that extend across the entire outcrop and there is no apparent difference between the sediments in the hole and above the hole. Unit g4 was sampled for OSL dating (sample 1370A, Table 1, 4.7 ±0.5 ka).

3.2.8.4 1258 exposure

This exposure is in the main creek about 200 m upstream of the road on the north side of the stream (Figure 14 and Figure 15D, E). The stream is deeply incised into the fan with steep walls ~30 m high. The base of a small slip exposes in-situ sediments low in the fan stratigraphy (Figure 15D, E). The sediments are poorly to moderately sorted gravels, subrounded to angular, lens shaped clasts of grey schist with a silty sandy matrix. There are four distinct layers in the exposure, the base is a grey gravel, then above that is a medium grained grey sand layer that varies in thickness from 0-10 cm and is not continuous across the outcrop. Above the thin grey sand is a tan sandy gravel, with rounded to angular lenticular clasts of schist up to ~0.5m thick and is continuous across the outcrop. Above the tan gravel is a grey gravel similar to the basal unit.

The outcrop is faulted by multiple splays of NNE-striking and west-dipping faults (Figure 15D, E). These faults project up to the east edge of the pop-up structure at the top of the fan. The sandy and tan marker beds show that these faults have some component of reverse slip. The discontinuity and variable thickness of the sandy bed suggests there is strike-slip displacement

perpendicular to the plane of the outcrop that juxtaposes lateral variations in the bed thickness. In the faults, the clasts are rotated from horizontal to vertical or completely disorganized, and the matrix contains more clay. Measured in the outcrop, the faults strike 212-216° and dip 40-60° NW. The apparent displacement on each fault varies, and the apparent thickness of the marker units also varies. The maximum measured apparent dip-slip displacement on a single fault is 30 cm, the total vertical displacement across the outcrop is 2 ± 0.1m measured on the base of the tan gravel. The vertical displacement across the scarp on the fan surface associated with the outcrop is 1.8 ±0.2m (Figure 14C), indicating that most or all of the dip-slip displacement on this particular splay occurred after the fan sediment had accumulated and the surface became inactive.

3.2.8.5 Age control

Sample 1370A is from unit g4 (unfaulted) in outcrop 1370 (Figure 15B) at the west edge of the fan and yields an OSL age of 4.7 ±0.5 ka. Sample 1370B from the faulted unit g2 yields an OSL age of 6.4 ± 0.5 ka (Figure 15B, Table 1). Sample 1258A from the upstream outcrop, yields an age of 6.1 ± 0.6 ka (Figure 15D, Table 1).

The conventional radiocarbon age for sample J1370C (225 ±19 BP) yielded a 95% CI calibrated radiocarbon age of 1663-1805 CE with significant peaks at 1663-1686 CE (16.6%) and 1731-1805 CE (78.9%) (Figure 15C) (Bronk and Ramsey, 2020; Hogg et al., 2020). The calibrated calendar age has a large range because it occurs at a flat portion of the calibration curve. The material dated is a thin twig or possible root. If the sampled material was a detrital twig, its age represents the maximum depositional age of the sediment. If the sampled fragment is an ingrown root, it is a minimum age for the deposit because it indicates the deposit was in place before the age of the root, but it does not constrain the maximum age for the deposit.

At 1370, the OSL ages (1370A 4.7 ±0.5 ka, 1370B 6.4 ±0.5 ka) are an order of magnitude older than the radiocarbon, despite being from units both above and below the radiocarbon sample. The radiocarbon sample may be younger than either deposit if it is an ingrown root fragment. If the radiocarbon sample is of detrital origin it would represent the depositional age of the sediment, then the age discrepancy may be explained by the OSL samples being reworked, but not having the OSL reset. This is similar to the process we invoked to explain out of sequence luminescence ages in the upper Taramakau valley. If the sediments really were deposited within the last <1000 years, then the environment was likely similar to how it is today, with deeply incised channels and dense vegetation. In these conditions, sediments with a short transport distance may not have had enough sunlight exposure to completely bleach before being redeposited, resulting in inherited OSL age. In the Hope River valley, Khajavi et al. (2016) suggested a similar reworked but not reset process to explain 23 ka and 16 ka OSL ages from sediments underlying an apparently young (mid-late Holocene) alluvial fan.

Because unit g2 is faulted, but not unit g4, if the OSL ages accurately date deposition, then there would have been surface rupture on this fault splay >4,000 years ago then no surface ruptures since. The location of this site along the main Alpine Fault trace makes this interpretation unlikely.

Dated organic materials from the trench at 1277 (Figure 15A) are from the grey silt (unit gs, sample J1277gs), tan clayey silt (unit tc, sample J1277tc) and the red rounded gravel (unit rg, sample J1277rg), and they all returned modern ages (modern refers to post-1950). There have been no recorded surface rupturing earthquakes in this area historically and especially since 1950, so if the unit rg is faulted (see trench description for discussion of this uncertainty), the radiocarbon sample material is likely ingrown roots, because to be faulted the sediments must be older than 1950. The modern sample age for units tc and gs may be accurate to their depositional age, but

this does not offer additional constraints on the timing of the last surface rupture as it is already known to be older than 1950 because there has been no historic surface rupture here. These modern 14C ages highlight the difficulty in differentiating between rootlets and detrital twigs in areas with abundant vegetation.

3.2.8.6 Slip-rate

These three exposures and the morphologic mapping are consistent with the interpretation that S1 is an alluvial deposit that has been uplifted by the hanging wall of the Alpine Fault (Figure 14A). Faulting is documented on morphologic scarps on both the east (exposure 1370, Figure 15B) and west (exposure 1258, Figure 15D) sides of the pop-up on faults parallel to the Alpine Fault, and also on an east-west striking splay of the Kelly Fault east of the pop-up (trench 1277, Figure 15A). The OSL sediment ages indicate that the fan sediment is 6.1 ±0.5 ka, so this fan is mid-Holocene in age. We were unable to identify any laterally displaced features that could be correlated across the faults with an absolute age to get a lateral slip-rate measurement. The eastern side of the S1 fan surface appears undeformed but is uplifted in the hanging wall of the Alpine Fault. The surface remnant west of the Alpine Fault (Figure 14 A, S1b) may correlate with S1 east of the fault, allowing measurement of a vertical slip-rate. We do not have observations on the stratigraphy or age of the western surface remnant, only the surface morphology. Assuming S1 and S1b are correlative, projection of both surfaces to the main trace of the Alpine Fault yields 21.5 ±3.5 m of vertical displacement (Figure 14B). This measurement disregards the vertical displacement within the pop-up, because this structure is formed primarily by the lateral slip on the fault and is not representative of the vertical or dip-slip-rate below the surface complexities. The resulting dip-slip-rate of the Alpine Fault, using J1258A as the maximum age, is 6.3 (+3.2/-1.9) mm/yr dip-slip assuming a 50 ±10° E fault dip (Table 3).

3.2.8.7 Earthquake timing

The radiocarbon sample J1370C (1663 - 1805 CE, Figure 15 B and C) was taken from sediments faulted by at least one surface rupture on the Alpine Fault main trace. If the dated twigs are actually rootlets, their age is younger than the sediment deposition. However, if they are detrital twigs, the sample age represents the depositional age of the sediment and is a maximum age for at least one surface rupture. The sample has a large calibrated age range (Figure 15C), and we lack additional stratigraphically related samples that can be used for OxCal modelling to constrain the depositional age more precisely. The age range is such that the post-depositional surface rupture could have been the 1717 Alpine Fault earthquake, or the more recent early 1800's Alpine Fault earthquake identified 3 km to the south (Langridge et al., 2020) and in Lake Kaniere (Howarth et al., 2021).

3.2.9 Lake Kaurapataka tree

Lake Kaurapataka is an alluvial fan-dammed lake ≥23 m deep that sits in the valley south of Sackung Hill (section 2.6) along the trend of the Kelly Fault zone. At the lake Kaurapataka, multiple decaying tree stumps sit in shallow water (<0.5m deep in summer) along the shores, the most easily accessed are along the southeast shore (Figure 16A and B). The stumps were mature, >0.5 m diameter trees that are presumed to have grown in their current locations when the lake level was lower, then died due to drowning when the lake level rose (Figure 16C). The lake drains to the west into Pfeifer Creek. The geomorphic mapping and field investigations reveal at least two generations of fans along the outlet stream of the lake. The oldest fan surface remnant extends the furthest down the valley away from the lake (Figure 16A, alluvial fan 1). The younger fan (Figure 16A, alluvial fan 2) has deposited on the east side of the old fan remnant (Figure 16A alluvial fan 1) and presently dams the lake. The fans are incised by the source stream flowing from

the south, and also by a stream originating at the lake. There is a unvegetated, lobate debris flow deposit on top of the younger alluvial fan surface (alluvial fan 2, Figure 16A). The stream emanating from the lake has a large knickpoint in the channel downstream of the lake outlet, and during dry times the lake only drains via groundwater in the fan deposits and does not drain over the surface of the fan. Incisional cut banks in the stream flowing from the south have revealed weathered paleosol covered with younger (unweathered) coarse, angular alluvial sediment, these are interpreted to be the sediments of the older fan topped by sediments of the younger fan.

OxCal modelling of the ^{14}C ages of two outer rings indicate that the tree likely died in 1753-1848. The number of rings between the two dated rings could not be counted because of poor wood quality. However, using the width of the rings from other nearby trees, we assume that there were ~20 rings between the dated rings. The death of the drowned tree provides a robust minimum age for the deposition of the younger lake-damming alluvial fan (Figure 16A, alluvial fan 2). Large landslides often occur as a result of strong ground shaking, so the landslide, damming of the lake, and subsequent tree death may be considered as a potential strong shaking proxy that can help constrain the timing of a proximal earthquake. Similar methods have been used at Lake Poerua on the coastal plain (Figure 2), where Langridge et al (2012) used death ages of drowned trees to date two generations of alluvial fan deposition at the lake outlet. These periods of increased sedimentation were coincident with previously determined Alpine Fault surface rupturing earthquakes, indicating the increased sedimentation that formed the alluvial fans were driven by coseismic shaking.

4. Coulomb Stress Transfer Modelling

4.1 Theory and Methods

An earthquake reduces stress on the source fault (i.e., coseismic stress drop) and redistributes stress in the lithosphere surrounding the source fault, with some areas increasing in stress, and others decreasing (stress shadows, e.g., Harris and Simpson 1998). Areas with increased Coulomb stress are areas where aftershocks and/or future earthquakes are hypothesized to be more likely (King et al., 1994; Stein et al., 1997; Toda et al., 1998; Harris et al., 1995).

Coulomb stress change on a receiver fault (CFS) is calculated using the equation (King et al., 1994):

$$\Delta CFS = \Delta\tau - \mu\,(\Delta\sigma + \Delta P)$$

where ΔCFS is the Coulomb failure stress, $\Delta\tau$ is the change in shear stress, μ is the coefficient of friction, $\Delta\sigma$ is the change in normal stress and ΔP is the change in pore fluid pressure. The location, strike, dip, and rake of the receiver faults affect the CFS (e.g., Lin and Stein, 2004; Steacy et al 2005), thus the geometry of the faults in the system are needed to robustly calculate CFS. Coulomb stress change from a source fault (the one with the earthquake) onto a receiver fault can increase or decrease the CFS, hence promoting or delaying failure. Modelling along-strike variations in geometry along a single fault has been shown to be important (Mildon et al., 2016). Rectangular discretization of a fault surface is used to create variable fault geometry, based on surface observations, to model the CFS resulting from representative earthquakes in the fault system. The main faults in the Alpine-Kelly-Hope Fault network have been discretised with variations in strike, dip and rake, following the approaches of Mildon et al. (2016) and Hughes et al. (2020). We conducted CFS modelling using Coulomb 3.4 (Toda et al., 2005). The current version of the code is available at https://github.com/ZoeMildon/3D-faults.

The magnitude of seismic hazard depends on how and whether earthquakes co-seismically propagate onto other faults, or trigger temporally clustered rupture of other faults. Complex earthquakes (Kaikōura, Darfield, Ridgecrest) have been observed to propagate along many faults (Hamling et al., 2017; Quigley et al., 2019; Ross et al., 2019). Multi-fault earthquake scenarios are being included in seismic hazards (e.g., Uniform California Earthquake Rupture Forecast; Field et al. 2014). Earthquake occurrence depends not only on geometry but also pre-stress from interseismic stress accumulation and prior coseismic stress changes (Mildon et al., 2017, 2019). CFS can be used to model cascading ruptures in steps, looking at the absolute or relative CFS on different faults in a network to determine which might be preferred by the rupture as it continues (Parsons et al., 2012; Quigley et al., 2019). This is the approach utilized here by modelling earthquake ruptures that terminate at the edge of the intersection zone or at geometrically significant junctions within it. With these stepwise static CFS models, we can evaluate how stress is distributed through the fault system as a rupture progresses through the system.

4.2 Fault model construction

We constructed a discretised version of the 3D fault model from Vermeer et al. (2021) with 1x1 km rectangular elements created using the process outlined in Mildon et al. (2016) and Hughes et al (2020) (Figure 17), with updates to enable along-strike variations in rake to be modelled. This fault model is a simplified generalization of the Hope-Kelly-Alpine intersection zone, especially in the western Kelly Fault area, where the diffuse faulting has been generalized into four splays of the Kelly Fault that follow the trends of mapped strike and approximate dip, located along some of the most continuous mapped fault traces. In reality the fault system may be more discontinuous and segmented into many smaller structures (Vermeer et al., 2021), but this approximation

provides useful insights into the stresses acting on the numerous smaller faults with similar orientations.

The rake values of Hope and Kelly Fault splays are taken from the model of Vermeer et al. (2021), calculated using rigid block assumptions and relative neutral intersections with the Alpine Fault (Figure 17). The Alpine Fault was assumed to be planar with a 50° SE dip down to the base of the model at 15 km. East of the intersection with the Alpine Fault plane, fault rake is determined from the displacement measurements determined in this study.

In the upper Taramakau Valley, the Hope and Kelly Fault traces are within 2 km of each other, strike subparallel and dip steeply (>75°). Based on the higher slip-rate on the Kelly Fault and because it is the along-strike projection of the Hurunui section, we decided to make the Kelly Fault dominant over the Hope in the upper Taramakau River valley where they are sub-parallel. At the 1 km element resolution, the Hope Fault could not be effectively modelled, so between Michael Creek and Harper Pass, the Hope Fault is not modelled separately from the Kelly Fault. Nevertheless, because of their similar orientation and dextral rake, the CFS results would likely be similar for the two faults.

Outside the area of the Vermeer et al. (2021) fault model, we use the Alpine and Hope Fault traces and dip from the New Zealand Active Fault Database (NZAFD; Langridge et al., 2016). Rake was calculated using slip-rate displacement measurements (Norris and Cooper, 2001; Langridge et al., 2010; Khajavi et al., 2016).

4.3 Modelled earthquake scenarios

The six modelled earthquake scenarios are detailed in Table 4, three earthquakes are modelled on the Alpine Fault, one on the Hope Fault and two on the Kelly Fault. Source ruptures

are terminated at points where the earthquake meets a structural complexity such as a branching node on a major fault. None of the models are specifically based on historic earthquakes but are meant to be representative scenarios that may be characteristic of the faults. Displacement is scaled with rupture length and Mw and slip distributions progressively reduce to zero at the rupture end points. The proportion of slip at the surface relative to slip at depth was chosen based on Dolan and Haravitch (2014), based on estimated cumulative slip of each fault (central Hope Fault up to 13 km, Langridge et al., 2013; Kelly Fault <2 km, Nathan et al., 2002). The full Kelly Fault southern splay rupture has a high maximum displacement in order to reach the desired magnitude on the westward, vertically decreasing fault area where the fault intersects the Alpine Fault. The modelled Alpine Fault rupture through the intersection zone has a homogenous slip distribution so specific earthquake parameters would not affect the resulting pattern of CFS. All the source earthquakes modelled are finite fault slip solutions rather than reflecting the progressive dynamic rupture of an earthquake. A propagation direction can be incorporated into the interpretation by using the resulting CFS at a fault intersection to evaluate which splay might be preferred for continued rupture (Parsons et al., 2012), but the models themselves have no assigned propagation direction.

4.4 Results

4.4.1. Alpine Fault earthquakes

Figure 18 shows the resulting CFS from three representative Alpine Fault earthquakes. The first (Figure 18, A1) is an earthquake on the central Alpine Fault with the north end of the rupture at the surface intersection of the southern splay of the Kelly Fault and the Alpine Fault (essentially stopping just south of the Styx site, Figure 18 A2). This earthquake positively stresses the Alpine Fault north of the rupture termination, and the entire Hope-Kelly Fault system. The magnitude of

positive stress broadly decreases with distance from the rupture termination, but also displays variation among fault planes at similar distances due to variations in fault geometry. For example, the Kelly Fault splay tips receive higher positive stress change than the immediately adjacent Alpine Fault plane (Figure 18 A1). The magnitude of positive stress on the southernmost splay of the Kelly Fault is variable along its length, being lowest where the fault is modelled as sub-parallel to the Alpine Fault and primarily dextral slip, and higher on sections with strike more obliquely to the Alpine Fault strike (Figure 18 A1).

The next simulated earthquake is a northern Alpine Fault rupture that reaches the Hope-Alpine surface intersection (Figure 18 B1). This earthquake results in primarily negative stress change on the Hope-Kelly Fault system (Figure 18 B2). The Alpine Fault south of the source receives positive stress change. The western tips of the Kelly Fault splays receive a patchy pattern of low positive and negative stress change (Figure 18 B2). The strongest negative stress change occurs on the westernmost Hope Fault, where it has normal slip and E-W strike, and on the eastern end of the Kelly Fault splays (especially K3 and K4) (Figure 18 B2).

We modelled the stress change for an earthquake rupturing completely through the intersection; for this scenario we used a constant 5 m displacement on the entire Alpine Fault including extending beyond the intersection zone (Figure 18 C1). On the Alpine Fault in the centre of the intersection zone, where the fault bends by ~3°, the model has artifacts of positive stress on the Alpine Fault (Figure 18 C2). Overall, the Hope-Kelly Fault system receives negative stress change from an Alpine Fault earthquake rupturing all the way through the intersection zone (Figure 18 C2), though there may be minor regions of positive stress at the base of the Kelly splay faults.

These models overall show that rupture of the central Alpine Fault positively stresses the Hope-Kelly Fault system (Figure 18 A2). If there was an earthquake on the central Alpine Fault

(south of the Hope-Kelly system), this broadly transfers positive CFS to the Hope-Kelly Fault system. This implies that a subsequent earthquake may be triggered on the Hope-Kelly system. If an earthquake rupture extends through the intersection zone or occurs on the northern Alpine Fault, the Hope-Kelly Faults receive mainly negative stress (Figure 18 C2 and B2). This implies that southward-propagating earthquakes originating on the northern Alpine Fault are expected to inhibit rupture nucleation (i.e., bypass) on the Hope-Kelly system and preferentially continue on to the central Alpine Fault.

4.4.2. Hope-Kelly Fault earthquakes

Three earthquake scenarios were modelled for the Hope-Kelly Fault system (Table 4). The first is a central Hope Fault earthquake on the Hurunui section that ends at Harper Pass (Figure 19 A1). Because of the model resolution and the proximity of the faults, the Hope Fault is not modelled between Michael Creek and Harper Pass (Figure 19 A1). The Kelly Fault is selected to be the primary structure west of Harper Pass because slip-rates show it accommodates most of the strain (Section 3.2.1 – 3.2.5). From this hypothetical earthquake scenario, west of Michael Creek as the Hope and Kelly Faults diverge, the Kelly Fault receives greater positive stress than the Hope Fault (Figure 19 A3). There is a small (<2 bars) positive stress change on the central Alpine Fault and on the southern end of the northern Alpine Fault at depths greater than ~10 km (Figure 19 A3); above 10 km depth the northern Alpine Fault receives negative CFS.

The next earthquake modelled is a Hope Fault (Hurunui section) to central Kelly Fault earthquake (Table 4); this source rupture extends west to ~10 km east of the Alpine Fault where the Kelly and Alpine Faults intersect near the base of the seismogenic zone (Figure 19 B1 and B3). This earthquake scenario produces higher magnitude positive stress change on the K2 and K3 splays than the western extent of the southern splay (Figure 19 B3). This suggests that even though

the southern splay is often considered the “main splay” of the fault system, the other Kelly Fault splays, and likely the diffuse unmodeled faults, receive high positive stress that may initiate slip on those faults (Figure 19 B2). The westernmost section of the Hope Fault receives positive stress, but at a much lower magnitude relative to the Kelly splays (Figure 19 B3). The northern Alpine Fault receives only negative stress, but the central Alpine Fault receives positive stress, especially at depth where it is close to and directly interacting with the slipped fault (Figure 19 B4).

The final earthquake modelled in this sequence is a complete rupture of the southern splay of the Kelly Fault from Harper Pass to the surface intersection with the Alpine Fault (Table 4, Figure 19 C1). In the CFS results, the positive stress patches on the source fault are an artifact (Figure 19 C2 and C3). This earthquake mostly reduces stress on the other Kelly splays and the western Hope Fault, with the exception of a small patch of positive stress near the Hope-Kelly divergence point (Figure 19 C2). This earthquake produces a large positive stress change on the central Alpine Fault along the intersection (Figure 19 C3), while the northern Alpine Fault stress is reduced (Figure 19 C2). This earthquake extends east to Harper Pass, and it produces a positive stress change on the Hurunui segment of the Hope Fault (Figure 19 C2 and C3).

Combining insights from all three models on the Hope-Kelly Fault system, there is change in the pattern of CFS associated with a change in the proportion of the fault system that ruptures. If an earthquake ruptures the Hope/eastern Kelly Fault up to Michael Creek, the Kelly splays and the central Alpine Fault all experience positive stress (Figure 19 A2-3 and B2-3). Therefore the earthquake may propagate onto any of the splays. If an earthquake ruptures along the entire length of the southernmost Kelly Fault splay, the rest of the Hope-Kelly Fault system experiences mostly negative stress, but the central Alpine Fault experiences positive stress (Figure 19 C2-3). Therefore

a common feature of earthquake ruptures on the Hope-Kelly Fault system is that the central Alpine Fault is positively stressed.

5. Discussion

5.1. Slip-rate variations through the Hope-Kelly Fault system: discrete and distributed strain in an incipient fault interaction zone

The estimated slip-rates for the Hope and Kelly Faults are highly variable, between 1 and >6 mm/yr over a distance spanning only ~15 km along strike, highlighting the complexity of the fault system. Overall, the Kelly Fault has a faster late Quaternary slip-rate than the westernmost Hope Fault. In the area studied here, the Hope and Kelly principal slip zones are close together (within 1 - 5 km perpendicular to strike, across the valley) and both have a discontinuous mappable surface trace, with many other low displacement, short faults mapped in the distributed deformation zone. There could be un-measured slip on structures between and around the principal slip zone segments where we have measured slip-rates; distributed deformation within complex and young fault systems is anticipated (Dolan and Haravitch, 2014; Zinke et al., 2014).

To infer how much unrecognized slip may be within the Hope-Kelly Fault system, we use horizontal slip vector balancing with the surrounding faults, according to the methods of Langridge et al. (2010) and Vermeer et al. (2021). In this process only one slip vector measurement or an average slip vector should be used from each fault in the system, and slip vectors from parallel faults should be added to capture the slip across the whole width of the fault system. In this case we use the Locke Stream slip-rate for the Kelly Fault (section 3.2.3 Site 3, 6.2 (+2.7/-1.4) mm/yr) and the Yeo Creek measurement for the Hope Fault (section 3.2.2. Site 2, 5.6 (+2.1/-0.7) mm/yr) (Figure 20A). Alternatively, the rate from Site 5: KF3 (west of Sackung Hill) could be used alone, since at this point in the fault system much of the dextral slip from the Hope Fault has been

transferred onto the Kelly Fault (see section 2.6.4 for discussion of Hope-Kelly linking faults exposed on Sackung Hill). Compared to the average slip vector on the Hurunui segment (Khajavi et al., 2018), the Hope and Kelly Faults have a combined horizontal slip vector that is within error of the Hurunui average slip vector (Figure 20 B). However, the average Hurunui section slip vector is determined at sites east of the Hurunui-Kakapo fault intersection, so it may be an underestimate of the slip-rate on the western Hurunui section which turns into the Hope-Kelly Fault system (Khajavi et al., 2018). Slip-rate estimates at Harper Pass are ~15 mm/yr (Hardy and Wellman, 1984; Langridge and Berryman, 2005). The slip-vector balancing in Langridge et al. (2010) used McKenzie Fan on the Hurunui section (Figure 1, location 5), plus the Kakapo fault (Figure 1, location 12) slip vectors to balance with the central to northern Alpine Fault slip vector change (Figure 1, locations 1 and 3). We subsequently compare the slip vectors measured in the Hope-Kelly Fault system to the slip vector change on the Alpine Fault (Figure 20 C). We expect that all the deformation in the Hope-Kelly Fault system on the combined vectors would fill the gap between the central Alpine Fault and northern Alpine Fault slip vectors. However, the slip vectors measured do not entirely fill the gap. There is 5-7 mm/yr at 090 ± 15° unaccounted for (Figure 20). The missing slip may be distributed among many low displacement structures, or accommodated on structures without surface expression appropriate for making slip-rate measurements.

Estimated slip-rates are based on displaced early post-glacial to early Holocene landforms, with total slip accumulated over 7-16 kyr. Most of the slip-rate measurements on the central Hope Fault and Alpine Fault are from displaced late Holocene landforms less than 5 kyr (see references in Figure 1). Studies on the Hope Fault and other MFS faults have shown that slip-rates on single fault segments or at single sites covering different time windows vary through time (Gold and

Cowgill, 2011; Khajavi et al., 2018; Zinke et al., 2019; Hatem et al., 2020; Zinke et al., 2021). This temporal variability in slip-rates may be an additional factor in why the measured Hope-Kelly slip vectors are in deficit to the central-northern Alpine Fault slip-rate change, and do not balance like the late Holocene Alpine-Hope-Kakapo slip circuit.

5.2. Timing of MRE on the Hope-Kelly Fault relative to adjacent fault segments and Alpine Fault earthquakes

The paleoseismic trenching and dating of possible shaking proxies (damming of Lake Kaurapataka and tree death) provide preliminary constraints on the timing of the most recent surface rupturing earthquake on the Hope-Kelly Fault system. The ^{14}C date in faulted sediment on the Hope Fault at Site 1: Michael Creek (Section 2.1.5) constrains the age of surface rupture to between ca. 1650-1840 CE, the latter bound being constrained by widespread European settlement and the absence of a large earthquake being recorded. The trench and subsequent ^{14}C sampling did not provide sufficient stratigraphy and material to constrain this age further; the wide age range is a consequence of the flat shape of the ^{14}C calibration curve around the time interval in question. However, assuming the large landslide which dammed Lake Kaurapataka was due to proximal strong shaking, the death age of the tree indicates that the earthquake occurred in the early 1800's. Indicators of strong shaking have also been recognized in Lake Kaniere, east of the Alpine Fault, near Site 8: Styx, which is dated at 1809-1880 CE (Howarth et al., 2021). This has been connected to the proposed post-1717 surface rupture dated at 1813-1848 CE on the Alpine Fault in paleoseismic trenches at Staples (Figure 1, location 2), just south of the Styx site (Langridge et al., 2020). Finally, there is no post-European colonization historic record of a strong earthquake in this region, limiting the minimum age to before ~1840.

Langridge et al. (2020) attributed the early 1800's Alpine Fault surface rupture at Staples (Figure 1 site 2) to either a short partial section rupture of the Alpine Fault, or triggered slip from an earthquake primarily on the Hope-Kelly Faults. Preliminary data is consistent with the latter interpretation, however it is not conclusive. The isoseismals for a M 7.4 northern Alpine Fault earthquake presented by Langridge et al (2020) have strong shaking overlap with the Lake Kaurapataka area, so the landsliding there may not be exclusively triggered by Hope-Kelly earthquakes but also Alpine Fault earthquakes. To explain the shaking proxies and surface rupture observations along the Alpine Fault, Langridge et al. (2020) preferred the interpretation that the early 1800's Alpine Fault surface rupture was from an earthquake primarily on the Kelly Fault which triggered Alpine Fault slip with a limited spatial extent. This scenario is within the possible interpretations of the Hope-Kelly Fault earthquake dating. However, considered without shaking proxies, the depositional age of faulted sediments at Michael Creek does not constrain the age of the surface rupture with enough certainty to determine whether it was coincident with ruptures on other proximal faults in the Alpine-Hope-Kelly Fault region during the ~200 year interval between 1650-1840.

5.3. Stress modelling and fault interactions

As indicated from CFS modelling, earthquakes on the central Alpine Fault could exert up to 10 bars of positive Coulomb stress on parts of the Hope-Kelly Fault system. However, ruptures on the Alpine Fault which pass completely through the intersection zone and earthquakes limited to the northern Alpine Fault both decrease Coulomb stress on most of the Hope-Kelly Fault system. Earthquakes on the southern Kelly Fault splay substantially decrease Coulomb stress on the northern Alpine Fault but could impart large (>20 bars) positive stress change on the central Alpine Fault. Earthquakes on the southern Kelly Fault splay also impart positive stress on the Hurunui

section of the Hope Fault, and vice-versa. These patterns of stress interaction suggest that the Hope-Kelly Fault system is a stress-efficient link between the central Alpine Fault and the Hope Fault. The magnitude of positive stress changes modelled in many of the rupture scenarios investigated herein exceed the estimates of threshold triggering Coulomb stress changes estimated from other scenarios. A Coulomb stress increase of 0.01 MPa (0.1 bar) is commonly proposed to be the threshold for potential earthquake triggering (Harris, 1998; Reasenberg and Simpson, 1992; Freed, 2005; King et al., 1994; Stein, 1999), although Coulomb stress changes of > 0.1 MPa (Zhan et al., 2011) and 1 to 1.5 MPa (Walters et al., 2018) were insufficient to generate spontaneous rupture during the 2010–2011 Canterbury earthquake sequence and 2016 Central Italy seismic sequence, respectively. Mohammadi et al. (2019) estimated a Coulomb stress change threshold sufficient to trigger receiver fault rupture of ca. 1 to 4 bars based on an analysis of global events.

The location of the central-northern Alpine Fault section boundary was primarily determined by the slip-rate change and the presence of the Hope-Kelly-Alpine intersection which marks the southern extent of the MFS. Although there is a slight bend in the Alpine Fault within the Hope-Kelly intersection zone, there is no recognized geometric feature in this region on the Alpine Fault large enough to stop an earthquake rupture, according to global databases of strike-slip fault complexities (e.g. Wesnousky, 2006; Lozos et al., 2011; Elliott et al., 2015; Biasi and Wesnousky, 2016; Biasi and Wesnousky, 2017; Elliot et al., 2018). However, this CFS modelling shows the Hope-Kelly Fault system may impart a complex stress pattern on the Alpine Fault. If a northward propagating rupture on the central Alpine Fault was sufficient to trigger slip on the Kelly Fault splays at the same time as the continuation of the Alpine Fault rupture, the interaction of static stresses would be complex. Slip on the central Alpine Fault positively stresses the northward continuation of the Alpine Fault through the intersection zone but slip on the southern

Kelly splay causes negative stress on the Alpine Fault plane north of the ruptured portion of the Kelly Fault. Depending on the relative stresses, pre-stresses, and other dynamic factors not captured by this modelling, it is conceivable that the Hope-Kelly-Alpine intersection could arrest a northward propagating central Alpine Fault rupture by producing competing stresses on the Alpine Fault plane within the intersection zone.

Ruptures on the Hope-Kelly Fault system cause negative CFS on the northern Alpine Fault. The other MFS faults may exert a similar pattern of positive stress change south of the intersection and negative stress change north of the intersection. This complex spatial and temporal patchwork of stress change exerted on the northern Alpine Fault could make the behaviour of the fault spatially and temporarily heterogeneous. Paleoseismic work on the northern Alpine Fault has not resulted in well-accepted precise age distributions and rupture extents of Holocene earthquakes (Yetton, 1998). At this stage, we can conclude that Coulomb stress changes associated with northern and central Alpine Fault earthquakes generate distinct patterns on the Hope-Kelly receiver faults that may be important in dictating rupture propagation onto adjacent parts of the Alpine Fault and the Hope-Kelly Fault system.

The transfer of coseismic Coulomb stresses between the Alpine and Hope-Kelly Faults could affect the millennial-scale pattern of earthquakes, slip-rates and recurrence intervals of all the faults involved. Work on the central and southern sections of the Alpine Fault show it may exhibit diverse rupture modes that could vary over 5-10 kyr timescales when it preferentially stops at the central-southern section boundary vs propagates through it (De Pascale et al., 2014; Howarth et al., 2021). If this behaviour also holds true at the central-northern section boundary, when the Alpine Fault is in central-northern dual-section mode it would repeatedly rupture through the section boundary and decrease stress on the Hope-Kelly Fault system. Inversely, when the Alpine

Fault is in single-section mode, central section earthquakes would repeatedly stop near the central-northern boundary and impart positive Coulomb stress on the Hope-Kelly Fault system. While less frequent and/or lower displacement (due to lower slip-rate) northern section earthquakes may alternately decrease the stress, overall, the Alpine Fault in single-section rupture mode would likely produce a net increase in Coulomb stress and promote more frequent ruptures of the Hope-Kelly Faults. This could in turn promote more frequent rupture of the Hurunui section of the Hope Fault. If this pattern persisted over multiple earthquake cycles, the 5-10 kyr slip-rate on the Hope-Kelly system and potentially the Hurunui segment during that time would be faster than the long-term average. Alternatively, when the Alpine Fault is in a dual-section rupture mode, each rupture through the intersection zone and on the northern Alpine Fault would decrease the Coulomb stress on the Hope-Kelly Fault system. The repeated negative CFS may impede rupture nucleation, potentially increasing recurrence intervals and decreasing slip-rate on the Hope-Kelly Fault system while the Alpine Fault is in dual-section mode. Future work understanding the tendency for single vs dual-section ruptures of the central to northern Alpine Fault should include the effects of the stress transfer interactions with the MFS faults. Also, partial section rupture of the northern Alpine Fault may be promoted by stress interactions at each of the MFS intersections.

5.4. Implications for seismic hazard and plate boundary faulting mechanics

The slip-rates presented here are the first for the Hope-Kelly Fault system and the western Hope Fault. In the eastern part of the fault system, the Hope and Kelly Faults are close together and interact within the upper 5 km of crust. As they diverge, the Hope Fault slip-rate decreases to <2 mm/yr of dextral slip, while the Kelly Fault maintains 6.2 (+7.8/-1.2) mm/yr. Up to 7 mm/yr of slip (up to 50% of strain) is unaccounted for in HSV balancing with the Alpine Fault, indicating

that slip distributed onto low displacement and/or unrecognized faults likely plays an important role in this intersection zone.

Coulomb stress transfer modelling using the 3D fault geometry shows that the central Alpine Fault, Kelly Fault, and Hurunui section of the Hope Fault form a kinematically efficient stress-transfer zone. Central Alpine Fault earthquakes almost equivalently increase Coulomb stress on the Kelly Fault splays and northern continuation of the Alpine Fault. If CFS is the main factor in determining fault behaviour, central Alpine Fault ruptures could be expected to cascade either onto the Hope-Kelly Faults and/or continue on the northern Alpine Fault with roughly equivalent probability. This is congruent with the observation that approximately 50% of the central Alpine Fault slip continues onto the northern Alpine Fault, and the other 50% is transferred through the intersection onto the central Hope Fault, as inferred from slip rates (Langridge et al., 2010). Meanwhile, the repeated negative CFS exerted on the northern Alpine Fault by Hope-Kelly ruptures may repeatedly inhibit rupture nucleation on that section. This pattern of stress may be similar at each MFS-Alpine Fault intersection, potentially causing spatial and temporal variations in rupture behaviours of the northern Alpine Fault.

6. Conclusions

- The Hope Fault slip-rate decreases westward from 5.6 (+2.1/-0.7) mm/yr to 1.7 (+1.1/-0.4) mm/yr. West of this point the Hope Fault strike bends to 090 ±10° and there is no unambiguous surface expression of the fault.
- The Kelly Fault has variable slip-rate along its length, with a maximum measured slip-rate of 6.2 (+7.8/-1.2) mm/yr. We consider the Kelly Fault to be the principal fault in the central and eastern parts of the Hope-Kelly Fault system.

- ^{14}C dating of faulted sediments on the Hope Fault and shaking proxies constrain the most recent surface rupture in the Hope-Kelly Fault system to between 1653 - 1848 CE.
- Horizontal slip vector balancing shows that the new slip-rates on the Hope and Kelly Faults match the average slip-rate of the eastern Hurunui segment of the Hope Fault but fall short of accounting for all the slip-rate transferred off the Alpine Fault across the intersection zone. The missing 5-7 mm/yr of strain may be accommodated by distributed deformation on small and/or unrecognized faults within this complex and diffuse fault system.
- CFS modelling shows that the Hope-Kelly Fault system is a stress-efficient link between the central Alpine Fault and the central Hope Fault. Slip on each of these fault sections causes positive CFS on the others and may cause rupture cascades or temporal clustering of earthquakes through the intersection zone.
- CFS modelling suggests it is unlikely for a Hope-Kelly rupture to induce rupture of the northern Alpine Fault and vice versa, because these sections of the fault system exert primarily negative CFS on each other.

Acknowledgements

JV acknowledges the support of a University of Melbourne International Research Scholarship and the Baragwanath Trust. RML was funded through GNS Science research programs TSZ and ZLD 2.2.2 South Island Paleoseismology. Lidar acquisition was funded by the New Zealand Earthquake Commission through an Earthquake Commission Capability Fund grant to MQ, and Jarg Pettinga. Additional funding for this research was provided through an Australian Research Council Discovery Project Grant (#DP170103350). ZM acknowledges NERC Studentship [NE/L501700/1], JSPS Fellowship PE 15776 and UKRI Future Leaders Fellowship

[MR/T041994/1] for support to develop the Coulomb modelling approach. MD acknowledges University of Plymouth PhD studentship. Permits for sampling and fieldwork were provided by the Department of Conservation (DOC). We thank the property owners Ed and Michelle Evans for access to their properties and for lodging and logistical support. We thank Andrew Wilson, Santosh Dhakal, Naomi Leclere, Mindi Curran, and Hector Flores for field assistance. We thank Andrew Murray and Vicki Hansen (Nordic Laboratory for Luminescence Dating, Aarhus University and DTU Risø Campus in Denmark) for conducting luminescence dating of these samples and discussing their interpretation. We acknowledge the mana whenua of Ngāti Waewae and Ngāi Tahu as kaitiaki over Te Tai Poutini.

References

Aki, K., and Richards, P.G., 1980, Quantative seismology: Theory and methods. Quantative Seismology: Theory and Methods: San Francisco, CA, Freeman.

Barrell, D.J.A., Andersen, B., and Denton, G., 2011, Glacial geomorphology of the central South Island, New Zealand. GNS Science monograph 27:, http://shop.gns.cri.nz/mon27/.

Barrows, T.T., Almond, P., Rose, R., Fi, L.K., Mills, S.C., and Tims, S.G., 2013, Late Pleistocene glacial stratigraphy of the Kumara-Moana region , West Coast of South Island , New Zealand: v. 74, doi: 10.1016/j.quascirev.2013.04.010.

Biasi, G.P., Weldon, R.J., Fumal, T.E., and Seitz, G.G., 2002, Paleoseismic event dating and the conditional probability of large earthquakes on the southern San Andreas fault, California: Bulletin of the Seismological Society of America, v. 92, p. 2761–2781, doi: 10.1785/0120000605.

Biasi, G.P., and Wesnousky, S.G., 2016, Steps and gaps in ground ruptures: Empirical bounds on rupture propagation: Bulletin of the Seismological Society of America, v. 106, p. 1110–1124, doi: 10.1785/0120150175.

Biasi, G.P., and Wesnousky, S.G., 2017, Bends and ends of surface ruptures: Bulletin of the Seismological Society of America, v. 107, p. 2543–2560, doi: 10.1785/0120160292.

Cochran, U.A., Clark, K.J., Howarth, J.D., Biasi, G.P., Langridge, R.M., Villamor, P., Berryman, K.R., and Vandergoes, M.J., 2017, A plate boundary earthquake record from a wetland adjacent to the Alpine Fault in New Zealand refines hazard estimates: Earth and Planetary Science Letters, v. 464, p. 175–188, doi: 10.1016/j.epsl.2017.02.026.

Cowgill, E., 2007, Impact of riser reconstructions on estimation of secular variation in rates of strike-slip faulting: Revisiting the Cherchen River site along the Altyn Tagh Fault, NW China: Earth and Planetary Science Letters, v. 254, p. 239–255, doi: 10.1016/j.epsl.2006.09.015.

De Pascale, G.P., Quigley, M.C., and Davies, T.R.H., 2014, Lidar reveals uniform Alpine Fault offsets and bimodal plate boundary rupture behavior, New Zealand: Geology, v. 42, p. 411–414, doi: 10.1130/G35100.1.

Dolan, J.F., Bowman, D.D., and Sammis, C.G., 2007, Long-range and long-term fault interactions in Southern California: Geology, v. 35, p. 855–858, doi: 10.1130/G23789A.1.

Dolan, J.F., and Haravitch, B.D., 2014, How well do surface slip measurements track slip at depth in large strike-slip earthquakes? The importance of fault structural maturity in controlling on-fault slip versus off-fault surface deformation: Earth and Planetary Science Letters, v. 388, p. 38–47, doi: 10.1016/j.epsl.2013.11.043.

Dolan, J.F., Mcauliffe, L.J., Rhodes, E.J., Mcgill, S.F., and Zinke, R.W., 2016, Extreme multi-millennial slip rate variations on the Garlock fault , California : Strain super-cycles , potentially time-variable fault strength , and implications for system-level earthquake occurrence: Earth and Planetary Science Letters, v. 446, p. 123–136, doi: 10.1016/j.epsl.2016.04.011.

Eaves, S.R., Anderson, B.M., and Mackintosh, A.N., 2017, Glacier-based climate reconstructions for the last glacial-interglacial transition: Arthur's Pass, New Zealand (43°S): Journal of Quaternary Science, v. 32, p. 877–887, doi: 10.1002/jqs.2904.

Elliott, A.J., Oskin, M.E., Liu-zeng, J., and Shao, Y.X., 2018, Persistent rupture terminations at a restraining bend from slip rates on the eastern Altyn Tagh fault: Tectonophysics, v. 733, p. 57–72, doi: 10.1016/j.tecto.2018.01.004.

Elliott, A.J., Oskin, M.E., Liu-Zeng, J., and Shao, Y., 2015, Rupture termination at restraining bends: The last great earthquake on the Altyn Tagh Fault: Geophysical Research Letters, v. 42, p. 2164–2170, doi: 10.1002/2015GL063107.

Freed, A.M., 2005, Earthquake triggering by static, dynamic, and postseismic stress transfer: Annual Review of Earth and Planetary Sciences, v. 33, p. 335–367, doi: 10.1146/annurev.earth.33.092203.122505.

Gauriau, J., and Dolan, J.F., 2021, Relative Structural Complexity of Plate-Boundary Fault Systems Controls Incremental Slip-Rate Behavior of Major Strike-Slip Faults: Geochemistry, Geophysics, Geosystems, v. 22, p. 1–24, doi: 10.1029/2021GC009938.

Gold, R.D., and Cowgill, E., 2011, Deriving fault-slip histories to test for secular variation in slip, with examples from the Kunlun and Awatere faults: Earth and Planetary Science Letters, v. 301, p. 52–64, doi: 10.1016/j.epsl.2010.10.011.

Hamling, I.J., Hreinsdóttir, S., Clark, K., Elliott, J., Liang, C., Fielding, E., Litchfield, N., Villamor, P., Wallace, L., Wright, T.J., D'Anastasio, E., Bannister, S., Burbidge, D., Denys, P., et al., 2017, Complex multifault rupture during the 2016 M w 7.8 Kaikōura earthquake, New Zealand: Science, v. 356, p. eaam7194, doi: 10.1126/science.aam7194.

Hardy, E.F., and Wellman, H.W., 1984, The Alpine, Wairau & Hope Faults: Victoria University of Wellington, Geology Department.

Harris, R.A., 1998, Forecasts of the 1989 Loma Prieta, California, earthquake: Bulletin of the Seismological Society of America, v. 88, p. 898–916.

Harris, R.A., and Simpson, R.W., 1998, Suppression of large earthquakes by stress shadows: A comparison of Coulomb and rate-and-state failure: Journal of Geophysical Research: Solid Earth, v. 103, p. 24439–24451.

Harris, R.A., Simpson, R.W., and Reasenberg, P.A., 1995, Influence of static stress changes on earthquake locations in southern California: Nature, v. 375, p. 221–224, doi: 10.1038/375221a0.

Hatem, A.E., Dolan, J.F., Zinke, R.W., Langridge, R.M., McGuire, C.P., Rhodes, E.J., Brown, N., and Van Dissen, R.J., 2020, Holocene to latest Pleistocene incremental slip rates from the east-central Hope Fault (Conway segment) at Hossack Station, Marlborough fault system, South Island, New Zealand: Towards a dated path of earthquake slip along a plate boundary fault: Geosphere, v. 16, p. 1–27, doi: 10.1130/ges02263.1.

Hogg, A.G., Heaton, T.J., Hua, Q., Palmer, J.G., Turney, C.S.M., Southon, J., Bayliss, A., Blackwell, P.G., Boswijk, G., Bronk Ramsey, C., Pearson, C., Petchey, F., Reimer, P., Reimer, R., et al., 2020, SHCal20 Southern Hemisphere Calibration, 0-55,000 Years cal BP: Radiocarbon, v. 62, p. 759–778, doi: 10.1017/RDC.2020.59.

Holden, C., Kaneko, Y., D'Anastasio, E., Benites, R., Fry, B., and Hamling, I.J., 2017, The 2016 Kaikōura Earthquake Revealed by Kinematic Source Inversion and Seismic Wavefield Simulations: Slow Rupture Propagation on a Geometrically Complex Crustal Fault Network: Geophysical Research Letters, v. 44, p. 11,320-11,328, doi: 10.1002/2017GL075301.

Holm, K., Bovis, M., and Jakob, M., 2004, The landslide response of alpine basins to post-Little Ice Age glacial thinning and retreat in southwestern British Columbia: Geomorphology, v. 57, p. 201–216, doi: 10.1016/S0169-555X(03)00103-X.

Hormes, A., Preusser, F., Denton, G., Hajdas, I., Weiss, D., Stocker, T.F., and Schlüchter, C., 2003, Radiocarbon and luminescence dating of overbank deposits in outwash sediments of the Last Glacial Maximum in North Westland, New Zealand: New Zealand Journal of Geology and Geophysics, v. 46, p. 95–106, doi: 10.1080/00288306.2003.9514998.

Howarth, J.D., Barth, N.C., Fitzsimons, S.J., Richards-Dinger, K., Clark, K.J., Biasi, G.P., Cochran, U.A., Langridge, R.M., Berryman, K.R., and Sutherland, R., 2021, Spatiotemporal clustering of great earthquakes on a transform fault controlled by geometry: Nature Geoscience, v. 14, p. 314–320, doi: 10.1038/s41561-021-00721-4.

Howarth, J.D., Cochran, U.A., Langridge, R.M., Clark, K., Fitzsimons, S.J., Berryman, K., Villamor, P., and Strong, D.T., 2018, Past large earthquakes on the Alpine Fault: paleoseismological progress and future directions: New Zealand Journal of Geology and Geophysics, v. 61, p. 309–328, doi: 10.1080/00288306.2018.1464658.

Hughes, A., Bell, R.E., Mildon, Z.K., Rood, D.H., Whittaker, A.C., Rockwell, T.K., Levy, Y., DeVecchio, D.E., Marshall, S.T., and Nicholson, C., 2020, Three-Dimensional Structure, Ground Rupture Hazards, and Static Stress Models for Complex Nonplanar Thrust Faults in the Ventura Basin, Southern California: Journal of Geophysical Research: Solid Earth, v. 125, doi: 10.1029/2020JB019539.

Kearse, J., Little, T.A., Van Dissen, R.J., Barnes, P.M., Langridge, R.M., Mountjoy, J., Ries, W., Villamor, P., Clark, K.J., Benson, A., Lamarche, G., Hill, M., and Hemphill-Haley, M., 2018, Onshore to Offshore Ground-Surface and Seabed Rupture of the Jordan–Kekerengu–Needles Fault Network during the 2016 Mw 7.8 Kaikoura Earthquake, New Zealand: Bulletin of the Seismological Society of America, v. 108, p. 1573–1595, doi: 10.1785/0120170304.

Keefer, D., 1984, Landslides caused by earthquakes: Geological Society of America Bulletin, v. 95, p. 406–421, doi: 10.1130/0016-7606.

Khajavi, N., Langridge, R.M., Quigley, M.C., Smart, C., Rezanejad, A., and Martín-González, F., 2016, Late Holocene rupture behavior and earthquake chronology on the Hope Fault, New Zealand: Geological Society of America Bulletin, v. 128, p. 1736–1761, doi: 10.1130/B31199.1.

Khajavi, N., Nicol, A., Quigley, M.C., and Langridge, R.M., 2018, Temporal slip-rate stability and variations on the Hope Fault, New Zealand, during the late Quaternary: Tectonophysics, v. 738–739, p. 112–123, doi: 10.1016/j.tecto.2018.05.001.

Khajavi, N., Quigley, M.C., and Langridge, R.M., 2014, Influence of topography and basement depth on surface rupture morphology revealed from LiDAR and field mapping, Hope Fault, New Zealand: Tectonophysics, v. 630, p. 265–284, doi: 10.1016/j.tecto.2014.05.032.

Khajavi, N., Quigley, M.C., and Langridge, R.M., 2014, Influence of topography and basement depth on surface rupture morphology revealed from LiDAR and field mapping, Hope Fault, New Zealand: Tectonophysics, v. 630, p. 265–284, doi: 10.1016/j.tecto.2014.05.032.

King, G.C.P., Stein, R.S., and Jian Lin, 1994, Static stress changes and the triggering of earthquakes: Bulletin - Seismological Society of America, v. 84, p. 935–953, doi: 10.1016/0148-9062(95)94484-2.

Langridge, R.M., Basili, R., Basher, L., and Wells, A.P., 2012, Late Holocene landscape change history related to the Alpine Fault determined from drowned forests in Lake Poerua, Westland, New Zealand: Natural Hazards and Earth System Science, v. 12, p. 2051–2064, doi: 10.5194/nhess-12-2051-2012.

Langridge, R.M., Campbell, J.K., Hill, N., Pere, V., Pope, J., Pettinga, J.R., Estrada, B., and Berryman, K., 2003, Paleoseismology and slip rate of the Conway Segment of the Hope Fault at Greenburn Stream, South Island, New Zealand: Annals of Geophysics, v. 46, p. 1119–1140, doi: 10.4401/ag-3449.

Langridge, R.M., Ries, W.F., Dolan, J.F., Schermer, E.R., and Siddoway, C., 2017, Slip rate estimates and slip gradient for the Alpine Fault at Calf Paddock, Maruia River, New Zealand: New Zealand Journal of Geology and Geophysics, v. 60, p. 73–88, doi: 10.1080/00288306.2016.1275707.

Langridge, R.M., Ries, W.F., Farrier, T., Barth, N.C., Khajavi, N., and De Pascale, G.P., 2014, Developing sub 5-m LiDAR DEMs for forested sections of the Alpine and Hope Faults, South Island, New Zealand: Implications for structural interpretations: Journal of Structural Geology, v. 64, p. 53–66, doi: 10.1016/j.jsg.2013.11.007.

Langridge, R.M., Ries, W., Litchfield, N., Villamor, P., Van Dissen, R.J., Barrell, D., Rattenbury, M., Heron, D., Haubrock, S., Townsend, D., Lee, J., Berryman, K., Nicol, A., Cox, S., et al., 2016, The New Zealand Active Faults Database: New Zealand Journal of Geology and Geophysics, v. 59, p. 86–96, doi: 10.1080/00288306.2015.1112818.

Langridge, R.M., Villamor, P., Basili, R., Almond, P., Martinez-Diaz, J.J., and Canora, C., 2010, Revised slip rates for the Alpine Fault at Inchbonnie: Implications for plate boundary kinematics of South Island, New Zealand: Lithosphere, v. 2, p. 139–152, doi: 10.1130/L88.1.

Langridge, R.M., Villamor, P., Howarth, J.D., Ries, W.F., Clark, K.J., and Litchfield, N.J., 2020, Reconciling an Early Nineteenth-Century Rupture of the Alpine Fault at a Section End, Toaroha River, Westland, New Zealand: Bulletin of the Seismological Society of America, doi: 10.1785/0120200116.

Lin, J., and Stein, R.S., 2004, Stress triggering in thrust and subduction earthquakes and stress interaction between the southern San Andreas and nearby thrust and strike-slip faults: Journal of Geophysical Research: Solid Earth, v. 109, p. 1–19, doi: 10.1029/2003jb002607.

Litchfield, N.J., Van Dissen, R.J., Sutherland, R., Barnes, P.M., Cox, S.C., Norris, R., Beavan, R.J., Langridge, R.M., Villamor, P., Berryman, K., Stirling, M., Nicol, A., Nodder, S., Lamarche, G., et al., 2014, A model of active faulting in New Zealand: New Zealand Journal of Geology and Geophysics, v. 57, p. 32–56, doi: 10.1080/00288306.2013.854256.

Litchfield, N.J., Villamor, P., van Dissen, R.J., Nicol, A., Barnes, P.M., Barrell, D.J.A., Pettinga, J.R., Langridge, R.M., Little, T.A., Mountjoy, J.J., Ries, W.F., Rowland, J., Fenton, C., Stirling, M.W., et al., 2018, Surface rupture of multiple crustal faults in the 2016 Mw 7.8 Kaikōura, New Zealand, earthquake: Bulletin of the Seismological Society of America, v. 108, p. 1496–1520, doi: 10.1785/0120170300.

Lozos, J.C., 2021, The effect of along-strike variation in dip on rupture propagation on strike-slip faults: v. 17, p. 1–15, doi: 10.1130/GES02391.1/5455696/ges02391.pdf.

Mackenzie, D., and Elliott, A.J., 2017, Untangling tectonic slip from the potentially misleading effects of landform geometry: Geosphere, v. 13, p. 1310–1328, doi: 10.1130/GES01386.1.

McKay, A., 1890, On the Earthquakes of September 1888 in the Amuri and Marlborough Districts of the South Island: New Zealand: Geological Survey Report of Geological Explorations, v. 20, p. 1–16.

Mildon, Z.K., Roberts, G.P., Faure Walker, J.P., and Toda, S., 2019, Coulomb pre-stress and fault bends are ignored yet vital factors for earthquake triggering and hazard: Nature Communications, v. 10, p. 1–9, doi: 10.1038/s41467-019-10520-6.

Mildon, Z.K., Roberts, G.P., Faure Walker, J.P., and Iezzi, F., 2017, Coulomb stress transfer and fault interaction over millennia on non-planar active normal faults: TheMw 6.5-5.0 seismic sequence of 2016-2017, central Italy: Geophysical Journal International, v. 210, p. 1206–1218, doi: 10.1093/gji/ggx213.

Mildon, Z.K., Toda, S., Faure Walker, J.P., and Roberts, G.P., 2016, Evaluating models of Coulomb stress transfer: Is variable fault geometry important? Geophysical Research Letters, v. 43, p. 12,407-12,414, doi: 10.1002/2016GL071128.

Mohammadi, H., Quigley, M.C., Steacy, S., and Duffy, B., 2019, Effects of source model variations on Coulomb stress analyses of a multi-fault intraplate earthquake sequence: Tectonophysics, v. 766, p. 151–166, doi: 10.1016/j.tecto.2019.06.007.

Moss, R.E.S., and Ross, Z.E., 2011, Probabilistic fault displacement hazard analysis for reverse faults: Bulletin of the Seismological Society of America, v. 101, p. 1542–1553, doi: 10.1785/0120100248.

Murray, A.S., Thomsen, K.J., Masuda, N., Buylaert, J.P., and Jain, M., 2012, Identifying well-bleached quartz using the different bleaching rates of quartz and feldspar luminescence signals: Radiation Measurements, v. 47, p. 688–695, doi: 10.1016/j.radmeas.2012.05.006.

Nicol, A., and Van Dissen, R.J., 2002, Up-dip partitioning of displacement components on the oblique-slip Clarence Fault, New Zealand: Journal of Structural Geology, v. 24, p. 1521–1535, doi: 10.1016/S0191-8141(01)00141-9.

Nicol, A., Walsh, J., Berryman, K., and Villamor, P., 2006, Interdependence of fault displacement rates and paleoearthquakes in an active rift: Geology, v. 34, p. 865–868, doi: 10.1130/G22335.1.

Ninis, D., Little, T.A., Van Dissen, R.J., Litchfield, N.J., Smith, E.G.C., Wang, N., Rieser, U., and Henderson, C.M., 2013, Slip rate on the wellington fault, New Zealand, during the late quaternary: Evidence for variable slip during the Holocene: Bulletin of the Seismological Society of America, v. 103, p. 559–579, doi: 10.1785/0120120162.

Parsons, T., Field, E.H., Page, M.T., and Milner, K., 2012, Possible Earthquake Rupture Connections on Mapped California Faults Ranked by Calculated Coulomb Linking Stresses: Bulletin of the Seismological Society of America, v. 102, p. 2667–2676, doi: 10.1785/0120110349.

Preusser, F., Ramseyer, K., and Schlüchter, C., 2006, Characterisation of low OSL intensity quartz from the New Zealand Alps: Radiation Measurements, v. 41, p. 871–877, doi: 10.1016/j.radmeas.2006.04.019.

Quigley, M., Van Dissen, R.J., Litchfield, N., Villamor, P., Duffy, B., Barrell, D., Furlong, K., Stahl, T., Bilderback, E., and Noble, D., 2012, Surface rupture during the 2010 Mw 7.1 darfield(canterbury) earthquake: Implications for fault rupture dynamics and seismic-hazard analysis: Geology, v. 40, p. 55–58, doi: 10.1130/G32528.1.

Quigley, M.C., Hughes, M.W., Bradley, B.A., van Ballegooy, S., Reid, C., Morgenroth, J., Horton, T., Duffy, B., and Pettinga, J.R., 2016, The 2010-2011 Canterbury Earthquake Sequence: Environmental effects, seismic triggering thresholds and geologic legacy: Tectonophysics, v. 672–673, p. 228–274, doi: 10.1016/j.tecto.2016.01.044.

Quigley, M.C., Jiménez, A., Duffy, B., and King, T.R., 2019, Physical and Statistical Behavior of Multifault Earthquakes: Darfield Earthquake Case Study, New Zealand: Journal of Geophysical Research: Solid Earth, v. 124, p. 4788–4810, doi: 10.1029/2019JB017508.

Ramsey, C.B., 2009, Bayesian analysis of radiocarbon dates: Radiocarbon, v. 51, p. 337–360, doi: 10.1017/s0033822200033865.

Reasenberg, P.A., and Simpson, R.W., 1997, Response of regional seismicity to the static stress change produced by the Loma Prieta earthquake: US Geological Survey Professional Paper,.

Rockwell, T.K., Lindvall, S., Herzberg, M., Murbach, D., Dawson, T., and Berger, G., 2000, Paleoseismology of the Johnson Valley, Kickapoo, and Homestead Valley faults: Clustering of earthquakes in the Eastern California shear zone: Bulletin of the Seismological Society of America, v. 90, p. 1200–1236, doi: 10.1785/0119990023.

Rodgers, D.W., and Little, T.A., 2006, World’s largest coseismic strike-slip offset: The 1855 rupture of the Wairarapa Fault, New Zealand, and implications for displacement/length scaling of continental earthquakes: Journal of Geophysical Research: Solid Earth, v. 111, p. 1–19, doi: 10.1029/2005JB004065.

Ross, Z.E., Idini, B., Jia, Z., Stephenson, O.L., Zhong, M., Wang, X., Zhan, Z., Simons, M., Fielding, E.J., Yun, S., Hauksson, E., and Moore, A.W., 2019, Hierarchical interlocked orthogonal faulting in the 2019 Ridgecrest earthquake sequence: Science, v. 3665, p. 346–351.

Rosser, B.J., and Carey, J.M., 2017, Comparison of landslide inventories from the 1994 Mw 6.8 Arthurs Pass and 2015 Mw 6.0 Wilberforce earthquakes, Canterbury, New Zealand: Landslides, v. 14, p. 1171–1180, doi: 10.1007/s10346-017-0797-8.

Rother, H., 2006, Late Pleistocene Glacial Geology of the Hope-Waiau Valley System in North Canterbury, New Zealand: University of Canterbury, 1–74 p.

Rother, H., Shulmeister, J., Fink, D., Alexander, D., and Bell, D., 2015, Surface exposure chronology of the Waimakariri glacial sequence in the Southern Alps of New Zealand: Implications for MIS-2 ice extent and LGM glacial mass balance: Earth and Planetary Science Letters, v. 429, p. 69–81, doi: 10.1016/j.epsl.2015.07.033.

Rother, H., Shulmeister, J., and Rieser, U., 2010, Stratigraphy, optical dating chronology (IRSL) and depositional model of pre-LGM glacial deposits in the Hope Valley, New Zealand: Quaternary Science Reviews, v. 29, p. 576–592, doi: 10.1016/j.quascirev.2009.11.001.

Rowan, A. V., Roberts, H.M., Jones, M.A., Duller, G.A.T., Covey-Crump, S.J., and Brocklehurst, S.H., 2012, Optically stimulated luminescence dating of glaciofluvial sediments on the Canterbury Plains, South Island, New Zealand: Quaternary Geochronology, v. 8, p. 10–22, doi: 10.1016/j.quageo.2011.11.013.

Sarkar, I., and Chander, R., 2003, Role of static stress transfer in earthquake occurrence in the Himalaya: Journal of Asian Earth Sciences, v. 22, p. 59–65, doi: 10.1016/S1367-9120(03)00036-1.

Shulmeister, J., Thackray, G.D., Rittenour, T.M., Fink, D., and Patton, N.R., 2019, The timing and nature of the last glacial cycle in New Zealand: Quaternary Science Reviews, v. 206, p. 1–20, doi: 10.1016/j.quascirev.2018.12.020.

Shulmeister, J., Thackray, G.D., Rittenour, T.M., and Hyatt, O.M., 2018, Multiple glacial advances in the Rangitata Valley, South Island, New Zealand, imply roles for Southern Hemisphere westerlies and summer insolation in MIS 3 glacial advances: Quaternary Research (United States), v. 89, p. 375–393, doi: 10.1017/qua.2017.108.

Sohbati, R., Borella, J., Murray, A., Quigley, M.C., and Buylaert, J.P., 2016, Optical dating of loessic hillslope sediments constrains timing of prehistoric rockfalls, Christchurch, New Zealand: Journal of Quaternary Science, v. 31, p. 678–690, doi: 10.1002/jqs.2895.

Stahl, T., Quigley, M.C., and Bebbington, M.S., 2016, Tectonic geomorphology of the Fox Peak and Forest Creek Faults, South Canterbury, New Zealand: slip rates, segmentation and earthquake magnitudes: New Zealand Journal of Geology and Geophysics, v. 59, p. 568–591, doi: 10.1080/00288306.2016.1212908.

Steacy, S., Nalbant, S.S., McCloskey, J., Nostro, C., Scotti, O., and Baumont, D., 2005, Onto what planes should Coulomb stress perturbations be resolved? Journal of Geophysical Research: Solid Earth, v. 110, p. 1–14, doi: 10.1029/2004JB003356.

Stein, R.S., 1999, The role of stress transfer in earthquake occurrence: Nature, v. 402, p. 605–609, doi: 10.1038/45144.

Stein, R.S., Barka, A.A., and Dieterich, J.H., 1997, Progressive failure on the North Anatolian fault since 1939 by earthquake stress triggering: Geophysical Journal International, v. 128, p. 594–604, doi: 10.1111/j.1365-246X.1997.tb05321.x.

Stirling, M., McVerry, G., Gerstenberger, M., Litchfield, N., Van Dissen, R., Berryman, K., Barnes, P., Wallace, L., Villamor, P., Langridge, R.M., Lamarche, G., Nodder, S., Reyners, M., Bradley, B., et al., 2012, National Seismic Hazard Model for New Zealand: 2010 Update: Bulletin of the Seismological Society of America, v. 102, p. 1514–1542, doi: 10.1785/0120110170.

Suggate, R.P., and Almond, P.C., 2005, The Last Glacial Maximum (LGM) in western South Island, New Zealand: Implications for the global LGM and MIS 2: Quaternary Science Reviews, v. 24, p. 1923–1940, doi: 10.1016/j.quascirev.2004.11.007.

Toda, S., Stein, R.S., Richards-Dinger, K., and Bozkurt, S.B., 2005, Forecasting the evolution of seismicity in southern California: Animations built on earthquake stress transfer: Journal of Geophysical Research: Solid Earth, v. 110, p. 1–17, doi: 10.1029/2004JB003415.

Toda, S., Stein, R.S., Reasenberg, P. a, Dieterich, J.H., and Yoshida, A., 1998, Stress transferred by the 1995 M w = 6.9 Kobe, Japan, shock: Effect on aftershocks and future earthquake probabilities: Journal of Geophysical Research: Solid Earth, v. 103, p. 24543–24565, doi: 10.1029/98JB00765.

Vermeer, J.L., Quigley, M.C., Duffy, B.G., Langridge, R.M., and Pettinga, J.R., 2021, Structure and kinematics of active faulting in the Hope-Kelly and Alpine Fault intersection zone, South Island, New Zealand: Tectonophysics, v. 813, p. 228928, doi: 10.1016/j.tecto.2021.228928.

Walters, R.J., Gregory, L.C., Wedmore, L.N.J., Craig, T.J., McCaffrey, K., Wilkinson, M., Chen, J., Li, Z., Elliott, J.R., Goodall, H., Iezzi, F., Livio, F., Michetti, A.M., Roberts, G., et al., 2018, Dual control of fault intersections on stop-start rupture in the 2016 Central Italy seismic sequence: Earth and Planetary Science Letters, v. 500, p. 1–14, doi: 10.1016/j.epsl.2018.07.043.

Wells, A., Yetton, M.D., Duncan, R.P., and Stewart, G.H., 1999, Prehistoric dates of the most recent Alpine Fault earthquakes, New Zealand: Geology, v. 27, p. 995–998, doi: 10.1130/0091-7613(1999)027<0995:PDOTMR>2.3.CO;2.

Wesnousky, S.G., 2006, Predicting the endpoints of earthquake ruptures: Nature, v. 444, p. 358–360, doi: 10.1038/nature05275.

Yetton, M.D., 1998, Progress in understanding the paleoseismicity of the central and northern Alpine Fault, Westland, New Zealand: New Zealand Journal of Geology and Geophysics, v. 41, p. 475–483, doi: 10.1080/00288306.1998.9514824.

Zechar, J.D., and Frankel, K.L., 2009, Incorporating and reporting uncertainties in fault slip rates: Journal of Geophysical Research: Solid Earth, v. 114, p. 1–9, doi: 10.1029/2009JB006325.

Zhan, Z., Jin, B., Wei, S., and Graves, R.W., 2011, Coulomb stress change sensitivity due to variability in mainshock source models and receiving fault parameters: A case study of the 2010-2011 Christchurch, New Zealand, earthquakes: Seismological Research Letters, v. 82, p. 800–814, doi: 10.1785/gssrl.82.6.800.

Zhan, Z., Wei, S., Ni, S., and Helmberger, D., 2011, Earthquake centroid locations using calibration from ambient seismic noise: Bulletin of the Seismological Society of America, v. 101, p. 1438–1445, doi: 10.1785/0120100118.

Zielke, O., 2018, Earthquake Recurrence and the Resolution Potential of Tectono-Geomorphic Records: Bulletin of the Seismological Society of America, v. 108, p. 1399–1413, doi: 10.1785/0120170241.

Zielke, O., Klinger, Y., and Arrowsmith, J.R., 2015, Fault slip and earthquake recurrence along strike-slip faults - Contributions of high-resolution geomorphic data: Tectonophysics, v. 638, p. 43–62, doi: 10.1016/j.tecto.2014.11.004.

Zinke, R.W., Dolan, J.F., Rhodes, E.J., Van Dissen, R.J., Hatem, A.E., McGuire, C.P., Brown, N.D., and Grenader, J.R., 2021, Latest Pleistocene–Holocene Incremental Slip Rates of the Wairau Fault: Implications for Long-Distance and Long-Term Coordination of Faulting Between North and South Island, New Zealand: Geochemistry, Geophysics, Geosystems, v. 22, p. 1–16, doi: 10.1029/2021GC009656.

Zinke, R.W., Dolan, J.F., Rhodes, E.J., Van Dissen, R.J., McGuire, C.P., Hatem, A.E., Brown, N.D., and Langridge, R.M., 2019, Multimillennial Incremental Slip Rate Variability of the Clarence Fault at the Tophouse Road Site, Marlborough Fault System, New Zealand: Geophysical Research Letters, v. 46, p. 717–725, doi: 10.1029/2018GL080688.

Zinke, R.W., Dolan, J.F., Rhodes, E.J., Van Dissen, R., and McGuire, C.P., 2017, Highly Variable Latest Pleistocene-Holocene Incremental Slip Rates on the Awatere Fault at Saxton River, South Island, New Zealand, Revealed by Lidar Mapping and Luminescence Dating: Geophysical Research Letters, v. 44, p. 11,301-11,310, doi: 10.1002/2017GL075048.

Zinke, R., Hollingsworth, J., and Dolan, J.F., 2014, Surface slip and off-fault deformation patterns in the 2013 M W 7.7 Balochistan, Pakistan earthquake: Implications for controls on the distribution of near-surface coseismic slip: Geochemistry, Geophysics, Geosystems, v. 15, p. 5034–5050, doi: 10.1002/2014GC005538.

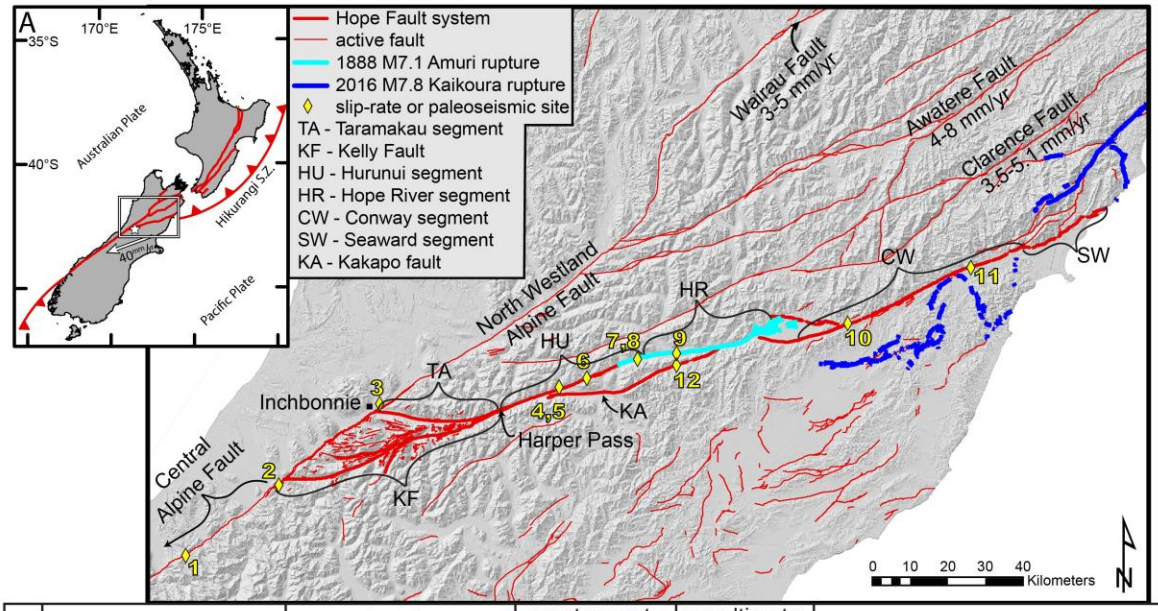

ID	site name	slip-rate SS: strike-slip DS: dip-slip	most recent surface rupture (C.E.)	penultimate surface rupture (C.E.)	references
1	Kakapotahi River	SS: 29 ±6 mm/yr DS: 6 ±1 mm/yr	—	—	Norris and Cooper, 2001
2	Staples	—	1813-1848	1717	Langridge et al., 2020
3	Inchbonnie	SS: 13.6 ±1.8 mm/yr DS: 3.4 ±0.6 mm/yr	—	—	Langridge et al., 2010
4	Matagouri Flat	SS: 13.3 ±3.2 mm/yr	1655-1835	1415-1625	Langridge et al., 2013; Khajavi et al., 2018
5	McKenzie Fan	SS: 14.9 ±3 mm/yr	—	—	Khajavi et al., 2018
6	Macs Knob	SS: 12 ±1.4 mm/yr	—	—	Khajavi et al., 2018
7	Hope River	SS: 9.3 ±2.7 mm/yr	—	—	Khajavi et al., 2018
8	Hope Shelter	—	1888	1740-1840	Khajavi et al., 2016
9	Horeshoe Lake	—	1888	—	Cowan and McGlone, 1991; Langridge et al., 2013
10	Hossack Station	SS: 8-32 mm/yr	—	—	Hatem et al., 2020
11	Green Burn	SS: 23 ±4 mm/yr	1730-1840	1657-1797	Hatem et al., 2019; Langridge et al., 2003
12	Kakapo Brook	SS: 6.4 ±0.4 mm/yr	—	—	Yang, 1991; Langridge and Berryman, 2005

Figure 1. A) Tectonic setting of New Zealand. The white arrow shows the Australian-Pacific relative plate motion at the Hope-Kelly-Alpine fault intersection. B) Active faults of the northern South Island, including the Alpine fault and Marlborough fault system, with generalized slip rates of the Clarence, Awatere and Wairau faults (Mason et al., 2006; Zachariasen et al., 2006; Van Dissen and Nicol, 2009). The Hope fault system is shown in bold red, with segments labelled in black and historic surface rupture extents highlighted in blue and light blue (1888 Amuri earthquake, 2016 Kaikoura earthquake, respectively). Yellow diamonds and numbers indicate slip-rate or paleoseismic study sites, and the numbers correlate to ID in the table which shows the

measured slip-rate and/or dates of most recent and penultimate surface rupture, with references (Cowan and McGlone, 1991; Yang, 1991; Norris and Cooper, 2001; Langridge and Berryman, 2005; Langridge et al., 2010; Langridge et al., 2013; Khajavi et al., 2016; Khajavi et al., 2018; Hatem et al., 2019; Hatem et al., 2020; Langridge et al., 2021).

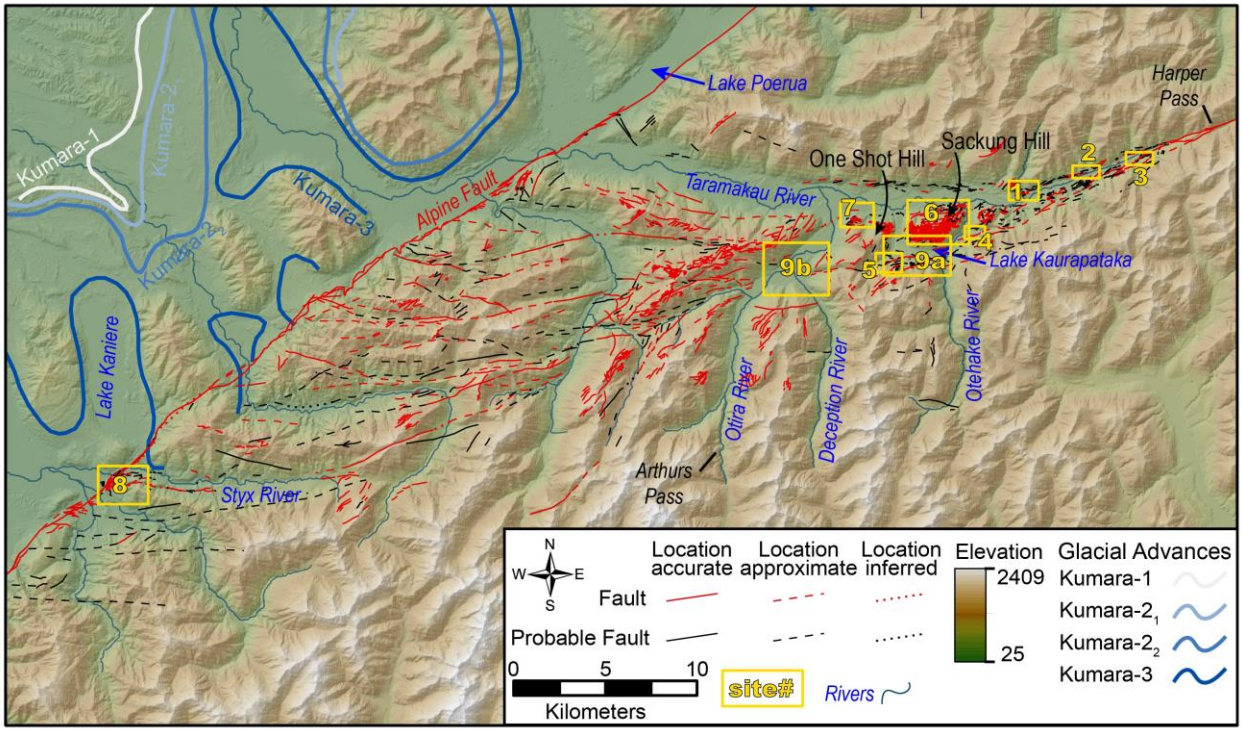

Figure 2. Map of the study area, showing topography and active faults from Harper Pass and Arthurs Pass to the coastal plain (Vermeer et al., 2021). The extent of sites in this study are shown with yellow boxes. Significant rivers are labelled in blue. The maximum extent of recent glaciations are shown in shades of blue/white and labelled (Barrows et al., 2013).

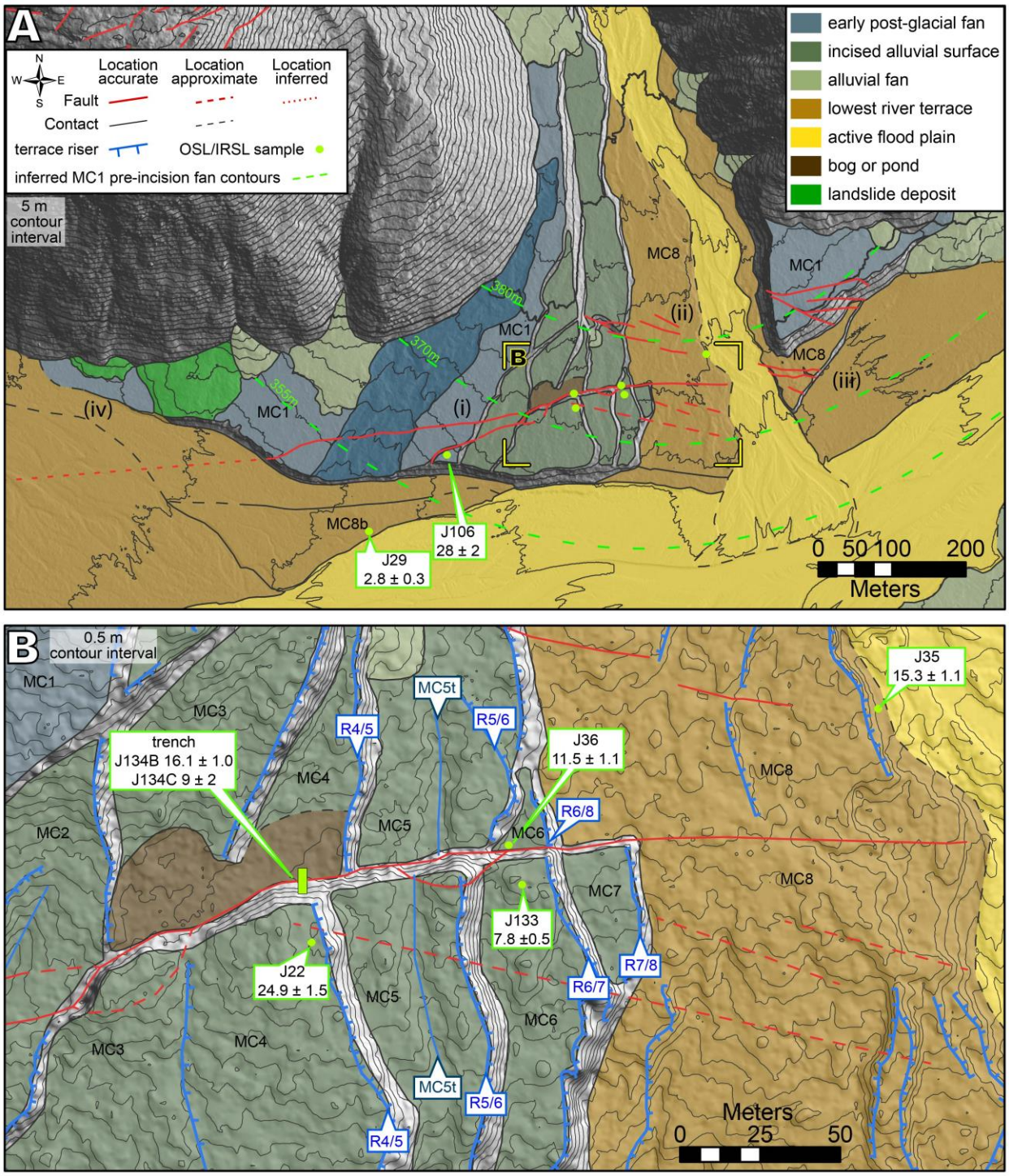

Figure 3. Geomorphic map of Site 1: Michael Creek with sample locations and luminescence or 14C ages. A) green lines show the inferred topographic contours of the earliest postglacial fan, of

which the MC1 surfaces are remnants. Contour interval is 5 m. B) Locations of OSL samples shown with green dots, trench is green rectangle. Surfaces are labelled (MCx), terrace risers (Rx/x), and the channel on MC5 (MC5t). Contour interval is 0.5 m.

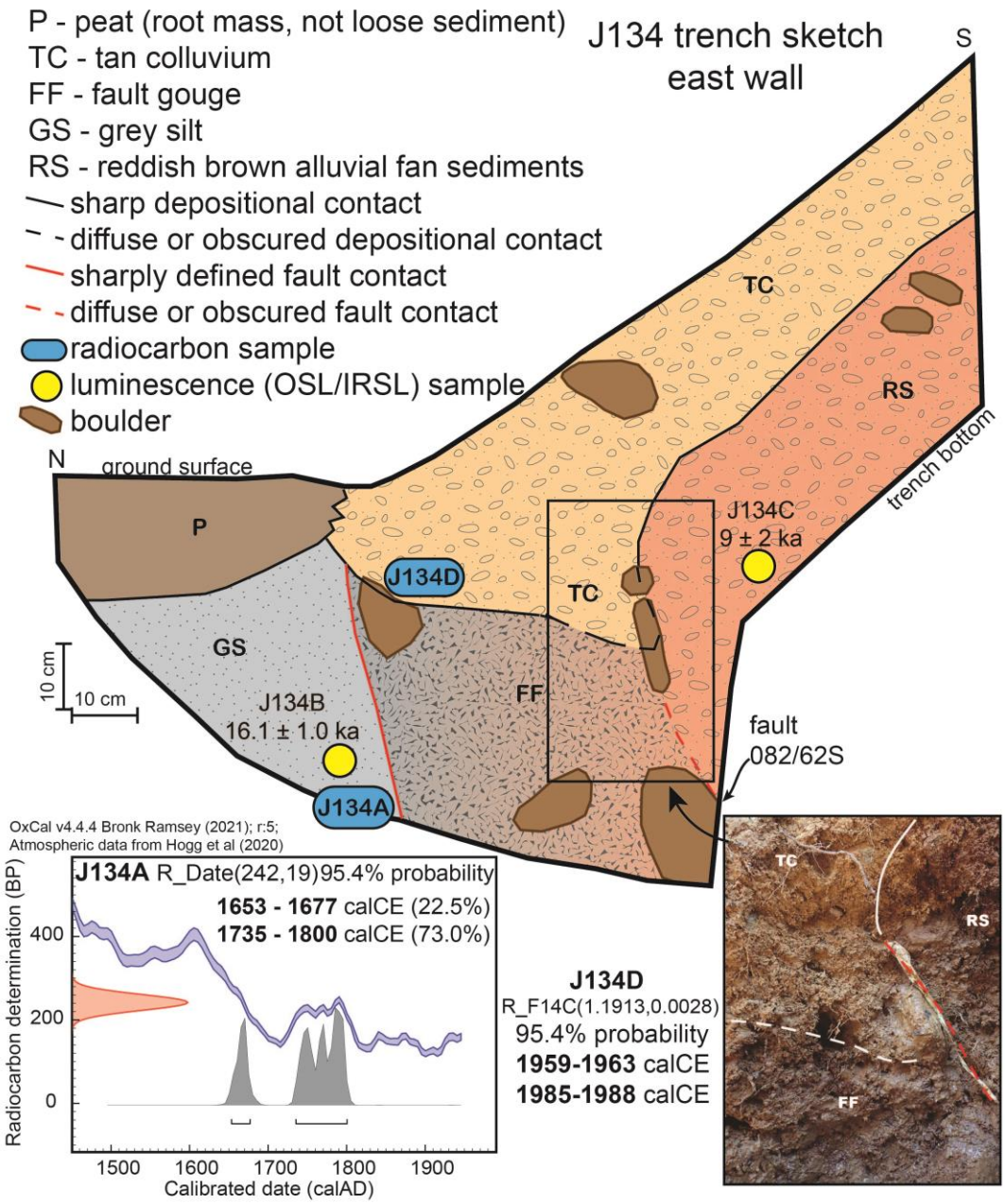

Figure 4. Log of the east side of the Michael Creek fan hand-dug trench. OSL samples are shown by yellow circles, radiocarbon samples are shown by blue ovals. The photo shows the complex

triple junction between RS, TC and the fault (FF) where TC has infilled post-rupture topographic irregularities. The south edge of the fault zone is oriented 082/62S. The 14C calibration curve and resulting calibrated age (1653-1800 CE) for sample J124A is also shown.

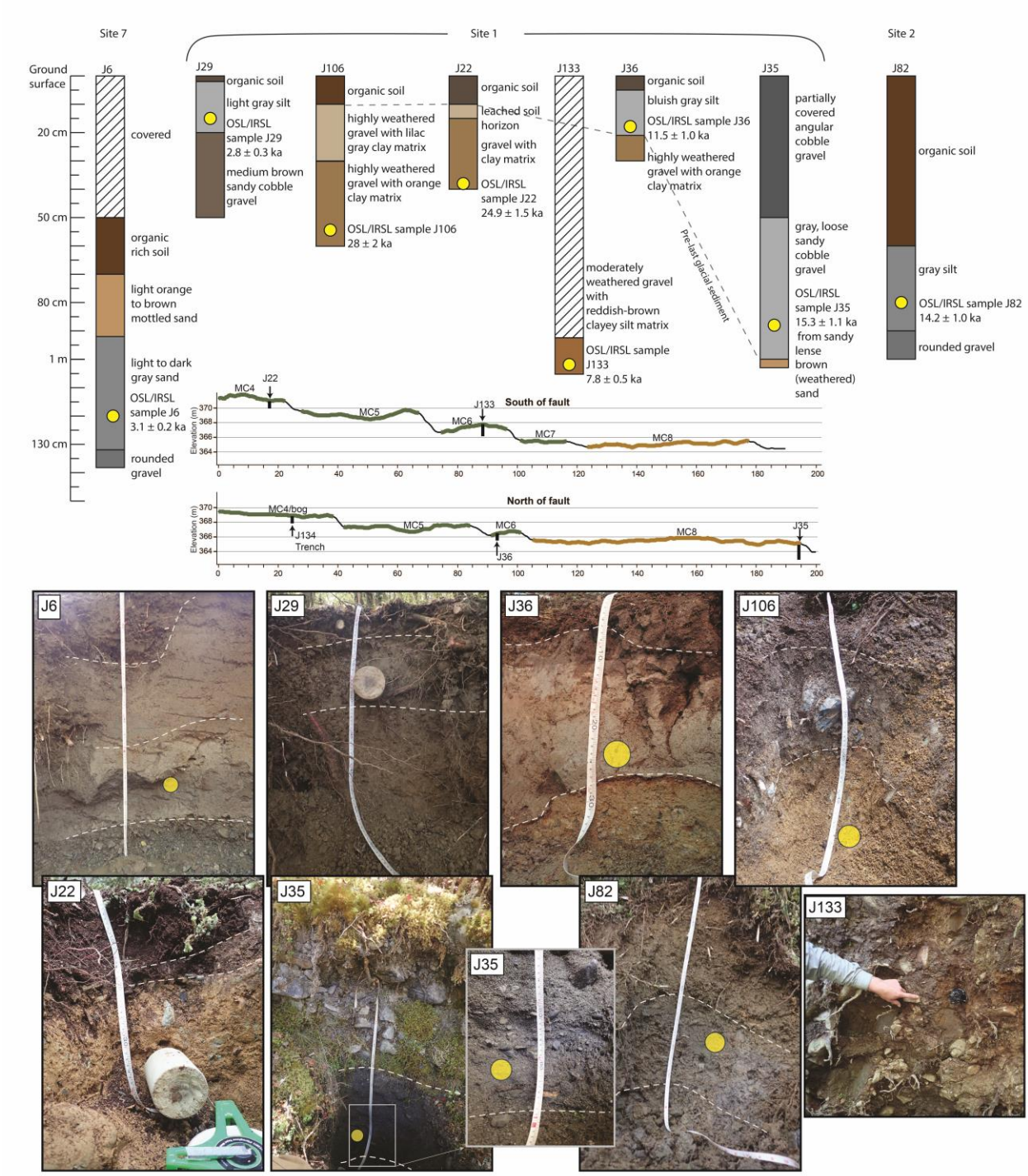

Figure 5. A) Luminescence sample pit and outcrop stratigraphic logs showing the stratigraphy of each sample site. The elevation and sample locations for Michael's Creek fan (Site 1, Section 3.2.1) are shown on vertically exaggerated fault parallel topographic profiles north and south of the fault. B) Photos of Luminescence sample sites.

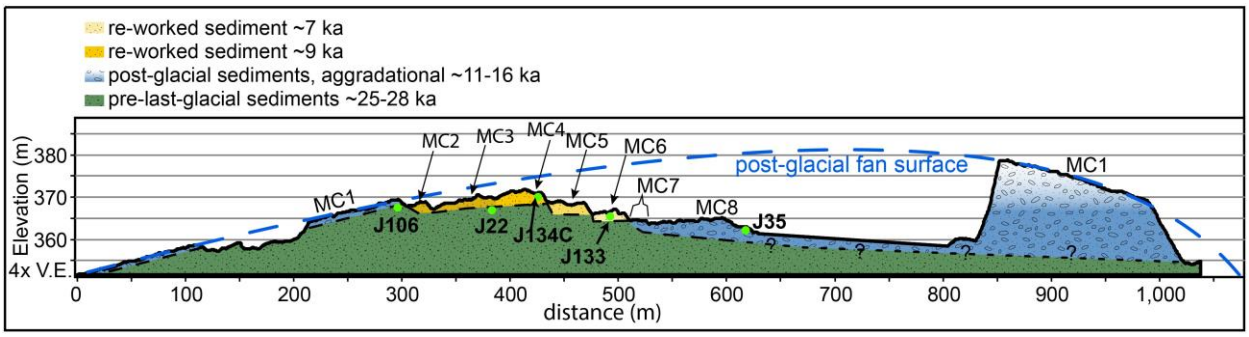

Figure 6. Sediment schematic of Michael Creek showing how the three generations of sediment (pre-last glacial, early post-last-glacial, and early Holocene) may be distributed.

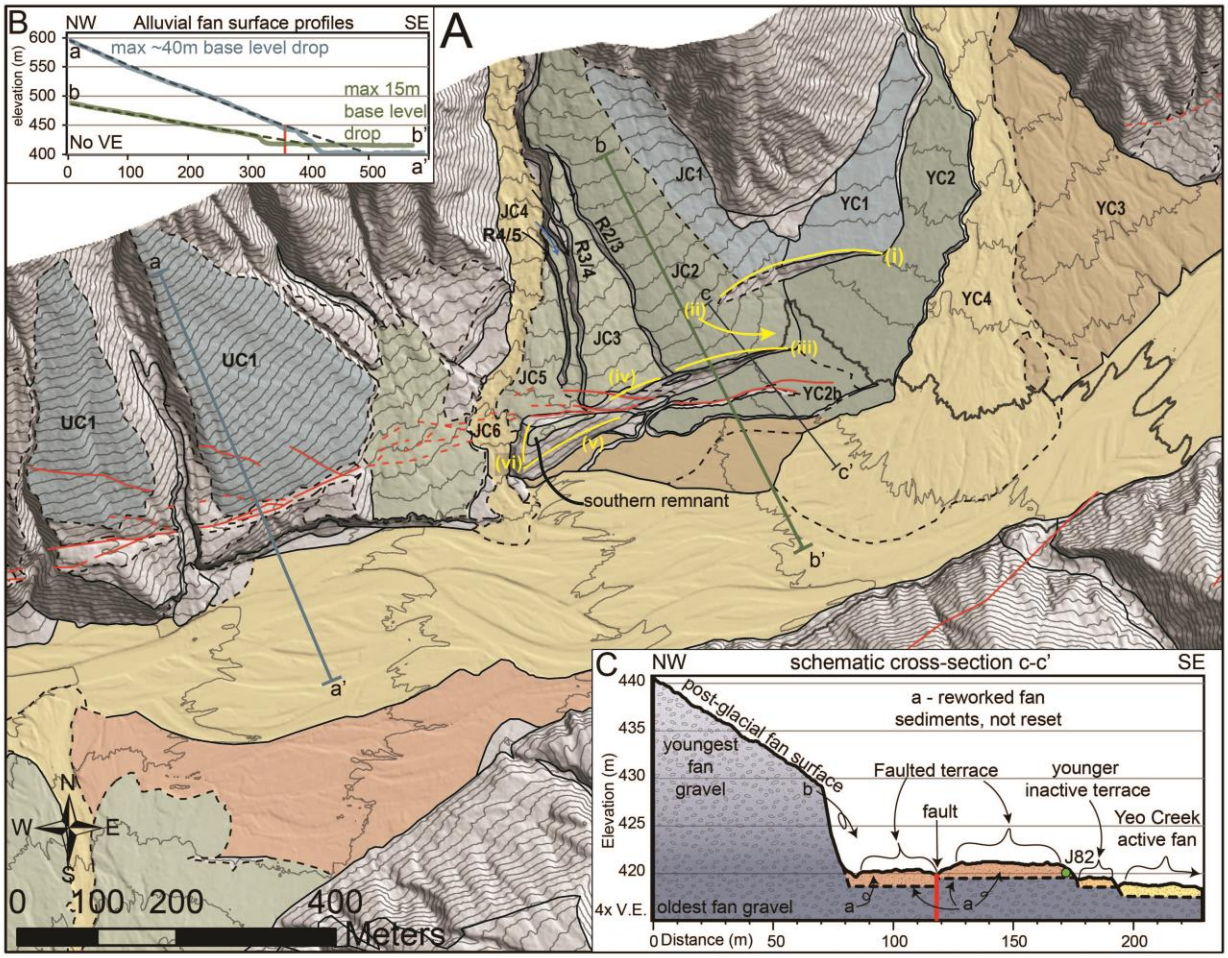

Figure 7. Geomorphology of Site 2: Yeo Creek. A) Geomorphic map with geomorphic feature labels (black), markers of interest (yellow), and cross-section locations. B) Topographic profiles of two major fan surfaces (solid line), location of the main trace of the Hope fault (red), and surface projection lines to the current local river level (dashed), maximum relative base level drop noted (maximum 40 m for a-a', maximum 15 m for b-b'). C) Schematic geologic cross-section (c-c') showing the early post-glacial fan sediments (blue), the re-worked but not reset sediments of the faulted TC2 terrace (orange) from which sample J82 was collected, and the younger and surfaces of Yeo Creek (yellow).

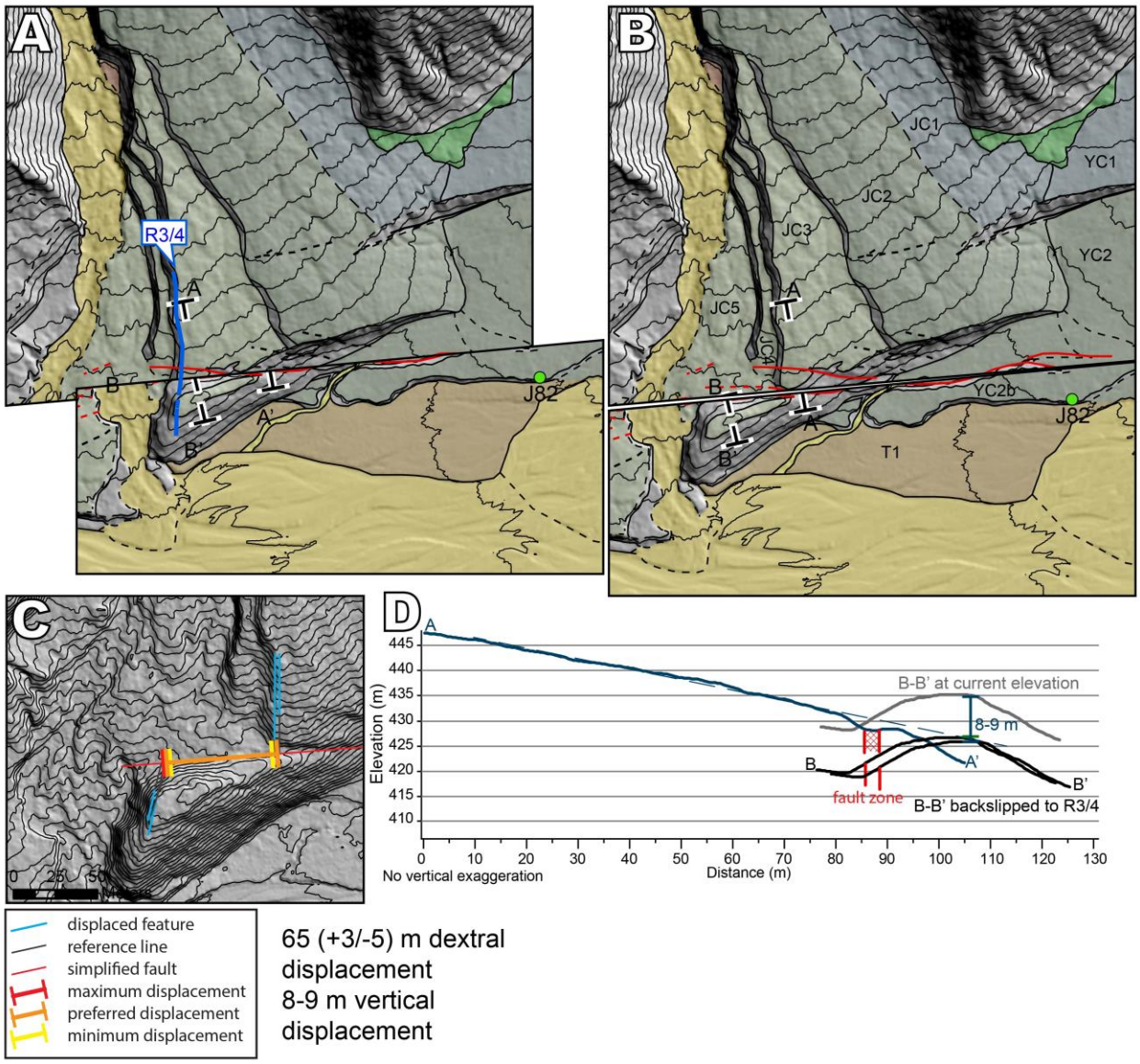

Figure 8. Displacement measurement in the Yeo-Jacobs creeks area (J82). A) Back-slip reconstruction of the measured displacement. B) Original site map, showing the profile end points and location of sample J82. C) Detailed view of the displacement measurement, with 1m contour interval. Minimum, maximum and preferred lateral displacements are shown. D) Topographic

profile reconstruction. Profile A-A' shows morphology of the JC2 fan surface, with the dashed line showing the projected fan surface (now eroded). Red zones show the fault zone, which has been aligned on A-A' and B-B' to estimate the pre-faulting position of B-B' relative to A-A'. The grey profile is B-B' showing the southern fan remnant at its present elevation. The black profiles show B-B' repositioned to match up with the projection of the JC3 surface, 8-9m lower than the present elevation.

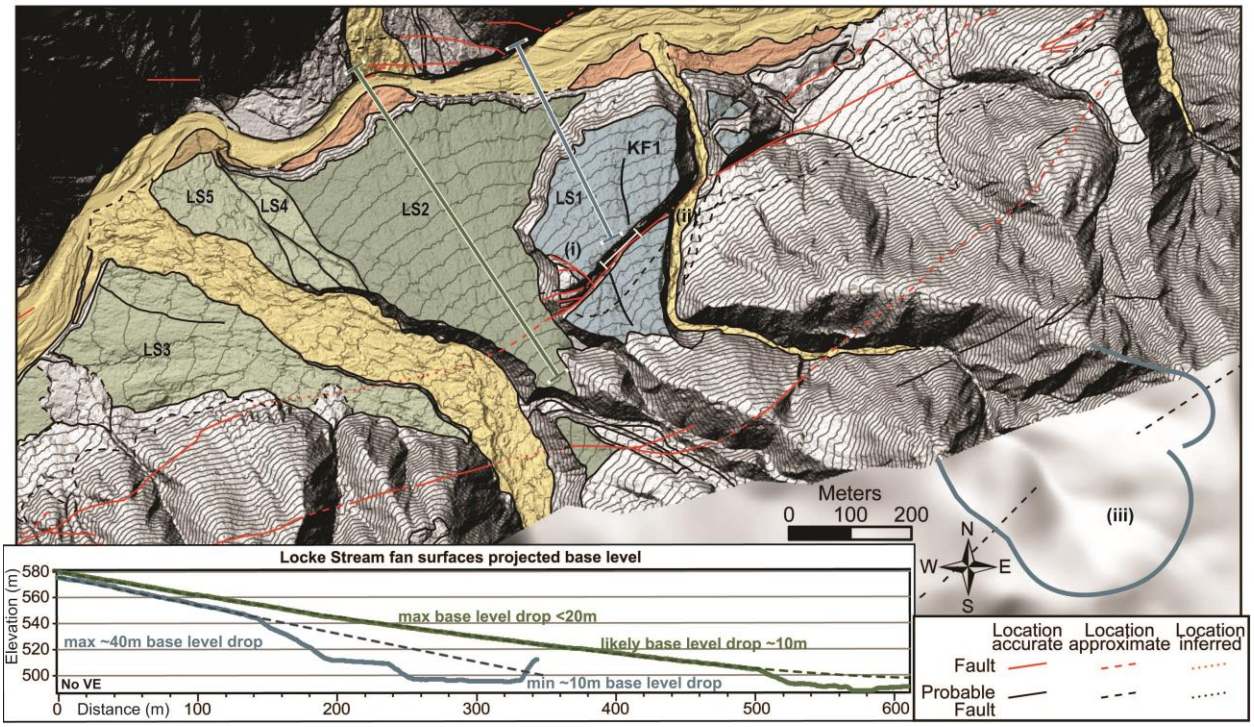

Figure 9. Geomorphic map of Site 3: Locke Stream area. Displacement measurement KF1 is shown in black on the LS1 surface. Source area for LS1 is shown by (iii). Part of the source area for the LS2 fan is shown with green, and also includes the Locke Stream watershed. Profiles show maximum relative base level drop interpolated from the preserved fan slopes and limited by the valley width.

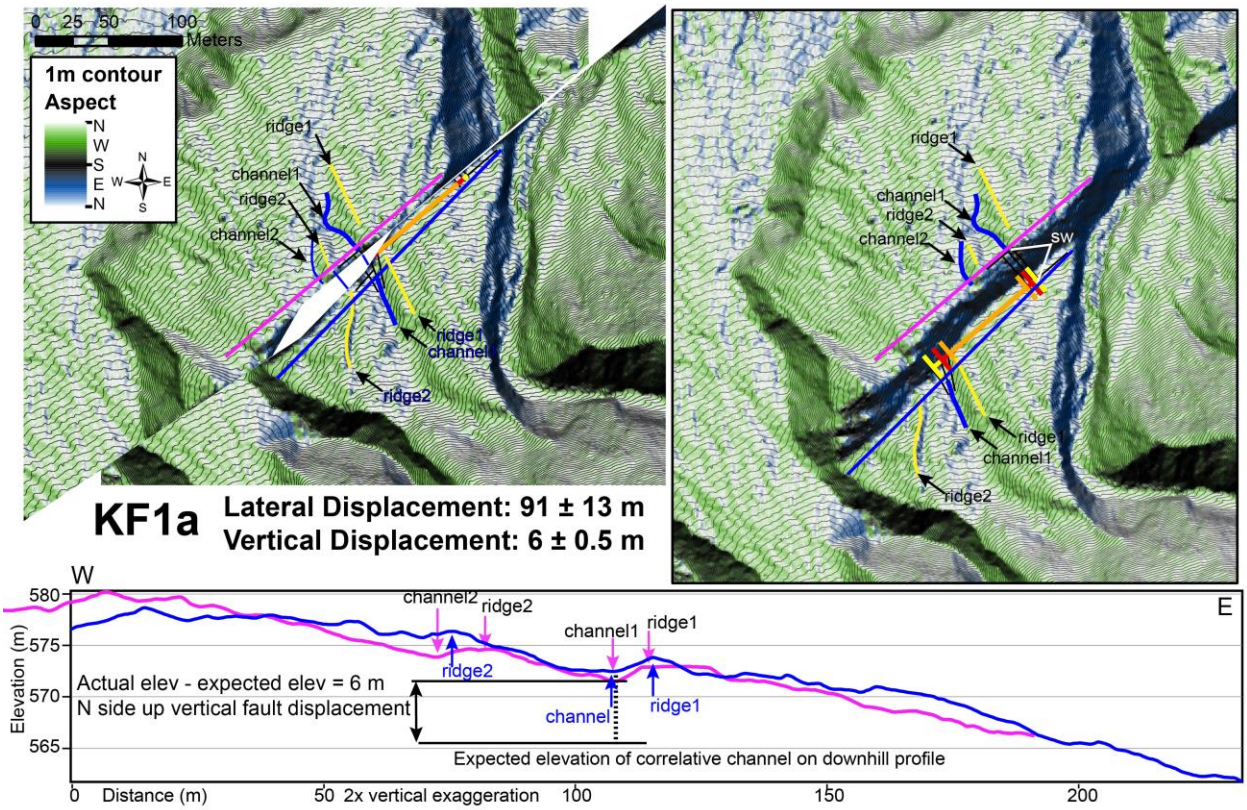

Figure 10. Displacement measurement details for the preferred reconstruction (KF1a) at Locke Stream. A) Back-slipped map showing correlation of features across the fault. B) Current site map with correlated features shown and minimum, preferred and maximum lateral displacement measurements. D) Fault parallel topographic profiles, visually shifted to measure vertical displacement across the fault.

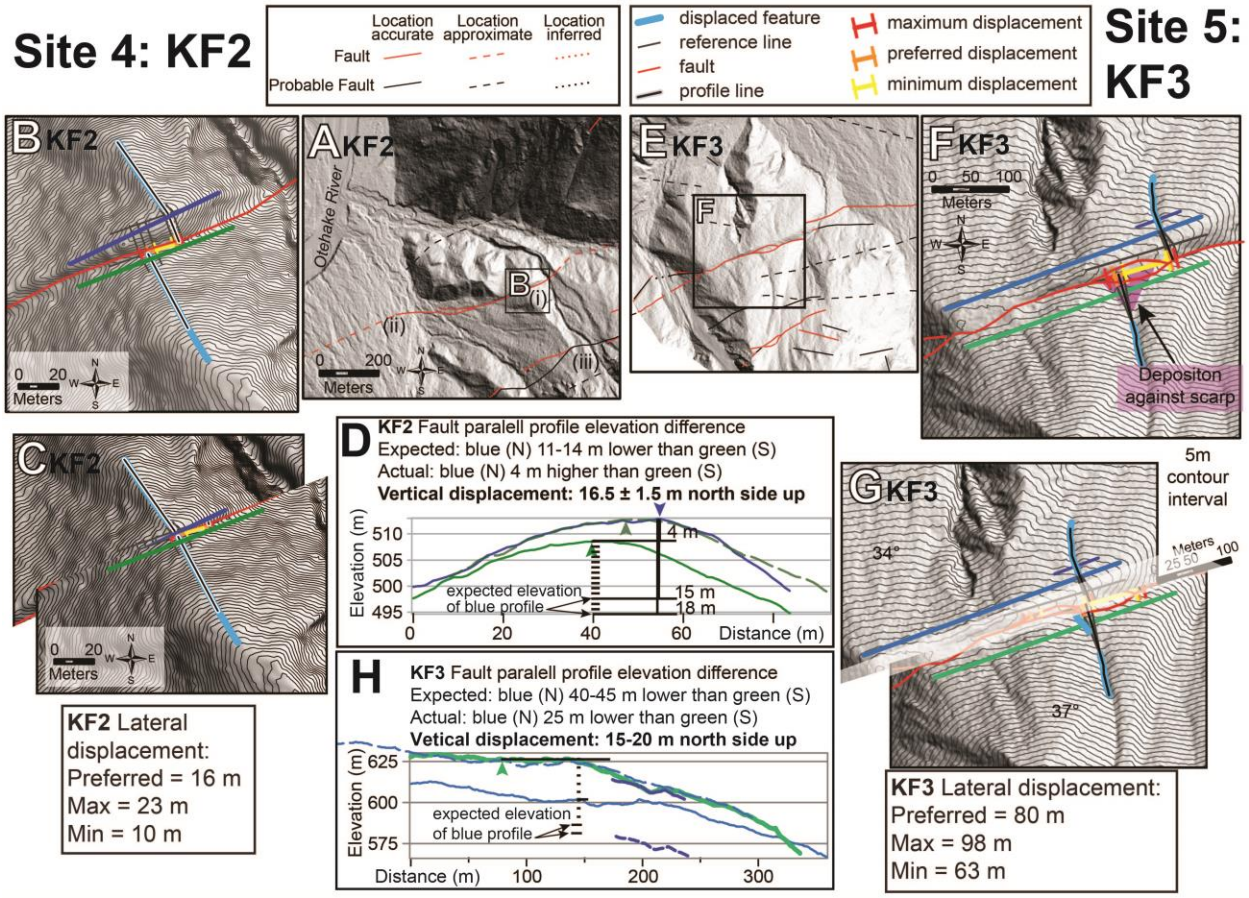

Figure 11. Map and displacement measurement for Site 4: KF2 (A-D) and Site 5: KF3 (E-H). A) hillshade and fault map of area surrounding KF2 displacement measurement. Roman numerals indicate locations mentioned in the text. B) Features and profiles at the KF2 displacement site. C) Cut and back-slipped map of the KF2 displacement. D) KF2 fault parallel topographic profiles, shifted to match. Vertical fault displacement calculated by differencing the observed and expected vertical offset of the profiles. Ridge slope and horizontal distance between the profiles was used to determine the expected vertical offset of the fault parallel profiles. E) Hillshade and mapped faults of area surrounding KF3 displacement measurement. F) Zoom of the displaced features at KF3. Lateral displacement correlation shown with minimum, preferred, and maximum measurements. Pre-faulting landscape slopes (37° and 34°) used to calculate the vertical

displacement in H. G) Cut and back-slipped map of the KF3 displaced features. H) Fault parallel profiles, original position and overlapping correlation (dashed). Short profile of the lateral displacement channel to show that the channel has similar shape as the channel south of the fault so it can be correlated across the fault.

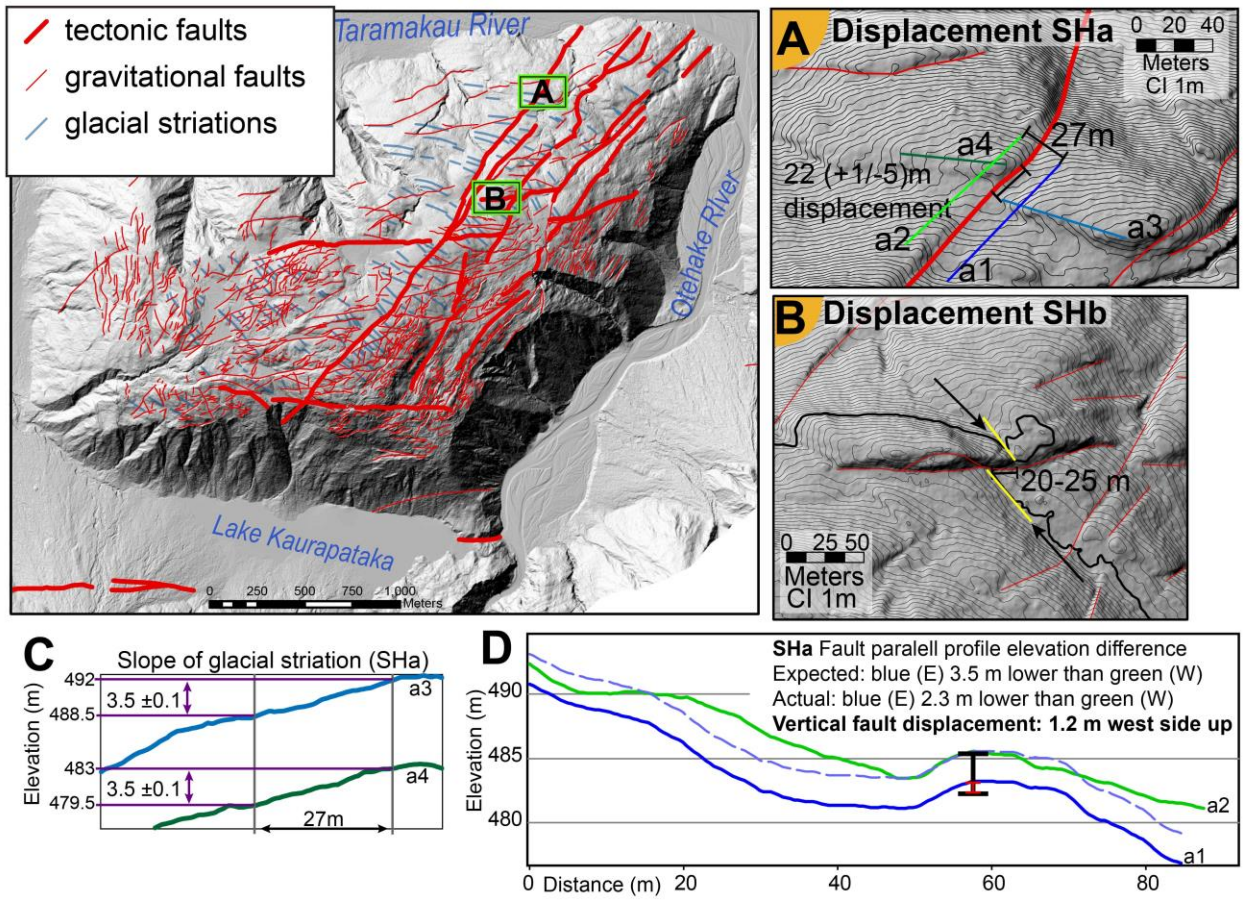

Figure 12. Map of Site 6: Sackung Hill, with faults from Vermeer et al., (2021), locations of displacement measurement maps are shown in green. A) Displacement SHa, with profile lines in C and D marked. Distance between fault-parallel profiles is 27 m and lateral displacement of glacial striation is 22 (+1/-5) m right-lateral. B) Displacement SHb yellow line shows the location of the slope change used to measure the offset of 20-25 m. The highlighted contour shows that the feature is nearly horizontal on the south side and is at the same elevation on the north side,

indicating no vertical displacement. C) Topographic profiles along glacial striation in A, showing the east and west sides have the same slope, and expected vertical difference 27 m along the feature is 3.5 m. D) Fault parallel topographic profiles, dashed profiles is shifted to show how features match. Vertical fault displacement is 1.2 m west side up, the difference between expected and actual elevation difference between the two profiles.

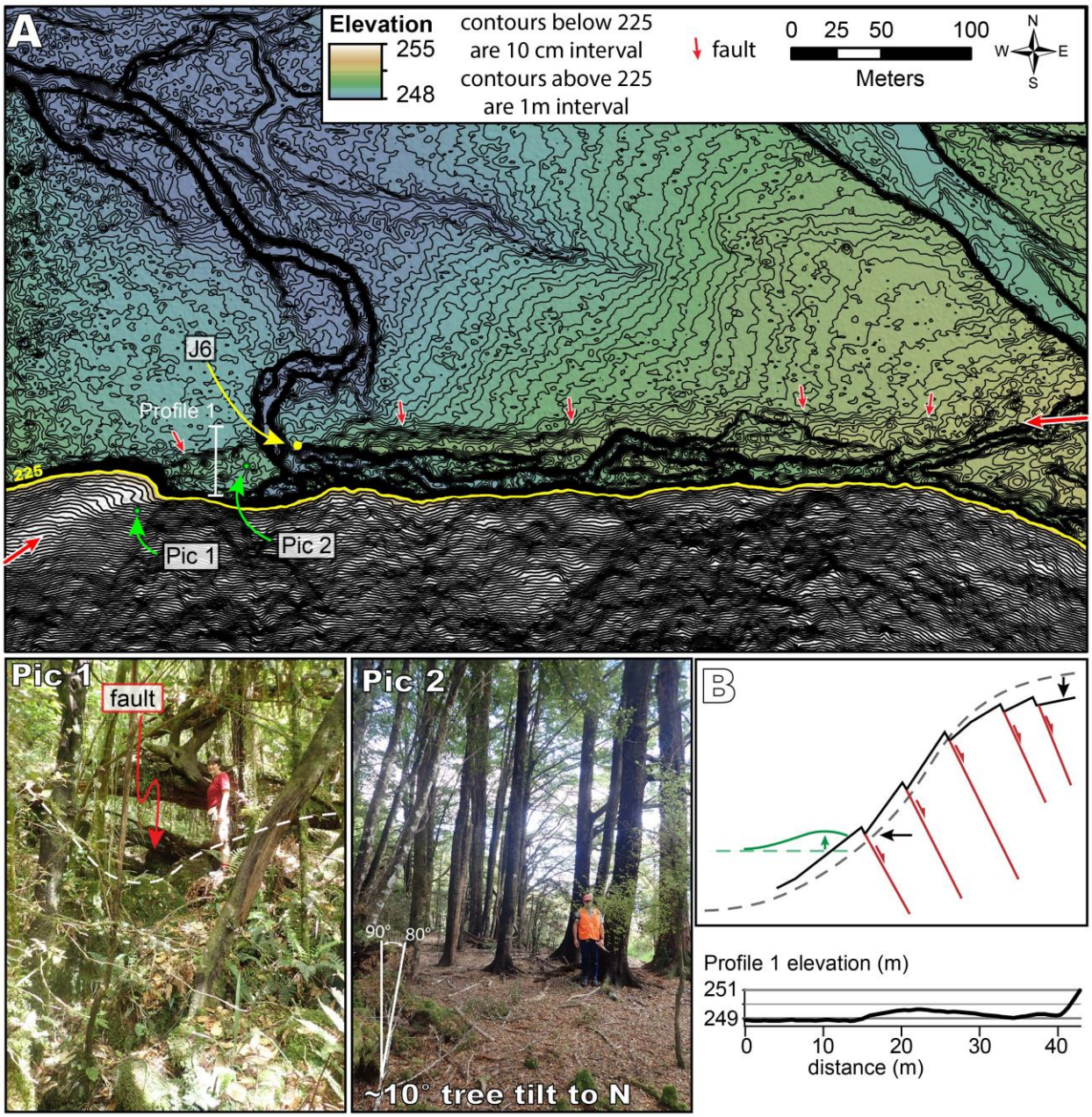

Figure 13. Map and site information for Site 7: J6. A) Site map showing elevation and J6 sample location, and picture locations. This area is located on the south side of the Taramakau River valley at the base of One Shot Hill, the extent of this map is indicated on Figure 2. The contour interval is 10 cm below the elevation of 225 m, where the slope is low. Contour interval is 1 m above 225, to show the features on the steep hillside. The profile shows where the ~0.8-1 m high scarp deforms

the alluvial surface. The fault scarp is indicated by the red arrows. Pic 1 is looking WSW and shows the fault scarp on the hillside, where it displaces large boulders, forming a ~1.5 m trough, which is easily identified on the lidar as well. Pic 2 is looking west and shows a grove of trees on the fault scarp that are tilted 9-12° to the north. B) schematic showing how gravitational deformation of the mountain can cause the bedrock fault and bulldoze deformation of the fluvial sediments. Applied to this site, the schematic profile would be oriented N-S and extend from the top of One Shot Hill into the Taramakau River valley. Black lines represent the bedrock hillslope, and green represents the valley sediments. Pre-deformation topography is represented by the dashed lines and solid lines represent post-deformation. Arrows indicate the location and direction of different components of deformation.

Styx

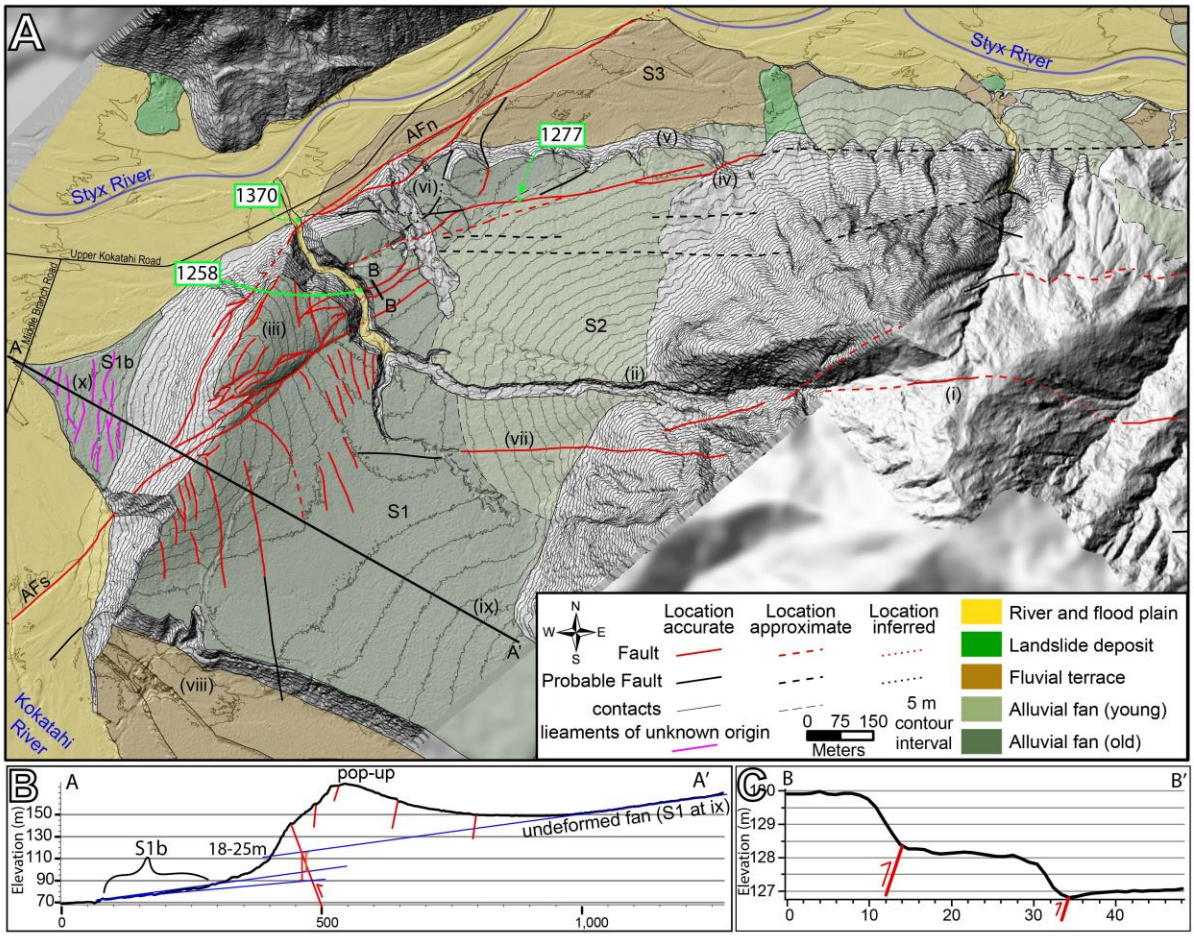

Figure 14. A) Geomorphic map of Site 8: Styx River, with trench and exposure sites and topographic profiles. Locations of interest referenced in the text are indicated with roman numerals in parentheses. The locations of trenches and outcrops are shown in green boxes. Fault mapping is from Vermeer et al. (2021). Geomorphic unit mapping has been refined for this study. B) Profile used for vertical slip-rate measurement. C) Profile of fault scarp of the fault exposed at site 1258.

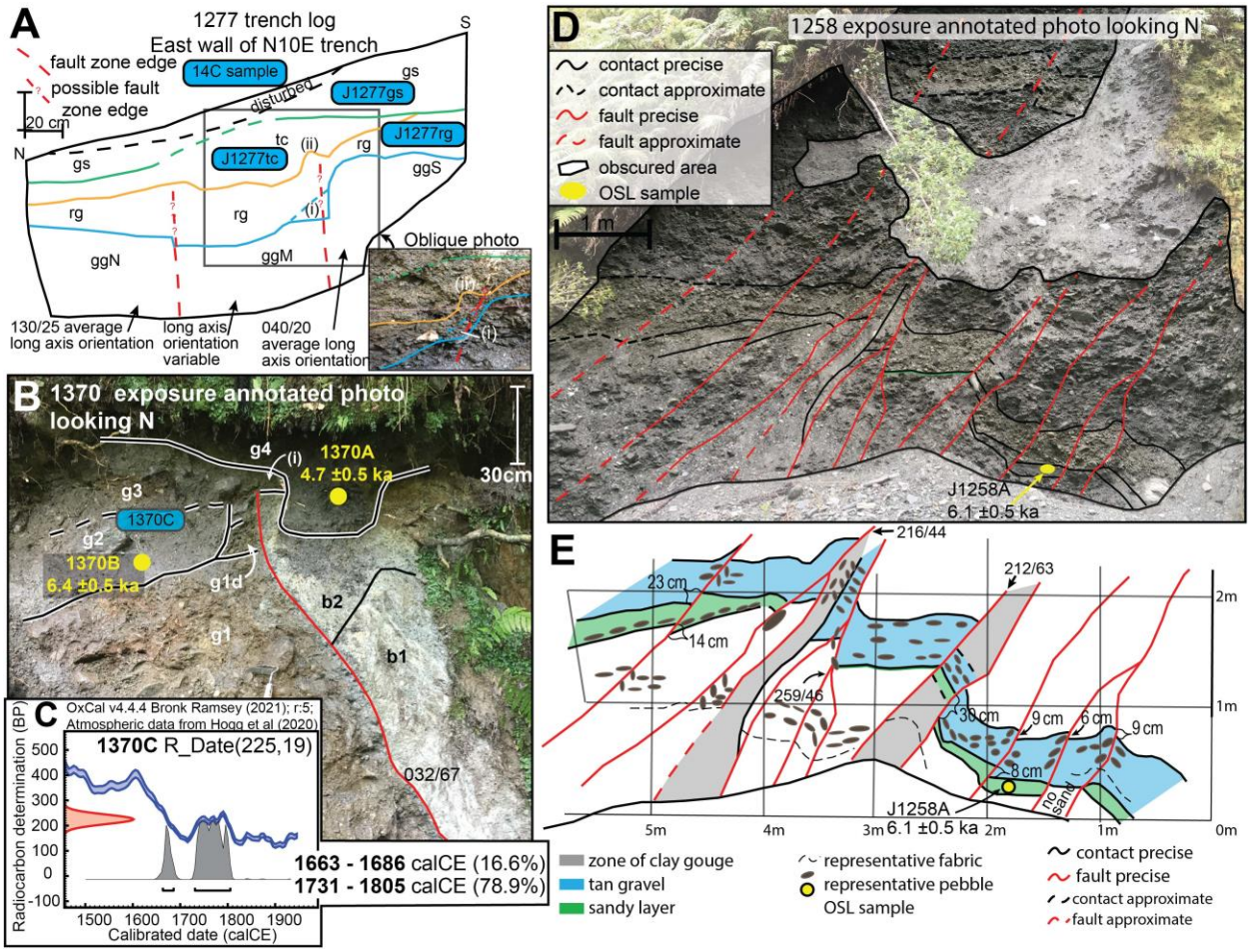

Figure 15. A) Log of the east wall of the hand-dug trench 1277 with annotated photo. Photo was taken oblique to the trench wall, extent indicated on log with black box. 14C sample locations are shown in blue, parenthetical roman numerals reference positions mentioned in the text. Colours of unit contacts correspond to annotations in the photo. The central area between the dashed red lines of non-imbricated gravel is interpreted as the fault zone. Dashed question mark upper fault extent is because of uncertainty whether unit Rg is faulted. All three 14C samples returned modern ages. B) Exposure 1370, photo with annotations and sample locations. A) Solid lines are sharp contacts, dashed lines are gradational contacts. Fault is shown in red, fault strikes 032° and dips 67°E. OSL samples are shown with yellow circles, 14C sample location with blue oval. Units are described in the text. C) Calibration curve for 14C sample 1370C, calibrated age is 1663-1805 CE. D)

Exposure 1258 annotated photo. E) Exposure 1258 gridded outcrop log. The yellow circle indicates the location of OSL sample 1258A. Distinctive tan gravel unit and underlying thin sand are shown in the annotated log.

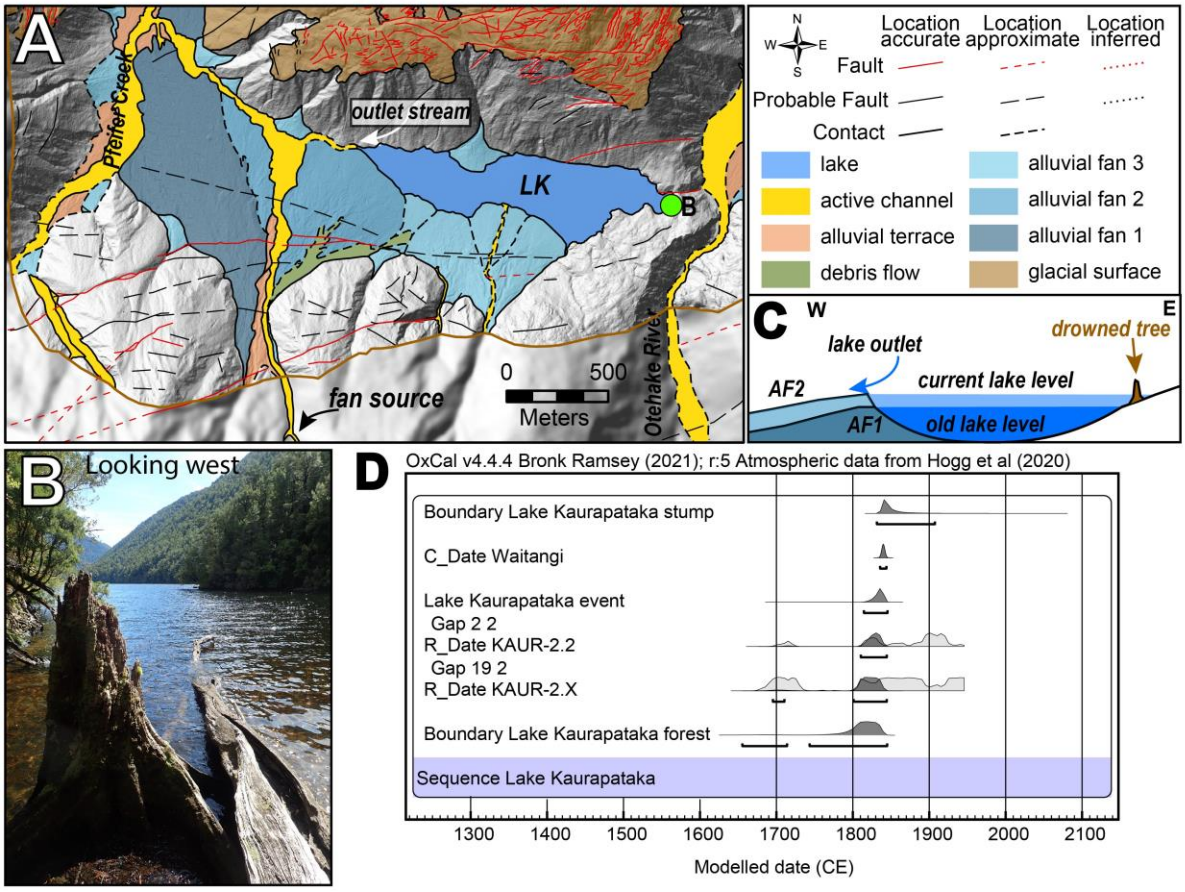

Figure 16. Lake Kaurapataka drowned tree. A) Lake Kaurapataka (LK) and surrounding fault and geomorphic mapping. The location of the dead tree is shown by a green dot at the east end of the lake. B) Dead in-situ tree stump sampled in Lake Kaurapataka. C) Schematic of how a younger

alluvial fan (AF2) can raise the lake level by damming the outlet, resulting in drowning the trees along the formerly dry edge. D) Oxcal model for the death age of the Lake Kaurapataka samples tree.

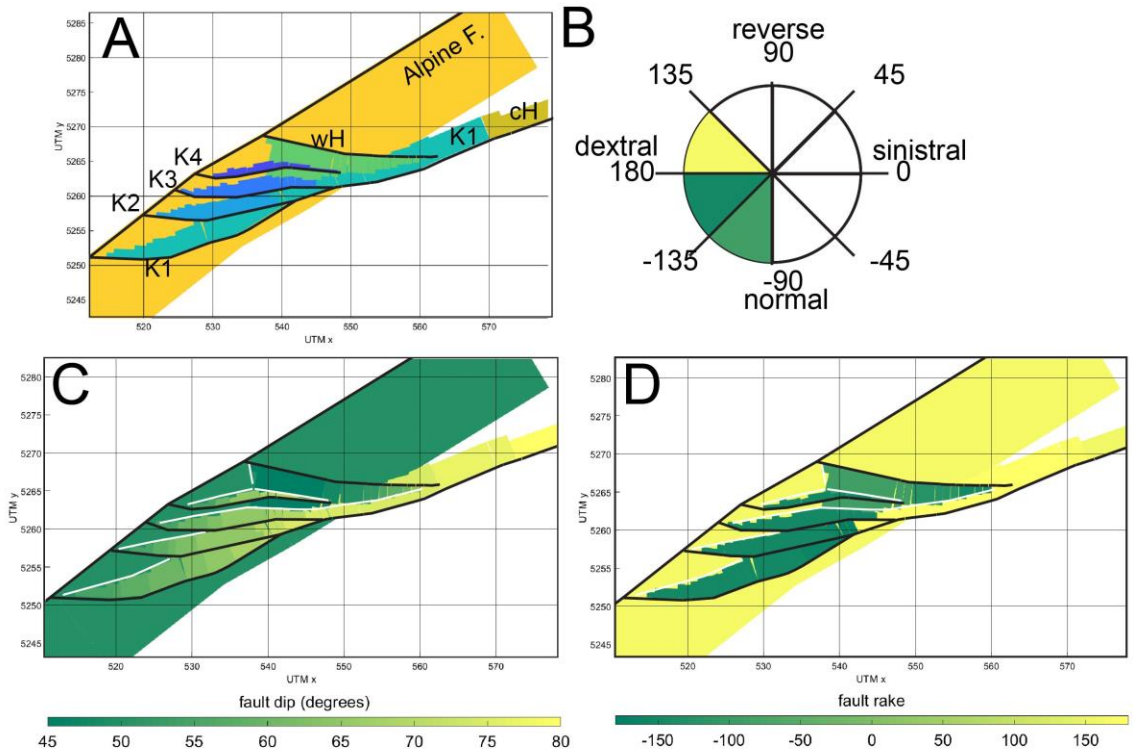

Figure 17. Fault geometry of the CFS fault model. A) 3D fault model with each fault in a different colour. cH – central Hope fault (Hurunui segment), K1 – Kelly fault southern splay, K2 K3 K4 – Kelly splay faults, wH – westernmost Hope fault (Michaels Creek to Alpine fault). B) Notation used for fault rake following the convention of Aki and Richards (1980). C) Modelled fault dips. D) Modelled fault rakes.

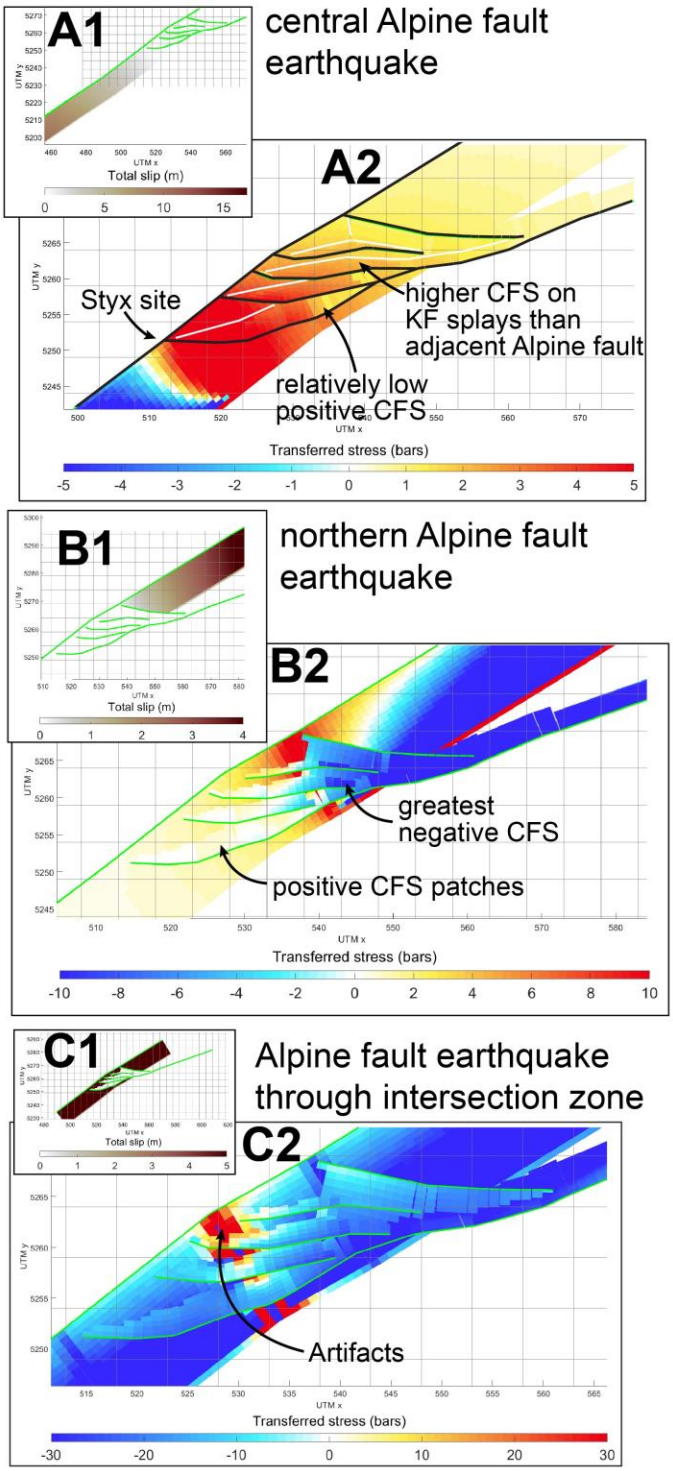

Figure 18. Coulomb fault stress change modeling results for Alpine fault earthquakes. Source earthquake parameters are listed in Table 4. A1) Source slip for central Alpine fault earthquake. A2) Coulomb stress changes from the central Alpine fault earthquake. B1) Source slip for northern

Alpine fault earthquake. B2) Coulomb stress transfer resulting from the northern Alpine fault earthquake. C1) Uniform Alpine fault slip (5m) through the intersection zone. C2) Coulomb stress change resulting from the uniform slip. High positive stress patches on the Alpine fault and Kelly splays at the bend are likely an artifact due to the Alpine fault being split into two fault surfaces to create the source fault. Overall the whole Hope-Kelly fault system receives negative stress change.

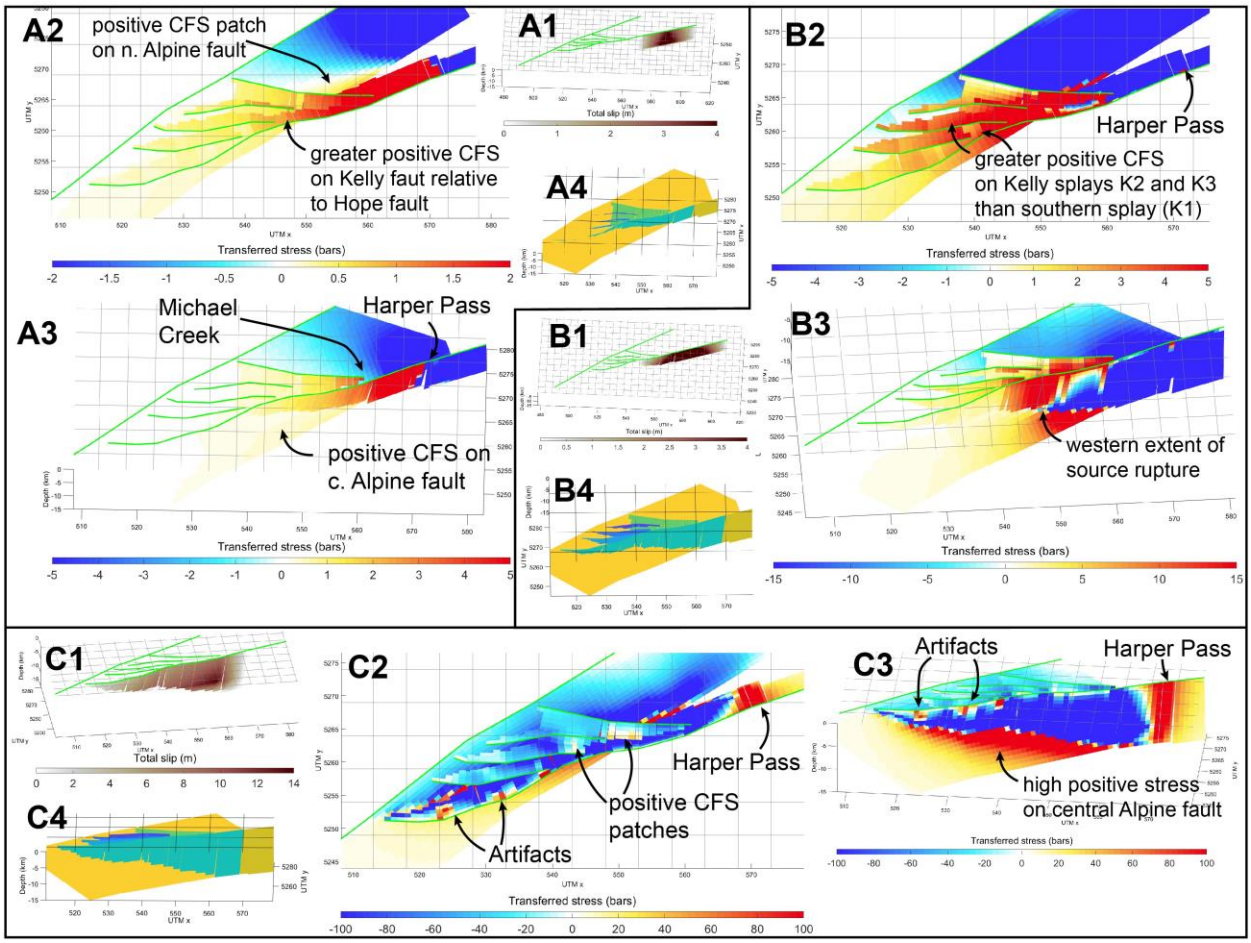

Figure 19. CFS model results for earthquakes on the Hope-Kelly faults. Source earthquake parameters are listed in Table 4. A1) Slip distribution for the source earthquake on the Hurunui segment of the Hope fault extending west to Harper Pass. A2-3) CFS results for a source earthquake with two different stretch values for the coloring. A4) fault model colored by fault name oriented similar to A3. B1) Slip distribution for the Hope-Kelly source earthquake on the

Hurunui section of the Hope fault and extending west to ~10 km east of the Alpine fault surface trace, where the Kelly fault and Alpine fault intersect within the seismogenic zone. B2-3) CFS results with two different stretch colors and an oblique view to show the positive stress transfer on the central Alpine fault. B4) Fault model colored by fault name, at similar orientation as B3. C1) Source earthquake slip distribution for a full Kelly southern splay rupture. C2-3) CFS results. The patches of positive stress on the source fault are artifacts. C4) Fault model colored by fault name oriented similar to C3.

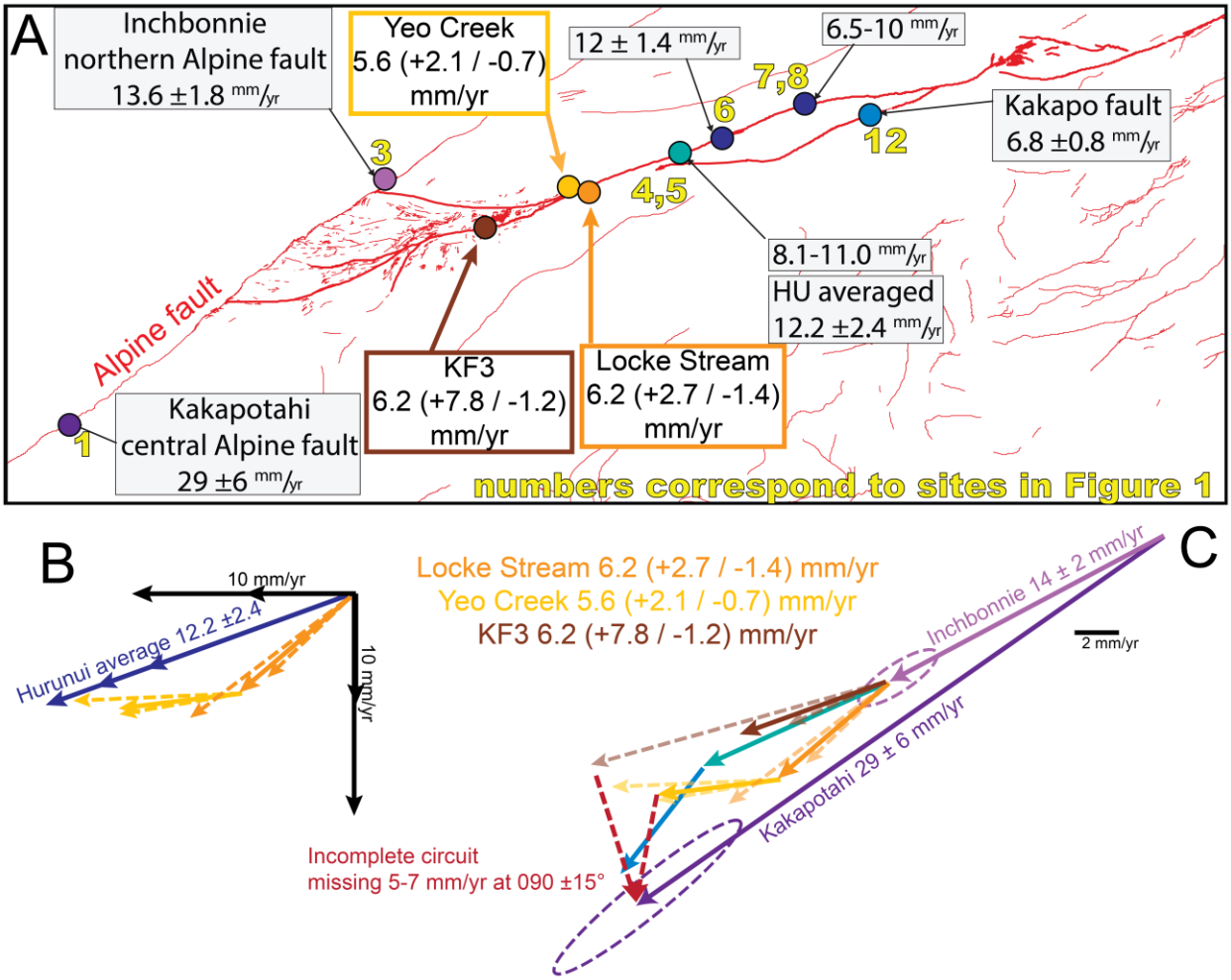

Figure 20. Slip circuits. A) Map showing the slip-rate measurements on the Alpine fault and Hope fault. B) The combined horizontal slip vectors from Locke Stream and Yeo Creek in the Hope-Kelly fault system are within error of the average eastern Hurunui Section HSV. C) The Alpine fault HSV from the central and northern sections, taken from slip-rates at Kakapotahi and Inchbonnie and assuming fault dip of 50 degrees (Norris and Cooper, 2001; Langridge et al., 2010). The eastern Hurunui average HSV (Khajavi et al., 2018), and the combined Yeo and Lock slip vectors, all fall short of completing the Alpine fault slip decrease. The missing HSV is 5-7 mm/yr at 090 +- 15°.

Table 1. OSL dates table. Yellow shading indicates samples that are probably well bleached, based on the IR50/OSL age ratio being ≤1. Green shading indicates sample that is well bleached, based on IR50/OSL ratio being ≤1 and the pIRIR/OSL ratio being ~1.

Average dose recovery, IR_{50}	0.65 ± 0.02	(n= 39)
Average dose recovery, pIRIR -	1.26 ± 0.03	(n= 39)
Average dose recovery, quartz -	0.80 ± 0.06	(n= 36)

Note: w.c. - water content, (n) - number of aliquots

Lab. Code	Sample	Site	Depth, cm	w.c. %	IR_{50} D_e, Gy	(n)	pIRIR D_e, Gy	(n)	OSL D_e, Gy	(n)	feldspar dose rate, Gy/ka	quartz dose rate, Gy/ka	IR_{50} age, ka	pIRIR age, ka	OSL age, ka	IR_{50}/OSL age ratio	pIRIR/OSL age ratio
19 66 01	J6	New Zealand	120	42	12 ± 3	5	83 ± 11	6	9.1 ± 0.3	22	3.88 ± 0.11	2.95 ± 0.10	3.1 ± 0.7	21 ± 3	3.1 ± 0.2	1.0 ± 0.2	6.9 ± 1.0
19 66 02	J22	New Zealand	38	47	57 ± 10	6	389 ± 44	6	60.8 ± 2.7	22	3.38 ± 0.10	2.44 ± 0.08	17 ± 3	115 ± 14	24.9 ± 1.5	0.68 ± 0.13	4.6 ± 0.6
19 66 03	J29	New Zealand	15	27	23 ± 4	4	155 ± 30	6	9.6 ± 0.8	21	4.42 ± 0.14	3.48 ± 0.12	5.3 ± 0.9	35 ± 7	2.8 ± 0.3	1.9 ± 0.4	12.7 ± 2.8
19 66 04	J35	New Zealand	90	16	45 ± 7	5	297 ± 41	6	46.4 ± 2.5	19	3.97 ± 0.13	3.03 ± 0.12	11 ± 2	75 ± 11	15.3 ± 1.1	0.74 ± 0.13	4.9 ± 0.8
19 66 05	J36	New Zealand	23	33	46 ± 6	10	294 ± 27	10	37.0 ± 2.7	24	4.16 ± 0.13	3.22 ± 0.11	11.1 ± 1.4	71 ± 7	11.5 ± 1.0	0.97 ± 0.15	6.1 ± 0.8
19 66 06	J82	New Zealand	80	42	97 ± 9	4	162 ± 6	3	40.8 ± 2.4	26	3.81 ± 0.11	2.88 ± 0.09	25 ± 2	42 ± 2	14.2 ± 1.0	1.8 ± 0.2	3.0 ± 0.3
19 66 07	J106	New Zealand	40	42	104 ± 8	4	150 ± 22	3	87.0 ± 6.3	21	4.06 ± 0.12	3.12 ± 0.11	26 ± 2	37 ± 6	28 ± 2	0.92 ± 0.11	1.3 ± 0.2
19 66 08	J133	New Zealand	100	22	138 ± 8	4	253 ± 12	4	27.3 ± 1.2	29	4.45 ± 0.15	3.51 ± 0.13	31 ± 2	57 ± 3	7.8 ± 0.5	4.0 ± 0.4	7.3 ± 0.6
19 66 09	J134B	New Zealand	40	55	467 ± 26	4	1268 ± 28	4	30.5 ± 1.5	27	2.83 ± 0.08	1.89 ± 0.06	165 ± 11	448 ± 19	16.1 ± 1.0	10.2 ± 0.9	27.8 ± 2.0
19 66 10	J134C	New Zealand	50	24	152 ± 41	6	223 ± 36	4	28 ± 7	4	4.17 ± 0.14	3.23 ± 0.12	37 ± 10	53 ± 9	9 ± 2	4.2 ± 1.5	6.1 ± 1.8
19 66 11	J1258	New Zealand	2600	11	107 ± 71	2	189 ± 53	3	17.6 ± 1.6	23	3.81 ± 0.14	2.87 ± 0.13	28 ± 19	50 ± 14	6.1 ± 0.6	4.6 ± 3.1	8.1 ± 2.4
19 66 12	1370A	New Zealand	50	25	67 ± 12	5	101 ± 11	4	13.0 ± 1.3	24	3.70 ± 0.12	2.77 ± 0.10	18 ± 3	27 ± 3	4.7 ± 0.5	3.8 ± 0.8	5.8 ± 0.9
19 66 13	1370B	New Zealand	100	21	91 ± 22	6	205 ± 38	5	17.4 ± 1.3	23	3.67 ± 0.13	2.73 ± 0.11	25 ± 6	56 ± 11	6.4 ± 0.5	3.9 ± 1.0	8.8 ± 1.8

probably well bleached
well bleached

Table 2. OSL dose rate table

Lab. Code	^{238}U	^{226}Ra	^{232}Th	^{40}K	beta dose rate	gamma dose rate
	$Bq.kg^{-1}$	$Bq.kg^{-1}$	$Bq.kg^{-1}$	$Bq.kg^{-1}$	$Gy.ka^{-1}$	$Gy.ka^{-1}$
19 66 01	50 ± 5	40.6 ± 0.9	55.9 ± 0.7	826 ± 14	2.87 ± 0.05	1.59 ± 0.04
19 66 02	35 ± 5	45.3 ± 1.0	58.7 ± 0.8	556 ± 13	2.25 ± 0.05	1.45 ± 0.04
19 66 03	45 ± 5	45.7 ± 0.7	61.6 ± 0.7	804 ± 12	2.90 ± 0.04	1.68 ± 0.04
19 66 04	29 ± 3	32.7 ± 0.6	44.4 ± 0.5	680 ± 9	2.34 ± 0.03	1.29 ± 0.03
19 66 05	59 ± 15	37.4 ± 1.3	62.0 ± 1.3	807 ± 21	2.83 ± 0.06	1.63 ± 0.04
19 66 06	45 ± 5	37.5 ± 0.7	56.5 ± 0.7	796 ± 14	2.77 ± 0.04	1.56 ± 0.03
19 66 07	60 ± 12	50.0 ± 1.2	76.8 ± 1.2	719 ± 22	2.84 ± 0.06	1.82 ± 0.05
19 66 08	46 ± 5	44.3 ± 0.8	59.3 ± 0.7	800 ± 13	2.86 ± 0.04	1.64 ± 0.04
19 66 09	42 ± 4	32.5 ± 0.6	39.9 ± 0.6	504 ± 10	1.87 ± 0.03	1.09 ± 0.03
19 66 10	44 ± 10	39.3 ± 1.0	55.7 ± 1.0	744 ± 20	2.65 ± 0.06	1.52 ± 0.04
19 66 11	24 ± 4	32.3 ± 0.6	47.4 ± 0.6	611 ± 11	2.19 ± 0.03	1.27 ± 0.03
19 66 12	31 ± 8	33.1 ± 0.8	47.1 ± 0.8	641 ± 16	2.27 ± 0.05	1.29 ± 0.03
19 66 13	55 ± 14	29.2 ± 1.2	43.9 ± 1.2	635 ± 19	2.19 ± 0.05	1.22 ± 0.03

Table 3. Slip-rates determined in this study.

Slip-rate Results						
Site	Latitude	Longitude	Net slip	strike-slip	dip-slip	feature age
KF1a	-42.742	171.835	6.2 (+2.7/-1)	6.2 (+2.4/-1.3)	0.4 (+0.1/-0.1)	14.5 ±1.6 ka
KF2	-42.7774	171.72825	1.7 (+2.2/-0.3)	1.2 (+1.5/-0.5)	1.2 (+1.4/-0.3)	13. ±2.9 ka
KF3	-42.7897	171.67192	6.2 (+7.8/-1.2)	6.1 (+6.8/-2.1)	1.3 (+1.4/-0.3)	13. ±2.9 ka
Yeo R3/4	-42.7485	171.79601	5.6 (+2.1/-0.7)	5.6 (+1.7/-1.1)	0.7 (+0.2/-0.1)	11.7 ±1.4 ka
SHa NNE fault	-42.7656	171.7109	1.3 (+0.1/-0.4)	1.3 (+0.2/-0.3)	0 (+0/-0)	16. ±.5 ka
SHb EW fault	-42.7718	171.70565	1.3 (+0.1/-0.4)	1.3 (+0.2/-0.3)	0 (+0/-0)	16. ±.5 ka
MC R4/5	-42.7579	171.75781	1.7 (+1.1/-0.4)	1.6 (+0.9/-0.6)	0.3 (+0.1/-0)	7.3 ±1.4 ka
MC5t	-42.7579	171.75819	0.9 (+0.9/-0.4)	0.9 (+0.9/-0.5)	0.2 (+0.1/-0)	7.3 ±1.4 ka
MC R5/6	-42.7579	171.75841	1.1 (+0.9/-0.5)	1.1 (+0.9/-0.5)	0.1 (+0.1/-0)	7.3 ±1.4 ka
Styx	-42.8909	171.14652			6.3 (+3.2/-1.9)	

Table 4. CFS earthquake scenario source parameters

Results figures	**Source fault**	**Rupture termination point**	**Rupture length (km)**	**Magnitude**	**Percent slip at surface***	**Maximum displacement (m)**	**Rake ****	**Seismogenic depth (km)**
Figure 18 A1-2	central Alpine fault	North end at Alpine/Kelly southern splay intersection	324	8.1	90	15	168	12
Figure 18 B1-2	northern Alpine fault	South end at Alpine/westernmost Hope intersection	120	7.4	90	4	166	12
Figure 18 C1-2	Alpine fault through intersection zone	~20 km north and south of intersection zone	97	-	100	5	168 to 166	15
Figure 19 A1-4	central Hope fault	Hurunui section to Hope/Kelly branch point at Harper Pass	36	7	70	4	160	12
Figure 19 B1-4	eastern Kelly fault (southernmost splay)	Hurunui section to ~10 km east of the Alpine fault, where Kelly fault intersects the Alpine fault at ~10-15 km depth	65	7.3	60	4	160 to 180	12
Figure 19 C1-4	whole Kelly fault (southernmost splay)	Surface intersection of Alpine/Kelly faults to Harper Pass	62	7.3	60	14	-150 to 180	12

* Dolan and Haravitch, 2014

** Aki and Richards, 1980

Appendix A

Slip-rate input values and PDFs and output PDFs

@RISK Input Results
Performed By: Jessie Vermeer
Date: Sunday, 30 January 2022 2:15:58 PM
slip_rate_calcs_at_risk_14-10-2021.xlsx

Name	Cell	Graph	Min	Mean	Max	5%	95%	Errors
KF1a / age min	B6	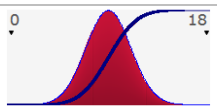	0.1	9.0	17.7	5.7	12.3	0
KF1a / age pref	C6	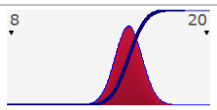	11.5	15.2	19.0	13.9	16.5	0
KF1a / age max	D6	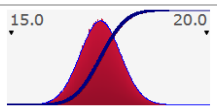	15.4	17.3	19.6	16.5	18.1	0
KF1a / age distribution	E6	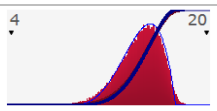	5.3	14.5	18.7	11.5	16.8	0
KF1a / SS distribution	I6	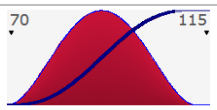	70.4	91.0	111.6	78.0	104.0	0
KF1a / VD distribution	M6	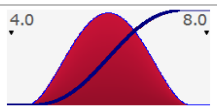	4.4	6.0	7.6	5.0	7.0	0
KF1a / strike distribution	Q6	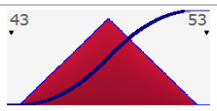	43.6	48.0	52.4	45.0	51.0	0
KF1a / dip distribution	U6	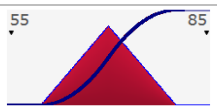	60.0	70.0	80.0	63.2	76.8	0
KF1b / age min	B7	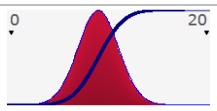	0.4	9.0	18.1	5.7	12.3	0

KF1b / age pref	C7	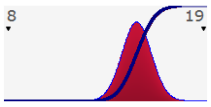	11.9	15.2	18.9	13.9	16.5	0
KF1b / age max	D7	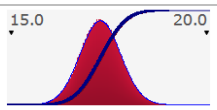	15.1	17.3	19.7	16.5	18.1	0
KF1b / age distribution	E7	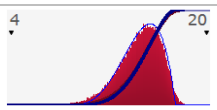	5.5	14.5	18.9	11.5	16.8	0
KF1b / SS distribution	I7	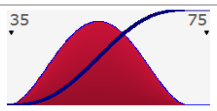	35.6	53.0	70.5	42.0	64.0	0
KF1b / VD distribution	M7	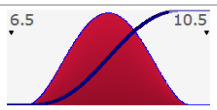	6.9	8.5	10.1	7.5	9.5	0
KF1b / strike distribution	Q7	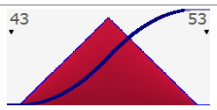	43.6	48.0	52.4	45.0	51.0	0
KF1b / dip distribution	U7	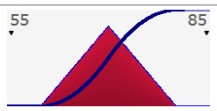	60.0	70.0	80.0	63.2	76.8	0
KF2 / age pref	C9	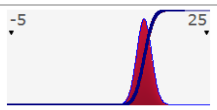	10.4	15.3	20.1	13.5	17.1	0
KF2 / age max	D9	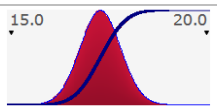	15.1	17.3	19.5	16.5	18.1	0
KF2 / age distribution	E9	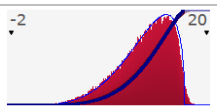	1.0	13.0	18.8	7.4	16.8	4901
KF2 / SS distribution	I9	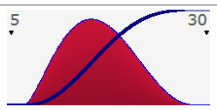	7.2	16.2	28.1	10.0	23.0	0
KF2 / VD distribution	M9	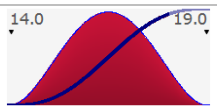	14.1	16.5	18.9	15.0	18.0	0
KF2 / strike distribution	Q9	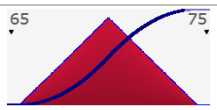	65.6	70.0	74.4	67.0	73.0	0
KF2 / dip distribution	U9	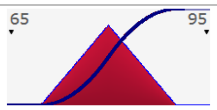	70.0	80.0	90.0	73.2	86.8	0

KF3 / age pref	C8	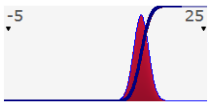	10.2	15.3	20.0	13.5	17.1	0
KF3 / age max	D8	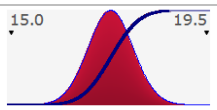	15.1	17.3	19.4	16.5	18.1	0
KF3 / age distribution	E8	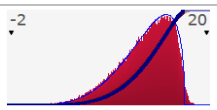	1.0	13.0	18.8	7.5	16.8	4888
KF3 / SS distribution	I8	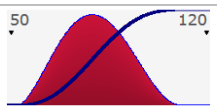	53.8	80.2	109.5	63.0	98.0	0
KF3/ VD distribution	M8	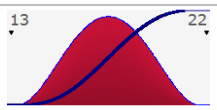	13.5	17.5	21.5	15.0	20.0	0
KF3 / strike distribution	Q8	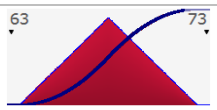	63.6	68.0	72.4	65.0	71.0	0
KF3 / dip distribution	U8	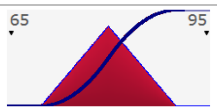	70.0	80.0	90.0	73.2	86.8	0
MC R3-1 / dip distribution	U17	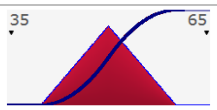	40.0	50.0	60.0	43.2	56.8	0
MC R4/5 / min	B13	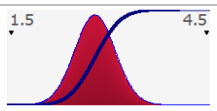	1.5	2.8	4.1	2.3	3.3	0
MC R4/5 / age	C13	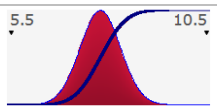	5.6	7.8	10.0	7.0	8.6	0
MC R4/5 / max	D13	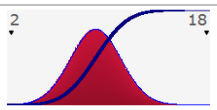	2.4	9.0	17.7	5.7	12.3	0
MC R4/5 / distribution	E13	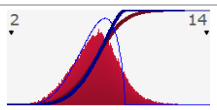	2.6	7.3	13.6	5.0	9.5	27873
MC R4/5 / SS distribution	I13	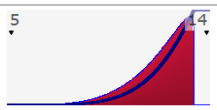	5.7	11.8	13.3	9.4	13.2	0
MC R4/5 / VD distribution	M13	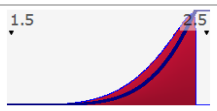	1.6	2.3	2.4	2.0	2.4	0

MC R4/5 / strike distribution	Q13	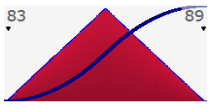	83.1	86.0	88.9	84.0	88.0	0
MC R4/5 / dip distribution	U13	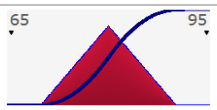	70.0	80.0	90.0	73.2	86.8	0
MC R5/6 / min	B15	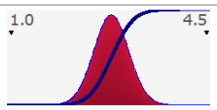	1.4	2.8	4.1	2.3	3.3	0
MC R5/6 / age	C15	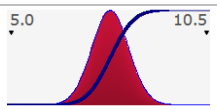	5.4	7.8	10.3	7.0	8.6	0
MC R5/6 / max	D15	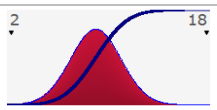	2.5	9.0	17.7	5.7	12.3	0
MC R5/6 / distribution	E15	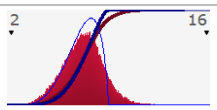	2.7	7.3	14.1	4.9	9.5	27997
MC R5/6 / SS distribution	I15	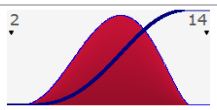	2.9	8.4	12.8	5.2	11.4	0
MC R5/6 / VD distribution	M15	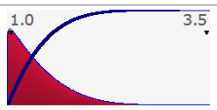	1.0	1.4	3.0	1.0	2.0	0
MC R5/6 / strike distribution	Q15	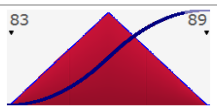	83.1	86.0	88.9	84.0	88.0	0
MC R5/6 / dip distribution	U15	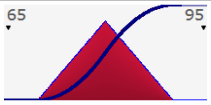	70.0	80.0	90.0	73.2	86.8	0
MC R6/8 / min	B16	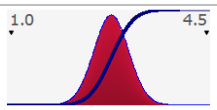	1.5	2.8	4.1	2.3	3.3	0
MC R6/8 / max	D16	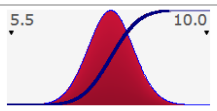	5.7	7.8	10.0	7.0	8.6	0
MC R6/8 / distribution	E16	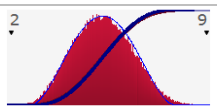	2.1	5.3	8.9	3.7	7.0	0
MC R6/8 / SS distribution	I16	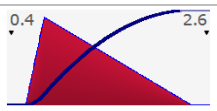	0.6	1.3	2.4	0.7	2.0	0

MC R6/8 / VD distribution	M16	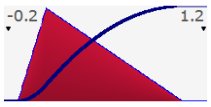	-0.1	0.3	1.0	0.0	0.8	0
MC R6/8 / strike distribution	Q16	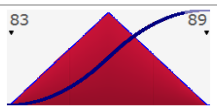	83.1	86.0	88.9	84.0	88.0	0
MC R6/8 / dip distribution	U16	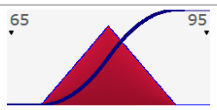	70.0	80.0	90.0	73.2	86.8	0
MC5t / min	B14	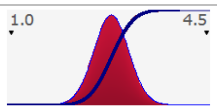	1.4	2.8	4.5	2.3	3.3	0
MC5t / age	C14	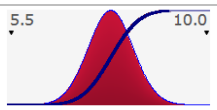	5.7	7.8	10.0	7.0	8.6	0
MC5t / max	D14	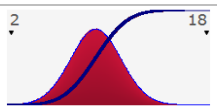	2.4	9.0	17.6	5.7	12.3	0
MC5t / distribution	E14	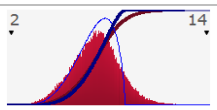	2.2	7.3	13.8	4.9	9.5	28022
MC5t / SS distribution	I14	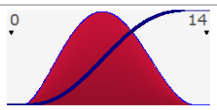	1.2	6.7	12.9	3.1	10.5	0
MC5t / VD distribution	M14	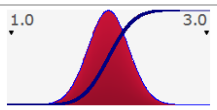	1.1	2.0	2.9	1.7	2.3	0
MC5t / strike distribution	Q14	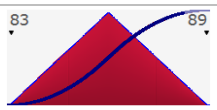	83.1	86.0	88.9	84.0	88.0	0
MC5t / dip distribution	U14	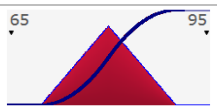	70.0	80.0	90.0	73.2	86.8	0
SHa NNE fault / min	B11	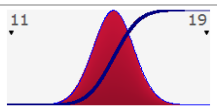	11.2	15.2	18.8	13.9	16.5	0
SHa NNE fault / max	D11	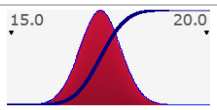	15.0	17.3	19.6	16.5	18.1	0
SHa NNE fault / distribution	E11	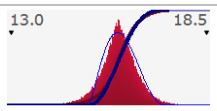	13.4	16.0	18.3	15.3	16.8	16257

SHa NNE fault / SS distribution	I11	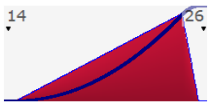	14.7	21.6	25.5	17.0	24.8	0
SHa NNE fault / VD distribution	M11	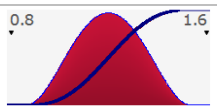	0.9	1.2	1.5	1.0	1.4	0
SHa NNE fault / strike distribution	Q11	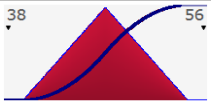	39.7	47.0	54.3	42.0	52.0	0
SHa NNE fault / dip distribution	U11	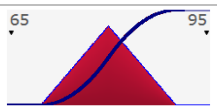	70.0	80.0	90.0	73.2	86.8	0
SHb EW fault / min	B12	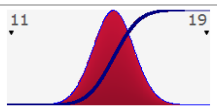	11.8	15.2	18.6	13.9	16.5	0
SHb EW fault / max	D12	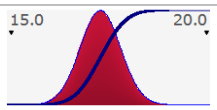	15.0	17.3	19.7	16.5	18.1	0
SHb EW fault / distribution	E12	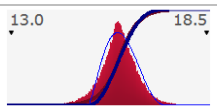	13.4	16.0	18.3	15.2	16.8	16263
SHb EW fault / SS distribution	I12	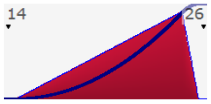	14.7	21.6	25.5	17.0	24.8	0
SHb EW fault / VD distribution	M12	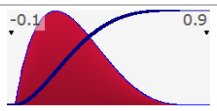	-0.1	0.2	0.8	0.0	0.5	0
SHb EW fault / strike distribution	Q12	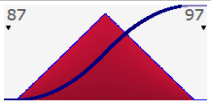	87.6	92.0	96.4	89.0	95.0	0
Styx / min	B17	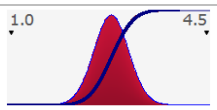	1.4	2.8	4.1	2.3	3.3	0
Styx / max	D17	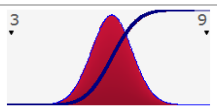	3.5	6.1	8.8	5.1	7.1	0
Styx / distribution	E17	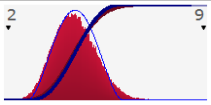	2.2	4.4	8.1	3.3	5.7	0
Styx / VD distribution	M17	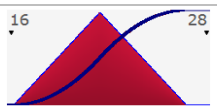	16.4	21.5	26.6	18.0	25.0	0

Yeo R3/4 / age min	B10	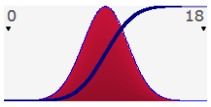	0.4	9.0	17.5	5.7	12.3	0
Yeo R3/4 / age pref	C10	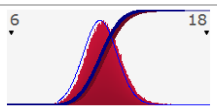	7.3	11.8	17.8	10.1	13.5	0
Yeo R3/4 / age max	D10	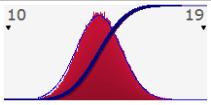	10.8	14.3	18.7	12.7	15.9	0
Yeo R3/4 / age distribution	E10	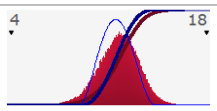	4.6	11.7	17.9	9.3	13.8	0
Yeo R3/4 / SS distribution	I10	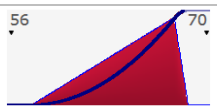	57.7	64.6	68.5	60.0	67.8	0
Yeo R3/4 / VD distribution	M10	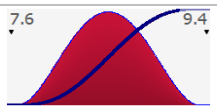	7.7	8.5	9.3	8.0	9.0	0
Yeo R3/4 / strike distribution	Q10	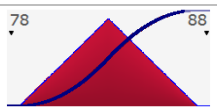	78.6	83.0	87.4	80.0	86.0	0
Yeo R3/4 / dip distribution	U10	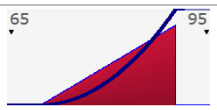	70.0	83.3	90.0	74.5	89.5	0
strike distribution	Q18					n/a	n/a	100000
strike distribution	Q19	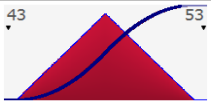	43.6	48.0	52.4	45.0	51.0	0
strike distribution	Q20	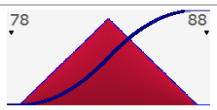	78.6	83.0	87.4	80.0	86.0	0
strike distribution	Q21	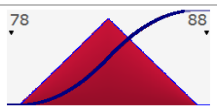	78.6	83.0	87.4	80.0	86.0	0
J82 / age min	B20	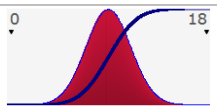	0.1	9.0	17.6	5.7	12.3	0
J82 / age min	B21	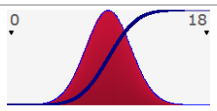	0.5	9.0	18.0	5.7	12.3	0

J82 / age pref	C20	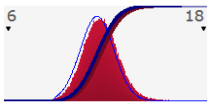	7.2	11.8	17.7	10.1	13.5	0
J82 / age pref	C21	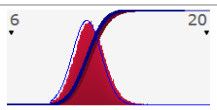	7.7	11.8	18.2	10.1	13.5	0
J82 / age max	D20	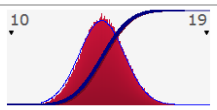	10.1	14.3	18.5	12.7	15.9	0
J82 / age max	D21	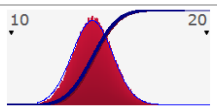	10.6	14.3	19.5	12.7	15.9	0
J82 / age distribution	E20	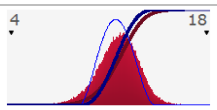	4.0	11.7	17.7	9.4	13.8	0
J82 / age distribution	E21	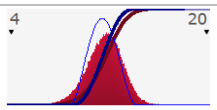	4.4	11.7	18.2	9.3	13.9	0
J82 / dip distribution	U20	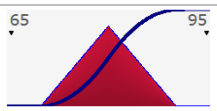	70.0	80.0	90.0	73.2	86.8	0
J82 / dip distribution	U21	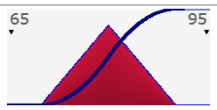	70.0	80.0	90.0	73.2	86.8	0
J82 upper / SS distribution	I20	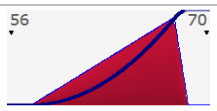	57.7	64.6	68.5	60.0	67.8	0
J82 upper / SS distribution	I21	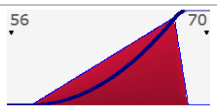	57.7	64.6	68.5	60.0	67.8	0
KF1 / SS distribution	I19	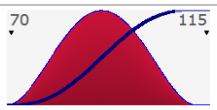	70.3	91.0	111.8	78.0	104.0	0
KF1a / age min	B6	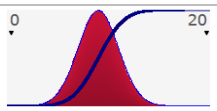	0.3	9.0	18.2	5.7	12.3	0
KF1a / age pref	C6	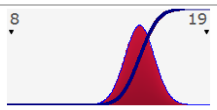	11.7	15.2	18.8	13.9	16.5	0
KF1a / age max	D6	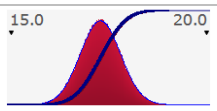	15.2	17.3	19.6	16.5	18.1	0

KF1a / age distribution	E6	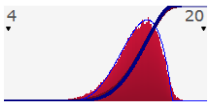	4.9	14.5	18.7	11.5	16.8	0
KF1a / SS distribution	I6	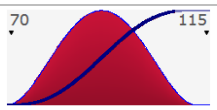	70.4	91.0	111.8	78.0	104.0	0
KF1a / VD distribution	M6	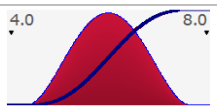	4.4	6.0	7.6	5.0	7.0	0
KF1a / strike distribution	Q6	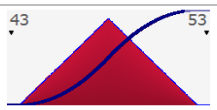	43.6	48.0	52.4	45.0	51.0	0
KF1a / dip distribution	U6	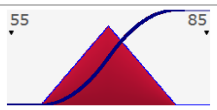	60.0	70.0	80.0	63.2	76.8	0
KF1a (old min age) / age min	B19	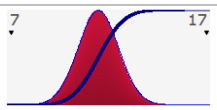	7.1	11.5	16.4	9.9	13.1	0
KF1a (old min age) / age pref	C19	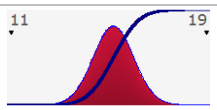	11.8	15.2	18.9	13.9	16.5	0
KF1a (old min age) / age max	D19	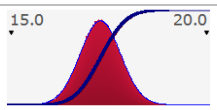	15.3	17.3	19.6	16.5	18.1	0
KF1a (old min age) / age distribution	E19	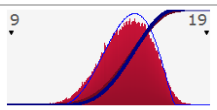	9.8	14.9	18.6	12.8	16.8	0
KF1a (old min age) / dip distribution	U19	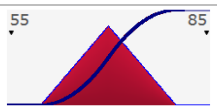	60.0	70.0	80.0	63.2	76.8	0
KF1b / age min	B7	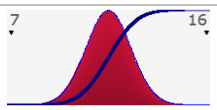	7.1	11.5	15.9	9.9	13.1	0
KF1b / age pref	C7	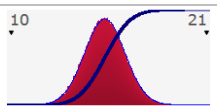	10.9	15.3	20.0	13.5	17.1	0
KF1b / age max	D7	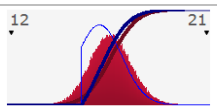	13.0	16.6	20.8	15.1	18.1	0
KF1b / age distribution	E7	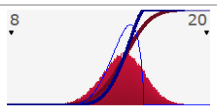	9.6	14.9	19.7	12.8	16.9	0

KF1b / SS distribution	I7	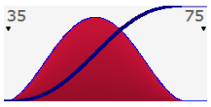	35.5	53.0	70.4	42.0	64.0	0
KF1b / strike distribution	Q7	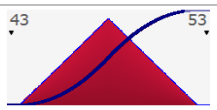	43.6	48.0	52.4	45.0	51.0	0
KF2 / age pref	C9	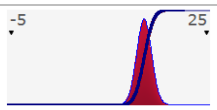	10.4	15.3	20.2	13.5	17.1	0
KF2 / age max	D9	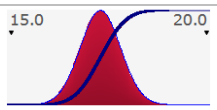	15.1	17.3	19.6	16.5	18.1	0
KF2 / age distribution	E9	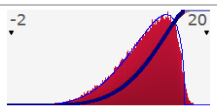	0.8	13.0	18.9	7.5	16.8	4965
KF2 / SS distribution	I9	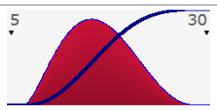	7.2	16.2	27.9	10.0	23.0	0
KF2 / VD distribution	M9	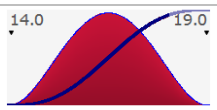	14.1	16.5	18.9	15.0	18.0	0
KF2 / VD distribution	M20	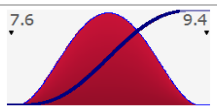	7.7	8.5	9.3	8.0	9.0	0
KF2 / VD distribution	M21	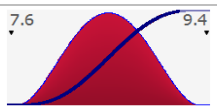	7.7	8.5	9.3	8.0	9.0	0
KF2 / strike distribution	Q9	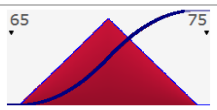	65.6	70.0	74.4	67.0	73.0	0
KF2 / dip distribution	U9	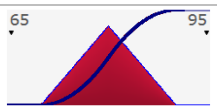	70.0	80.0	90.0	73.2	86.8	0
KF3 / age pref	C8	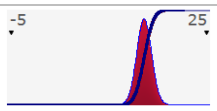	10.6	15.3	20.1	13.5	17.1	0
KF3 / age max	D8	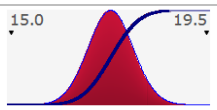	15.1	17.3	19.5	16.5	18.1	0
KF3 / age distribution	E8	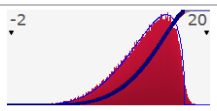	1.0	13.0	18.6	7.5	16.8	4931

KF3 / SS distribution	I8	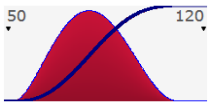	53.7	80.2	109.7	63.0	98.0	0
KF3/ VD distribution	M8	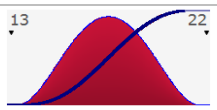	13.5	17.5	21.5	15.0	20.0	0
KF3 / strike distribution	Q8	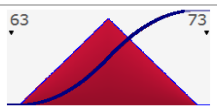	63.6	68.0	72.4	65.0	71.0	0
KF3 / dip distribution	U8	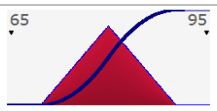	70.0	80.0	90.0	73.2	86.8	0
Locke highest fan / VD distribution	M7	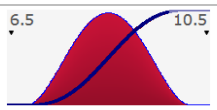	6.9	8.5	10.1	7.5	9.5	0
Locke highest fan / VD distribution	M19	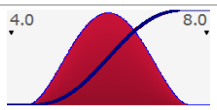	4.4	6.0	7.6	5.0	7.0	0
Locke highest fan / dip distribution	U7	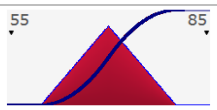	60.0	70.0	80.0	63.2	76.8	0
MC R3-1 / dip distribution	U18	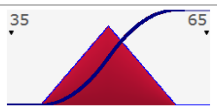	40.0	50.0	60.0	43.2	56.8	0
MC R4/5 / SS distribution	I13	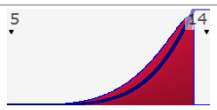	5.6	11.8	13.3	9.4	13.2	0
MC R4/5 / VD distribution	M13	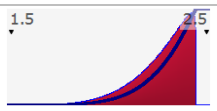	1.6	2.3	2.4	2.0	2.4	0
MC R4/5 / strike distribution	Q13	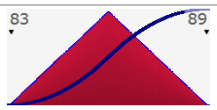	83.1	86.0	88.9	84.0	88.0	0
MC R4/5 / dip distribution	U13	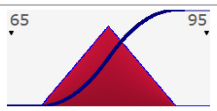	70.0	80.0	90.0	73.2	86.8	0
MC R4/5 / min	B13	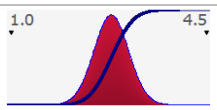	1.5	2.8	4.1	2.3	3.3	0

MC R4/5 / age	C13	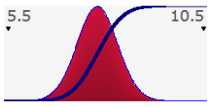	5.7	7.8	10.3	7.0	8.6	0
MC R4/5 / max	D13	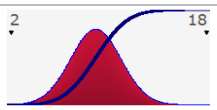	2.3	9.0	17.7	5.7	12.3	0
MC R4/5 / distribution	E13	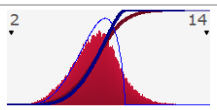	2.7	7.3	13.9	4.9	9.5	27874
MC R5/6 / SS distribution	I15	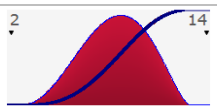	2.9	8.4	12.8	5.2	11.4	0
MC R5/6 / VD distribution	M15	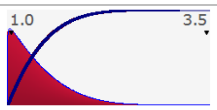	1.0	1.4	3.0	1.0	2.0	0
MC R5/6 / strike distribution	Q15	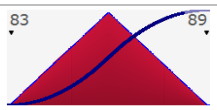	83.1	86.0	88.9	84.0	88.0	0
MC R5/6 / dip distribution	U15	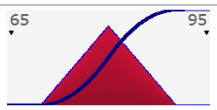	70.0	80.0	90.0	73.2	86.8	0
MC R5/6 / min	B15	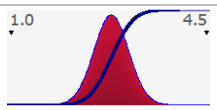	1.5	2.8	4.2	2.3	3.3	0
MC R5/6 / age	C15	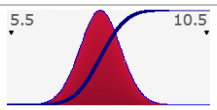	5.7	7.8	10.0	7.0	8.6	0
MC R5/6 / max	D15	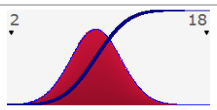	2.5	9.0	17.7	5.7	12.3	0
MC R5/6 / distribution	E15	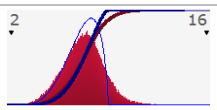	2.7	7.3	14.5	5.0	9.5	27909
MC R6/8 / SS distribution	I16	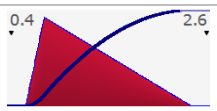	0.6	1.3	2.4	0.7	2.0	0
MC R6/8 / VD distribution	M16	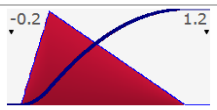	-0.1	0.3	1.0	0.0	0.8	0
MC R6/8 / strike distribution	Q16	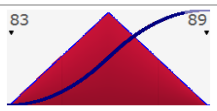	83.1	86.0	88.9	84.0	88.0	0

MC R6/8 / dip distribution	U16	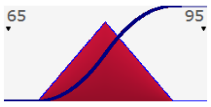	70.0	80.0	90.0	73.2	86.8	0
MC R6/8 / min	B16	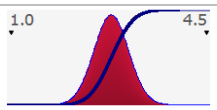	1.4	2.8	4.1	2.3	3.3	0
MC R6/8 / max	D16	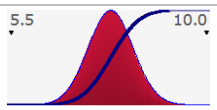	5.6	7.8	10.0	7.0	8.6	0
MC R6/8 / distribution	E16	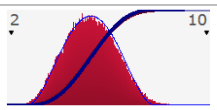	2.1	5.3	9.0	3.7	7.0	0
MC5t / min	B14	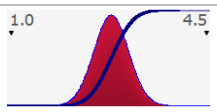	1.4	2.8	4.1	2.3	3.3	0
MC5t / age	C14	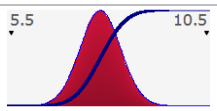	5.6	7.8	10.2	7.0	8.6	0
MC5t / max	D14	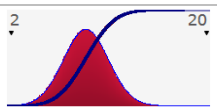	2.5	9.0	18.1	5.7	12.3	0
MC5t / distribution	E14	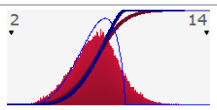	2.7	7.3	13.7	5.0	9.5	27907
MC5t / SS distribution	I14	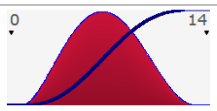	1.1	6.7	12.9	3.1	10.5	0
MC5t / VD distribution	M14	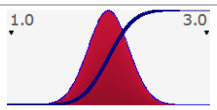	1.1	2.0	2.9	1.7	2.3	0
MC5t / strike distribution	Q14	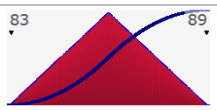	83.1	86.0	88.9	84.0	88.0	0
MC5t / dip distribution	U14	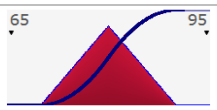	70.0	80.0	90.0	73.2	86.8	0
SHa NNE fault / min	B11	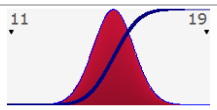	11.8	15.2	19.0	13.9	16.5	0
SHa NNE fault / max	D11	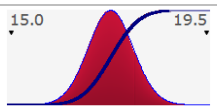	15.1	17.3	19.5	16.5	18.1	0

SHa NNE fault / distribution	E11	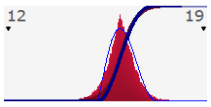	12.6	16.0	18.4	15.3	16.8	16259
SHa NNE fault / SS distribution	I11	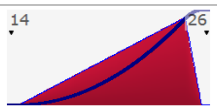	14.7	21.6	25.5	17.0	24.8	0
SHa NNE fault / VD distribution	M11	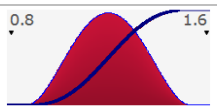	0.9	1.2	1.5	1.0	1.4	0
SHa NNE fault / strike distribution	Q11	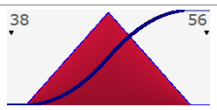	39.7	47.0	54.3	42.0	52.0	0
SHa NNE fault / dip distribution	U11	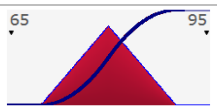	70.0	80.0	90.0	73.2	86.8	0
SHb EW fault / min	B12	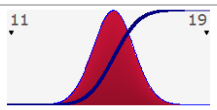	11.7	15.2	18.9	13.9	16.5	0
SHb EW fault / max	D12	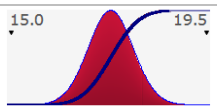	15.1	17.3	19.4	16.5	18.1	0
SHb EW fault / distribution	E12	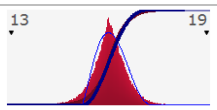	13.6	16.0	18.6	15.2	16.8	16259
SHb EW fault / SS distribution	I12	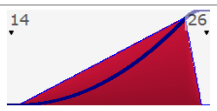	14.7	21.6	25.5	17.0	24.8	0
SHb EW fault / VD distribution	M12	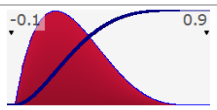	-0.1	0.2	0.8	0.0	0.5	0
SHb EW fault / strike distribution	Q12	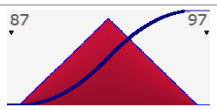	87.6	92.0	96.4	89.0	95.0	0
Styx / min	B18	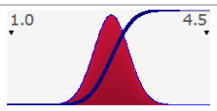	1.5	2.8	4.2	2.3	3.3	0
Styx / max	D18	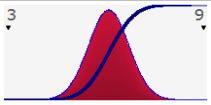	3.5	6.1	8.7	5.1	7.1	0
Styx / distribution	E18	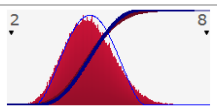	2.2	4.4	7.5	3.3	5.7	0

Styx / VD distribution	M18	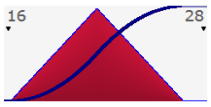	16.4	21.5	26.6	18.0	25.0	0
Yeo R3/4 / age min	B10	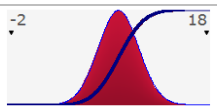	-1.0	9.0	17.7	5.7	12.3	0
Yeo R3/4 / age pref	C10	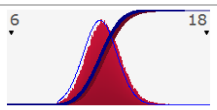	7.5	11.8	17.8	10.1	13.5	0
Yeo R3/4 / age max	D10	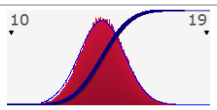	10.5	14.3	18.6	12.7	15.9	0
Yeo R3/4 / age distribution	E10	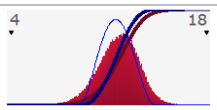	4.2	11.7	17.8	9.4	13.8	0
Yeo R3/4 / SS distribution	I10	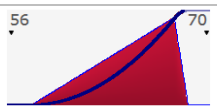	57.7	64.6	68.5	60.0	67.8	0
Yeo R3/4 / VD distribution	M10	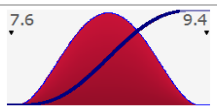	7.7	8.5	9.3	8.0	9.0	0
Yeo R3/4 / strike distribution	Q10	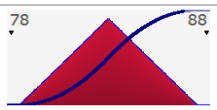	78.6	83.0	87.4	80.0	86.0	0
Yeo R3/4 / dip distribution	U10	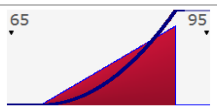	70.1	83.3	90.0	74.5	89.5	0

@RISK Output Results

Performed By: Jessie Vermeer
Date: Sunday, 30 January 2022 2:17:03 PM

Name	Cell	Graph	Min	Mean	Max	5%	95%	Errors
KF1a / Strike-Slip Rate	W6		4.1	6.4	17.9	5.0	8.1	0
KF1b / Strike-Slip Rate	W7		2.1	3.7	11.3	2.8	4.9	0
KF3 / Strike-Slip Rate	W8	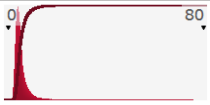	3.2	6.6	75.0	4.2	11.0	4888
KF2 / Strike-Slip Rate	W9	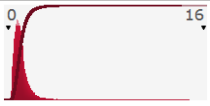	0.4	1.3	14.7	0.7	2.3	4901
Yeo R3/4 / Strike-Slip Rate	W10		3.4	5.6	14.7	4.6	7.0	0
SHa NNE fault / Strike-Slip Rate	W11	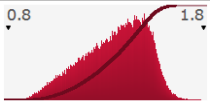	0.9	1.3	1.8	1.1	1.6	16257
SHb EW fault / Strike-Slip Rate	W12	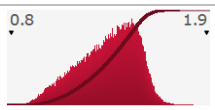	0.9	1.3	1.8	1.1	1.6	16263
MC R4/5 / Strike-Slip Rate	W13	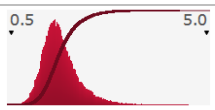	0.6	1.7	4.5	1.1	2.4	27873
MC5t / Strike-Slip Rate	W14	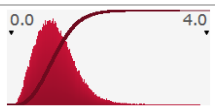	0.1	1.0	3.8	0.4	1.7	28022
MC R5/6 / Strike-Slip Rate	W15		0.3	1.2	4.0	0.7	1.9	27997
MC R6/8 / Strike-Slip Rate	W16		0.1	0.2	1.0	0.1	0.4	0
Styx / Strike-Slip Rate	W17		0.0	0.0	0.0	0.0	0.0	0

KF1a / dip-slip displacement	AB6	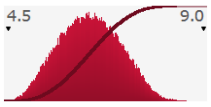	4.6	6.4	8.6	5.3	7.5	0
KF1b / dip-slip displacement	AB7	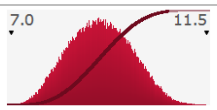	7.1	9.1	11.4	8.0	10.2	0
KF3 / dip-slip displacement	AB8	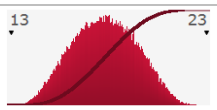	13.6	17.8	22.4	15.3	20.4	0
KF2 / dip-slip displacement	AB9	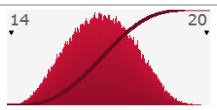	14.2	16.8	19.8	15.2	18.4	0
Yeo R3/4 / dip-slip displacement	AB10	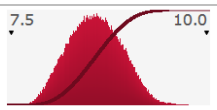	7.7	8.6	9.7	8.1	9.1	0
SHa NNE fault / dip-slip displacement	AB11	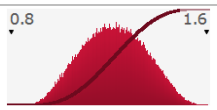	0.9	1.2	1.6	1.0	1.4	0
SHb EW fault / dip-slip displacement	AB12	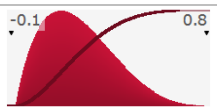	-0.1	0.2	0.8	0.0	0.5	0
MC R4/5 / dip-slip displacement	AB13	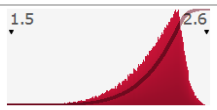	1.6	2.3	2.6	2.0	2.5	0
MC5t / dip-slip displacement	AB14	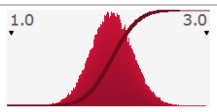	1.2	2.0	3.0	1.7	2.4	0
MC R5/6 / dip-slip displacement	AB15	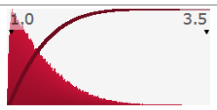	1.0	1.4	3.2	1.0	2.0	0
MC R6/8 / dip-slip displacement	AB16	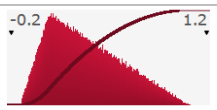	-0.1	0.3	1.1	0.0	0.8	0
Styx / dip-slip displacement	AB17	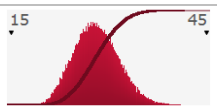	19.3	28.2	40.8	23.1	33.8	0
KF1a / Dip-Slip Rate	AC6		0.3	0.4	1.2	0.3	0.6	0
KF1b / Dip-Slip Rate	AC7		0.4	0.6	1.8	0.5	0.8	0
KF3 / Dip-Slip Rate	AC8		0.8	1.5	18.7	1.0	2.4	4888

KF2 / Dip-Slip Rate	AC9	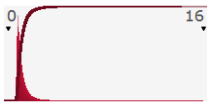	0.8	1.4	15.8	1.0	2.3	4901
Yeo R3/4 / Dip-Slip Rate	AC10		0.5	0.7	2.0	0.6	0.9	0
SHa NNE fault / Dip-Slip Rate	AC11	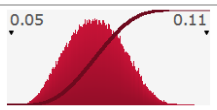	0.1	0.1	0.1	0.1	0.1	16257
SHb EW fault / Dip-Slip Rate	AC12	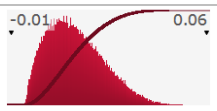	0.0	0.0	0.1	0.0	0.0	16263
MC R4/5 / Dip-Slip Rate	AC13		0.1	0.3	0.9	0.2	0.5	27873
MC5t / Dip-Slip Rate	AC14		0.1	0.3	1.0	0.2	0.4	28022
MC R5/6 / Dip-Slip Rate	AC15		0.1	0.2	0.9	0.1	0.3	27997
MC R6/8 / Dip-Slip Rate	AC16	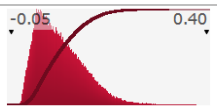	0.0	0.1	0.4	0.0	0.2	0
Styx / Dip-Slip Rate	AC17	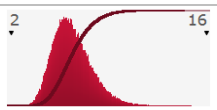	2.9	6.5	14.8	4.6	8.9	0
KF1a / horizontal shortening	AH6	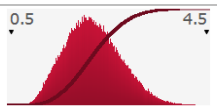	0.9	2.2	4.2	1.4	3.1	0
KF1b / horizontal shortening	AH7	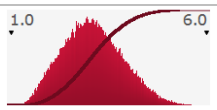	1.3	3.1	5.6	2.0	4.4	0
KF3 / horizontal shortening	AH8	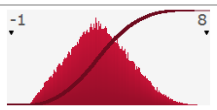	0.0	3.1	7.5	1.0	5.4	0
KF2 / horizontal shortening	AH9	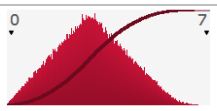	0.0	2.9	6.6	0.9	5.0	0
Yeo R3/4 / horizontal shortening	AH10	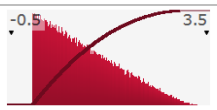	0.0	1.0	3.3	0.1	2.4	0
SHa NNE fault / horizontal shortening	AH11	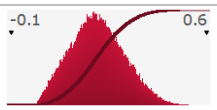	0.0	0.2	0.5	0.1	0.4	0

SHb EW fault / horizontal shortening	AH12	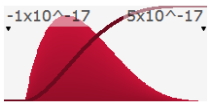	0.0	0.0	0.0	0.0	0.0	0
MC R4/5 / horizontal shortening	AH13	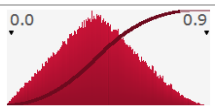	0.0	0.4	0.9	0.1	0.7	0
MC5t / horizontal shortening	AH14	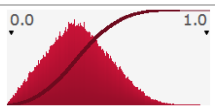	0.0	0.4	1.0	0.1	0.6	0
MC R5/6 / horizontal shortening	AH15	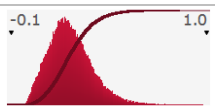	0.0	0.2	1.0	0.1	0.5	0
MC R6/8 / horizontal shortening	AH16		0.0	0.1	0.4	0.0	0.2	0
Styx / horizontal shortening	AH17	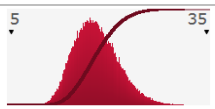	9.7	18.2	31.2	13.4	23.9	0
KF1a / net slip	AI6	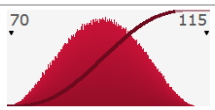	70.7	91.2	111.7	78.3	104.2	0
KF1b / net slip	AI7	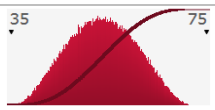	36.5	53.8	71.0	43.0	64.7	0
KF3 / net slip	AI8	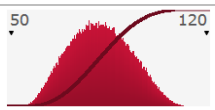	56.4	82.2	111.2	65.5	99.6	0
KF2 / net slip	AI9	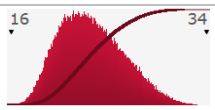	16.6	23.5	33.0	19.3	28.6	0
Yeo R3/4 / net slip	AI10	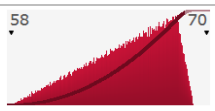	58.3	65.2	69.1	60.6	68.3	0
SHa NNE fault / net slip	AI11		14.8	21.6	25.5	17.0	24.8	0
SHb EW fault / net slip	AI12		14.7	21.6	25.5	17.0	24.8	0
MC R4/5 / net slip	AI13	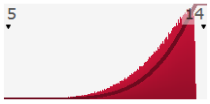	6.0	12.0	13.6	9.7	13.4	0
MC5t / net slip	AI14	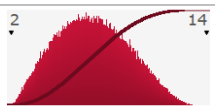	2.1	7.1	13.0	3.7	10.7	0

MC R5/6 / net slip	AI15	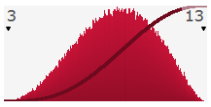	3.2	8.6	12.9	5.4	11.5	0
MC R6/8 / net slip	AI16	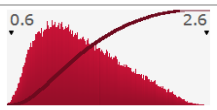	0.6	1.3	2.5	0.8	2.1	0
Styx / net slip	AI17	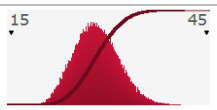	19.3	28.2	40.8	23.1	33.8	0
KF1a / slip rate (mean)	AK6		4.1	6.4	18.0	5.0	8.2	0
KF1b / slip rate (mean)	AK7		2.2	3.8	11.4	2.8	4.9	0
KF3 / slip rate (mean)	AK8	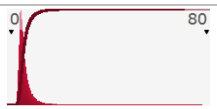	3.3	6.8	77.2	4.4	11.3	4888
KF2 / slip rate (mean)	AK9		1.0	1.9	21.4	1.3	3.2	4901
Yeo R3/4 / slip rate (mean)	AK10		3.5	5.6	14.8	4.6	7.0	0
SHa NNE fault / slip rate (mean)	AK11	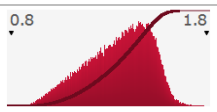	0.9	1.3	1.8	1.1	1.6	16257
SHb EW fault / slip rate (mean)	AK12	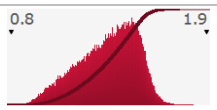	0.9	1.3	1.8	1.1	1.6	16263
MC R4/5 / slip rate (mean)	AK13	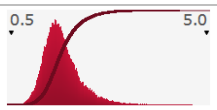	0.6	1.7	4.6	1.2	2.5	27873
MC5t / slip rate (mean)	AK14	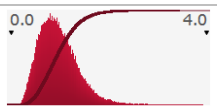	0.2	1.0	3.9	0.5	1.7	28022
MC R5/6 / slip rate (mean)	AK15	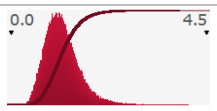	0.3	1.2	4.0	0.7	1.9	27997
MC R6/8 / slip rate (mean)	AK16		0.1	0.3	1.0	0.1	0.4	0
Styx / slip rate (mean)	AK17	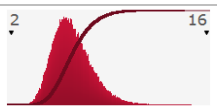	2.9	6.5	14.8	4.6	8.9	0

KF1a / HSV degree	AQ6	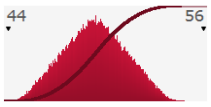	44.5	49.4	54.7	46.3	52.4	0
KF1b / HSV degree	AQ7	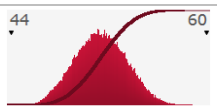	45.0	51.4	58.7	48.1	54.7	0
KF3 / HSV degree	AQ8	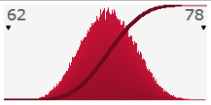	64.0	70.3	78.0	66.9	73.6	0
KF2 / HSV degree	AQ9	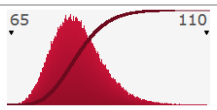	66.3	80.8	109.6	72.6	90.9	0
Yeo R3/4 / HSV degree	AQ10	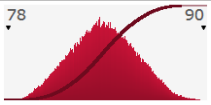	78.7	83.9	89.6	80.7	87.0	0
SHa NNE fault / HSV degree	AQ11	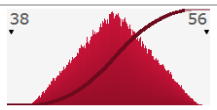	39.8	47.6	55.4	42.6	52.6	0
SHb EW fault / HSV degree	AQ12	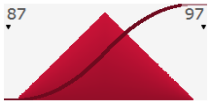	87.6	92.0	96.4	89.0	95.0	0
MC R4/5 / HSV degree	AQ13	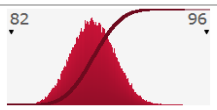	83.3	88.0	94.2	85.6	90.4	0
MC5t / HSV degree	AQ14		83.3	89.5	114.3	86.1	94.0	0
MC R5/6 / HSV degree	AQ15	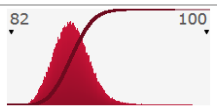	83.2	87.8	98.5	85.3	90.4	0
MC R6/8 / HSV degree	AQ16		82.2	89.0	112.8	85.0	95.1	0
Styx / HSV degree	AQ17					n/a	n/a	100000
KF1a / HSV length	AT6		4.4	6.8	18.1	5.5	8.5	0
KF1b / HSV length	AT7		2.7	4.9	12.2	3.8	6.1	0
KF3 / HSV length	AT8		3.5	7.6	77.2	5.1	11.8	4888

KF2 / HSV length	AT9		1.1	3.6	21.7	1.9	5.6	4901
Yeo R3/4 / HSV length	AT10	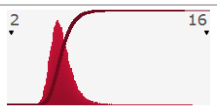	3.6	5.8	14.8	4.8	7.1	0
SHa NNE fault / HSV length	AT11	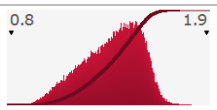	0.9	1.4	1.8	1.1	1.6	16257
SHb EW fault / HSV length	AT12	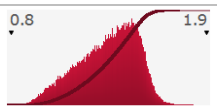	0.9	1.3	1.8	1.1	1.6	16263
MC R4/5 / HSV length	AT13	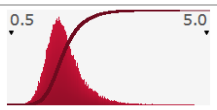	0.7	1.8	4.7	1.2	2.5	27873
MC5t / HSV length	AT14	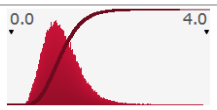	0.2	1.1	3.9	0.6	1.7	28022
MC R5/6 / HSV length	AT15	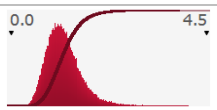	0.4	1.3	4.0	0.7	1.9	27997
MC R6/8 / HSV length	AT16		0.1	0.3	1.0	0.1	0.5	0
Styx / HSV length	AT17	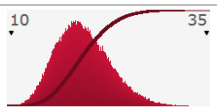	10.3	19.4	32.4	14.4	25.2	0
KF1a / Strike-Slip Rate	W6		4.0	6.4	19.3	5.0	8.2	0
KF1b / Strike-Slip Rate	W7	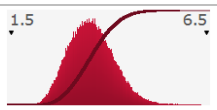	2.0	3.6	6.3	2.7	4.5	0
KF3 / Strike-Slip Rate	W8	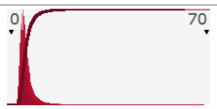	3.0	6.6	68.2	4.2	11.0	4931
KF2 / Strike-Slip Rate	W9		0.4	1.3	27.6	0.7	2.3	4965
Yeo R3/4 / Strike-Slip Rate	W10		3.4	5.6	14.6	4.6	7.0	0

SHa NNE fault / Strike-Slip Rate	W11	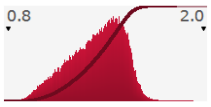	0.9	1.3	1.9	1.1	1.6	16259
SHb EW fault / Strike-Slip Rate	W12	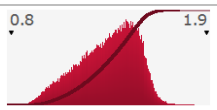	0.9	1.3	1.8	1.1	1.6	16259
MC R4/5 / Strike-Slip Rate	W13	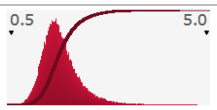	0.7	1.7	4.7	1.1	2.4	27874
MC5t / Strike-Slip Rate	W14	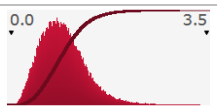	0.1	1.0	3.4	0.4	1.7	27907
MC R5/6 / Strike-Slip Rate	W15		0.3	1.2	4.2	0.7	1.9	27909
MC R6/8 / Strike-Slip Rate	W16		0.1	0.2	1.0	0.1	0.4	0
Styx / Strike-Slip Rate	W18		0.0	0.0	0.0	0.0	0.0	0
KF1a (older min age) / Strike-Slip Rate	W19	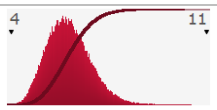	4.1	6.1	10.4	5.0	7.4	0
J82 upper fan / Strike-Slip Rate	W20		3.5	5.6	16.0	4.6	7.0	0
J82 upper fan / Strike-Slip Rate	W21		3.4	5.6	15.2	4.6	7.0	0
KF1a / dip-slip displacement	AB6	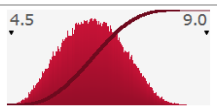	4.5	6.4	8.5	5.3	7.5	0
KF1b / dip-slip displacement	AB7	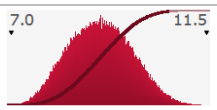	7.1	9.1	11.3	8.0	10.2	0
KF3 / dip-slip displacement	AB8	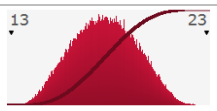	13.6	17.8	22.3	15.2	20.4	0
KF2 / dip-slip displacement	AB9	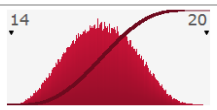	14.2	16.8	19.8	15.2	18.4	0
Yeo R3/4 / dip-slip displacement	AB10	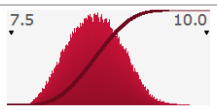	7.7	8.6	9.8	8.1	9.1	0

SHa NNE fault / dip-slip displacement	AB11	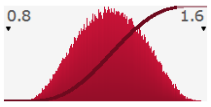	0.9	1.2	1.6	1.0	1.4	0
SHb EW fault / dip-slip displacement	AB12	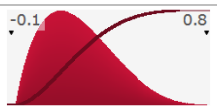	-0.1	0.2	0.8	0.0	0.5	0
MC R4/5 / dip-slip displacement	AB13	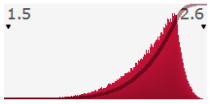	1.6	2.3	2.6	2.0	2.5	0
MC5t / dip-slip displacement	AB14	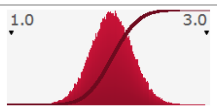	1.1	2.0	3.0	1.7	2.4	0
MC R5/6 / dip-slip displacement	AB15		1.0	1.4	3.1	1.0	2.0	0
MC R6/8 / dip-slip displacement	AB16	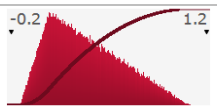	-0.1	0.3	1.1	0.0	0.8	0
Styx / dip-slip displacement	AB18	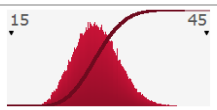	19.2	28.2	40.2	23.1	33.8	0
KF1a (older min age) / dip-slip displacement	AB19	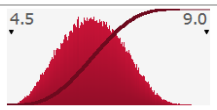	4.6	6.4	8.6	5.3	7.5	0
J82 upper fan / dip-slip displacement	AB20	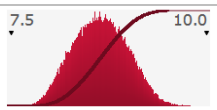	7.7	8.7	9.8	8.1	9.2	0
J82 upper fan / dip-slip displacement	AB21	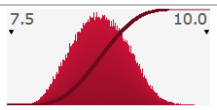	7.7	8.7	9.8	8.1	9.2	0
KF1a / Dip-Slip Rate	AC6		0.3	0.4	1.4	0.3	0.6	0
KF1b / Dip-Slip Rate	AC7	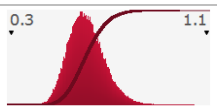	0.4	0.6	1.0	0.5	0.7	0
KF3 / Dip-Slip Rate	AC8		0.8	1.5	19.1	1.0	2.4	4931
KF2 / Dip-Slip Rate	AC9		0.8	1.4	21.6	1.0	2.3	4965
Yeo R3/4 / Dip-Slip Rate	AC10		0.5	0.7	2.0	0.6	0.9	0

SHa NNE fault / Dip-Slip Rate	AC11	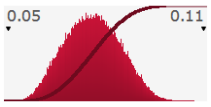	0.1	0.1	0.1	0.1	0.1	16259
SHb EW fault / Dip-Slip Rate	AC12	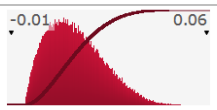	0.0	0.0	0.1	0.0	0.0	16259
MC R4/5 / Dip-Slip Rate	AC13	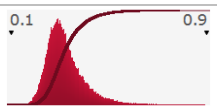	0.2	0.3	0.9	0.2	0.5	27874
MC5t / Dip-Slip Rate	AC14	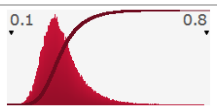	0.1	0.3	0.8	0.2	0.4	27907
MC R5/6 / Dip-Slip Rate	AC15		0.1	0.2	0.7	0.1	0.3	27909
MC R6/8 / Dip-Slip Rate	AC16	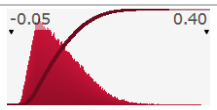	0.0	0.1	0.4	0.0	0.2	0
Styx / Dip-Slip Rate	AC18		3.0	6.5	14.8	4.6	8.9	0
KF1a (older min age) / Dip-Slip Rate	AC19	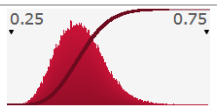	0.3	0.4	0.7	0.3	0.5	0
J82 upper fan / Dip-Slip Rate	AC20		0.5	0.7	2.0	0.6	0.9	0
J82 upper fan / Dip-Slip Rate	AC21		0.5	0.7	2.0	0.6	0.9	0
KF1a / horizontal shortening	AH6	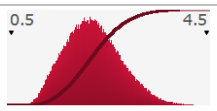	0.8	2.2	4.2	1.4	3.1	0
KF1b / horizontal shortening	AH7	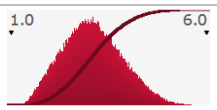	1.3	3.1	5.6	2.0	4.4	0
KF3 / horizontal shortening	AH8	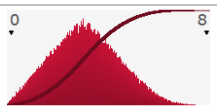	0.0	3.1	7.5	1.0	5.4	0
KF2 / horizontal shortening	AH9	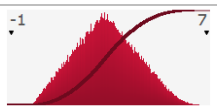	0.0	2.9	6.6	0.9	5.0	0
Yeo R3/4 / horizontal shortening	AH10	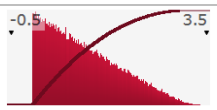	0.0	1.0	3.3	0.1	2.4	0

SHa NNE fault / horizontal shortening	AH11	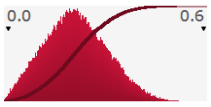	0.0	0.2	0.5	0.1	0.4	0
SHb EW fault / horizontal shortening	AH12	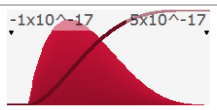	0.0	0.0	0.0	0.0	0.0	0
MC R4/5 / horizontal shortening	AH13	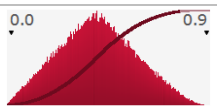	0.0	0.4	0.9	0.1	0.7	0
MC5t / horizontal shortening	AH14	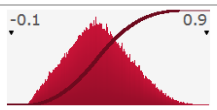	0.0	0.4	0.9	0.1	0.6	0
MC R5/6 / horizontal shortening	AH15		0.0	0.2	1.0	0.1	0.5	0
MC R6/8 / horizontal shortening	AH16	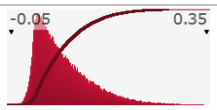	0.0	0.1	0.3	0.0	0.2	0
Styx / horizontal shortening	AH18	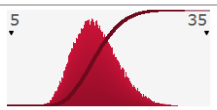	9.8	18.2	30.5	13.4	23.9	0
KF1a (older min age) / horizontal shortening	AH19	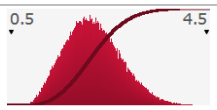	0.8	2.2	4.2	1.4	3.1	0
J82 upper fan / horizontal shortening	AH20	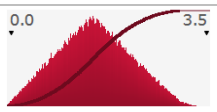	0.0	1.5	3.3	0.5	2.6	0
J82 upper fan / horizontal shortening	AH21	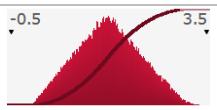	0.0	1.5	3.3	0.5	2.6	0
KF1a / net slip	AI6	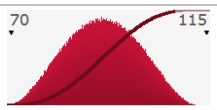	70.7	91.2	112.0	78.3	104.2	0
KF1b / net slip	AI7	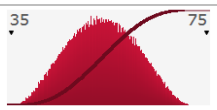	36.4	53.8	71.0	43.0	64.6	0
KF3 / net slip	AI8	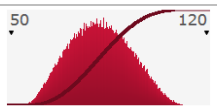	56.5	82.2	111.0	65.5	99.6	0
KF2 / net slip	AI9	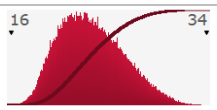	16.5	23.5	33.3	19.3	28.6	0
Yeo R3/4 / net slip	AI10	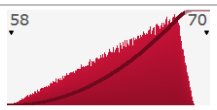	58.3	65.2	69.1	60.6	68.3	0

SHa NNE fault / net slip	AI11	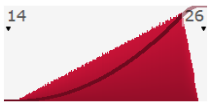	14.8	21.6	25.5	17.0	24.8	0
SHb EW fault / net slip	AI12		14.7	21.6	25.5	17.0	24.8	0
MC R4/5 / net slip	AI13	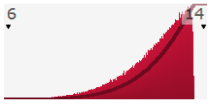	6.0	12.0	13.5	9.7	13.4	0
MC5t / net slip	AI14	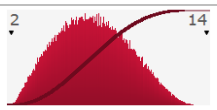	2.1	7.1	13.1	3.7	10.7	0
MC R5/6 / net slip	AI15	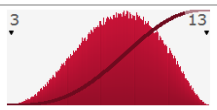	3.1	8.6	13.0	5.4	11.5	0
MC R6/8 / net slip	AI16	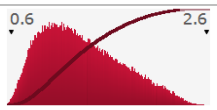	0.6	1.3	2.6	0.8	2.1	0
Styx / net slip	AI18	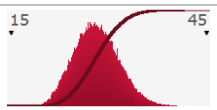	19.2	28.2	40.2	23.1	33.8	0
KF1a (older min age) / net slip	AI19		70.7	91.2	112.0	78.3	104.2	0
J82 upper fan / net slip	AI20	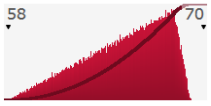	58.3	65.2	69.1	60.6	68.4	0
J82 upper fan / net slip	AI21	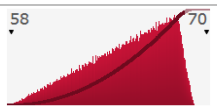	58.3	65.2	69.1	60.6	68.3	0
KF1a / slip rate (mean)	AK6		4.0	6.4	19.3	5.0	8.2	0
KF1b / slip rate (mean)	AK7	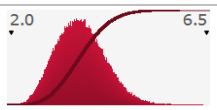	2.0	3.6	6.4	2.8	4.6	0
KF3 / slip rate (mean)	AK8		3.2	6.8	70.2	4.4	11.2	4931
KF2 / slip rate (mean)	AK9		1.0	1.9	35.0	1.3	3.2	4965
Yeo R3/4 / slip rate (mean)	AK10	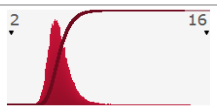	3.5	5.6	14.7	4.6	7.0	0

SHa NNE fault / slip rate (mean)	AK11	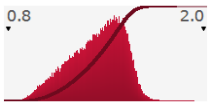	0.9	1.3	1.9	1.1	1.6	16259
SHb EW fault / slip rate (mean)	AK12	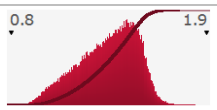	0.9	1.3	1.8	1.1	1.6	16259
MC R4/5 / slip rate (mean)	AK13	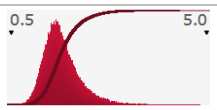	0.7	1.7	4.8	1.2	2.5	27874
MC5t / slip rate (mean)	AK14	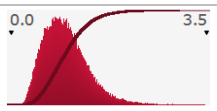	0.2	1.0	3.4	0.5	1.7	27907
MC R5/6 / slip rate (mean)	AK15		0.3	1.2	4.3	0.7	1.9	27909
MC R6/8 / slip rate (mean)	AK16		0.1	0.3	1.0	0.1	0.4	0
Styx / slip rate (mean)	AK18	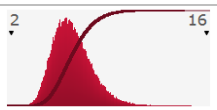	3.0	6.5	14.8	4.6	8.9	0
KF1a (older min age) / slip rate (mean)	AK19	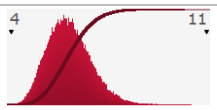	4.1	6.1	10.4	5.0	7.5	0
J82 upper fan / slip rate (mean)	AK20		3.5	5.6	16.1	4.6	7.0	0
J82 upper fan / slip rate (mean)	AK21		3.4	5.6	15.3	4.6	7.0	0
KF1a / HSV degree	AQ6	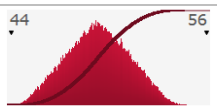	44.4	49.4	54.7	46.3	52.4	0
KF1b / HSV degree	AQ7	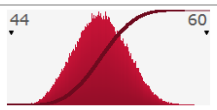	45.2	51.4	58.8	48.1	54.7	0
KF3 / HSV degree	AQ8	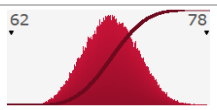	63.9	70.3	77.9	66.9	73.7	0
KF2 / HSV degree	AQ9	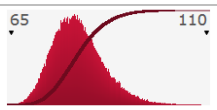	66.2	80.8	108.2	72.6	90.9	0
Yeo R3/4 / HSV degree	AQ10	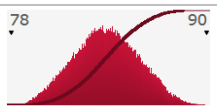	78.7	83.9	89.7	80.7	87.0	0

SHa NNE fault / HSV degree	AQ11	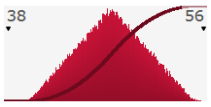	40.0	47.6	55.6	42.6	52.6	0
SHb EW fault / HSV degree	AQ12	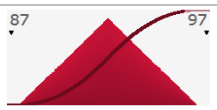	87.6	92.0	96.4	89.0	95.0	0
MC R4/5 / HSV degree	AQ13	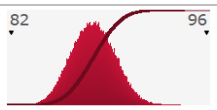	83.3	88.0	94.1	85.6	90.4	0
MC5t / HSV degree	AQ14	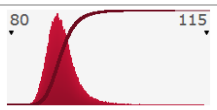	83.5	89.5	114.2	86.1	94.0	0
MC R5/6 / HSV degree	AQ15	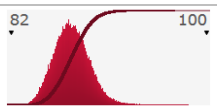	83.3	87.8	98.2	85.3	90.4	0
MC R6/8 / HSV degree	AQ16		81.9	89.0	110.6	85.1	95.1	0
Styx / HSV degree	AQ18					n/a	n/a	100000
KF1a (older min age) / HSV degree	AQ19	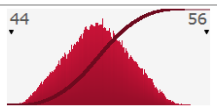	44.3	49.4	54.9	46.3	52.4	0
J82 upper fan / HSV degree	AQ20	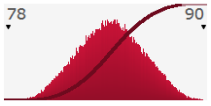	78.9	84.3	89.9	81.2	87.5	0
J82 upper fan / HSV degree	AQ21	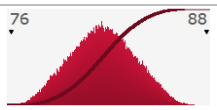	76.1	81.7	87.1	78.5	84.8	0
KF1a / HSV length	AT6		4.4	6.8	19.4	5.5	8.5	0
KF1b / HSV length	AT7	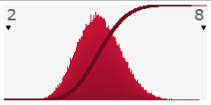	2.8	4.8	7.8	3.8	5.9	0
KF3 / HSV length	AT8		3.5	7.6	70.3	5.1	11.8	4931
KF2 / HSV length	AT9		1.0	3.6	35.2	1.9	5.6	4965
Yeo R3/4 / HSV length	AT10		3.5	5.8	14.7	4.8	7.1	0

SHa NNE fault / HSV length	AT11	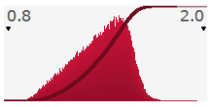	0.9	1.4	2.0	1.1	1.6	16259
SHb EW fault / HSV length	AT12	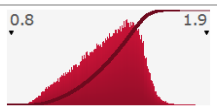	0.9	1.3	1.8	1.1	1.6	16259
MC R4/5 / HSV length	AT13	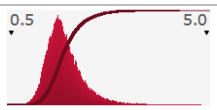	0.7	1.8	4.8	1.2	2.5	27874
MC5t / HSV length	AT14	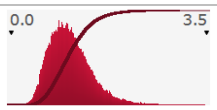	0.2	1.1	3.4	0.6	1.7	27907
MC R5/6 / HSV length	AT15	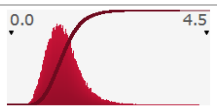	0.4	1.3	4.3	0.7	1.9	27909
MC R6/8 / HSV length	AT16		0.1	0.3	1.0	0.1	0.5	0
Styx / HSV length	AT18	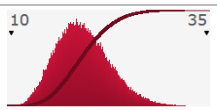	10.6	19.4	32.2	14.4	25.1	0
KF1a (older min age) / HSV length	AT19	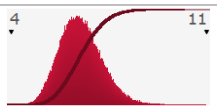	4.4	6.6	10.9	5.4	7.8	0
J82 upper fan / HSV length	AT20		3.7	5.9	16.1	4.9	7.2	0
J82 upper fan / HSV length	AT21		3.5	5.9	15.4	4.9	7.2	0

Appendix B

Radiocarbon sample information and additional reconnaissance samples:

Table A3B.1. Sample location and notes:

waypoint	sample type	notes	date	lat	long
J23	C14	peat above likely colluvial wedge. sampled 80cm bgs in bog.	24-011-17	-42.7579	171.758
J75	C14	Peat sampled in bog 40cm bgs, immediately above basal gravels (at least 20cm thick gravels, assumed to be terrace top)	04-012-17	-42.7485	171.796
J78A	C14	Peat samples from two pits (A and C). In pit A we sampled at 40, 38, and 20 cm bgs (peat base at 40cm, blue/gray clay underlies peat.) in pit B, sampled at 20cm bgs, at the base of the peat/clay interface.	05-012-17	-42.75	171.809
J84	C14	Peat from the base of the scarp bounded bog. Two samples of the peat, J84A2 is the preferred sample.	06-012-17	-42.7428	171.834
J78C	C14	Peat samples from two pits (A and C). In pit A we sampled at 40, 38, and 20 cm bgs (peat base at 40cm, blue/gray clay underlies peat.) in pit B, sampled at 20cm bgs, at the base of the peat/clay interface.	05-012-17	-42.75	171.809
1370C	C14	bulk material sample of possible paleosol development in faulted silty layer. Syndepositional organics will be a max age for the MRE.	2019	-42.8879	171.148
J134A	C14	bulk material sample of grey silt for C14 picking. Organics would be older than the MRE, and possibly	2019	-42.7579	171.758

		previous events (number of ruptures "seen" by the silt in unknown)			
J134D	C14	bulk material sample of the colluvium. Organics within this unit would be around the age of the MRE.	2019	-42.7579	171.758

Bgs = below ground surface

Figure A3B.1. Sampling pit logs

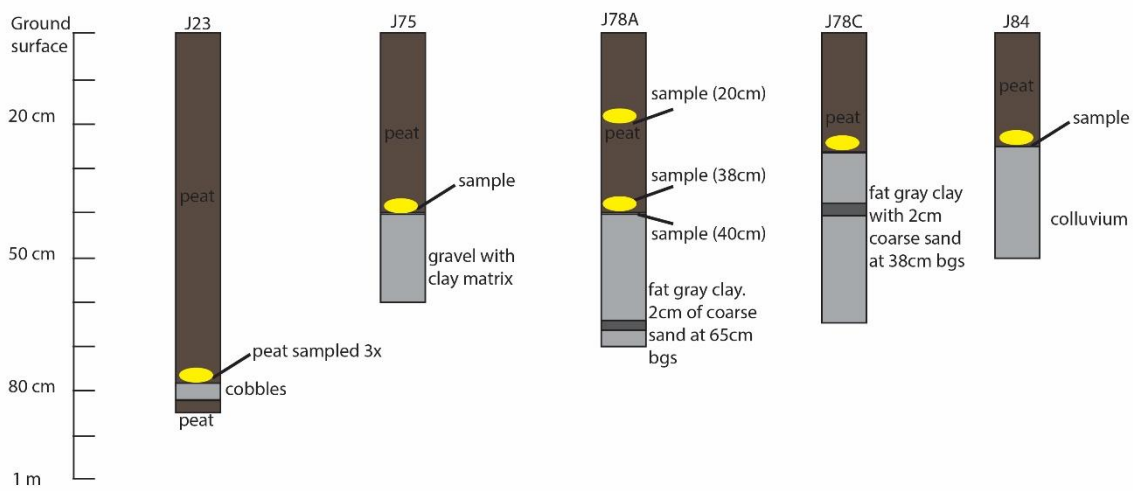

Table A3B.2. 14C dating analysis results

Date reported	Client name	TW	Date analysed	Sample ID	Description	Fraction dated	Rafter ID	NZA	CRA	CRA error	$\delta^{13}C$	$\delta^{13}C$ error	$\delta^{13}C$ source	F	F error	$\Delta^{14}C$	$\Delta^{14}C$ error
									[yBP]		[‰]			[ ]		[‰]	
22-08-2019	Jessie Vermeer	3245	3-08-2019	J134A	flakes of possible bark	Plant Material	41336/1	68075	242	19	-29.27	0.2	IRMS	0.970284	0.002395		
22-08-2019	Jessie Vermeer	3245	3-08-2019	J134D	stem/twig or possible root with bark	Plant Material	41336/2	68076	Modern		-29.34	0.2	IRMS	1.191293	0.002804		
22-08-2019	Jessie Vermeer	3245	3-08-2019	J1370C	thin twig, possible root	Plant Material	41336/3	68077	225	19	-28.63	0.2	IRMS	0.972291	0.002386		
22-08-2019	Jessie Vermeer	3247	16-08-2019	J1277 gs	twig (possibly monocot) or root	Plant Material	41336/4	68148	Modern		-28.44	0.2	IRMS	1.162407	0.002907		
22-08-2019	Jessie Vermeer	3247	16-08-2019	J1277TC	twig (reed?) or root	Plant Material	41336/5	68149	Modern		-26.68	0.2	IRMS	1.307053	0.003189		
22-08-2019	Jessie Vermeer	3247	16-08-2019	J1277RG	4 twigs (reed?) or roots	Plant Material	41336/6	68150	12	20	-27.01	0.2	IRMS	0.998484	0.002573		
25-06-2018	Jessie Vermeer	3171	21-06-2018	J23A-L	large leaf fragment	Plant material	41177/2	65213	Modern		-33.38	0.2	IRMS	1.028991	0.002667	28.99	2.67
25-06-2018	Jessie Vermeer	3171	21-06-2018	J75-L	leaf skeletons	Plant material	41177/4	65214	209	21	-28.48	0.2	IRMS	0.974329	0.00256	-25.67	2.56
25-06-2018	Jessie Vermeer	3171	21-06-2018	J78A65	small organic fragments	Plant material	41177/6	65215	168	21	-29.64	0.2	IRMS	0.979331	0.002592	-20.67	2.59

25-06-2018	Jessie Vermeer	3171	21-06-2018	J84A2	small organic fragments	Plant material	41177/8	65216	472	21	-23.25	0.2	IRMS	0.942896	0.002521	-57.1	2.52

Table A3B.3. 14C sample pre-treatment notes, same samples as Table A3B.2.

Rafter ID	Sample ID	Pretreatment description
41336/1	J134A	Description of sample when received: Multiple small flakes of likely bark (max 6mm long) were isolated. Sample prepared by: Cut/Scrape and Picking. Pretreatment description: dry picked, then washed with water and lightly scrubbed. Dried overnight. Chemical pretreatment was by acid, alkali, acid. Weight obtained after chemical pretreatment was 6.1mg. Carbon dioxide was generated by elemental analyser combustion and 0.7mgC was obtained. Sample carbon dioxide was converted to graphite by reduction with hydrogen over iron catalyst.
41336/2	J134D	Description of sample when received: A 14mm long small, possible twig, was isolated. Sample had a pithy center and poorly attached bark and could possibly be a root. Sample prepared by: Cut/Scrape. Pretreatment description: scraped sediment from surface with tweezers Chemical pretreatment was by acid, alkali, acid. Weight obtained after chemical pretreatment was 2.2mg. Carbon dioxide was generated by elemental analyser combustion and 1mgC was obtained. Sample carbon dioxide was converted to graphite by reduction with hydrogen over iron catalyst.
41336/3	J1370C	Description of sample when received: Thin twig with small offshoots, possible root fragment, was isolated. Sample prepared by: Cut/Scrape. Pretreatment description: picked sample clean with tweezers and brush once dry. Chemical pretreatment was by acid, alkali, acid. Weight obtained after chemical pretreatment was 4.2mg. Carbon dioxide was generated by elemental analyser combustion and 0.9mgC was obtained. Sample carbon dioxide was converted to graphite by reduction with hydrogen over iron catalyst.

41336/4	J1277 gs	Description of sample when received: sample was a small twig, 12mm long, with a monocot-like central structure and well attached bark. Sample prepared by: Cut/Scrape. Pretreatment description: scraped and brushed sediment off while dry. Chemical pretreatment was by acid, alkali, acid. Weight obtained after chemical pretreatment was 3.6mg. Carbon dioxide was generated by elemental analyser combustion and 1mgC was obtained. Sample carbon dioxide was converted to graphite by reduction with hydrogen over iron catalyst.
41336/5	J1277TC	Description of sample when received: sample was a small twig with offshoots. Possibly reed, with striated linear surface texture and wide tubes in the centre. Sample prepared by: Cut/Scrape. Pretreatment description: scraped and brushed sediment off while dry. Chemical pretreatment was by acid, alkali, acid. Weight obtained after chemical pretreatment was 4.1mg. Carbon dioxide was generated by elemental analyser combustion and 1mgC was obtained. Sample carbon dioxide was converted to graphite by reduction with hydrogen over iron catalyst.
41336/6	J1277RG	Description of sample when received: Samples were small twigs with a reed-like appearance (lengthways linear striated surface with thick tubes in centre). Sample prepared by: Cut/Scrape. Pretreatment description: scraped and brushed sediment off while dry. Chemical pretreatment was by acid, alkali, acid. Weight obtained after chemical pretreatment was 8.1mg. Carbon dioxide was generated by elemental analyser combustion and 1mgC was obtained. Sample carbon dioxide was converted to graphite by reduction with hydrogen over iron catalyst.
41177/2	J23A-L	29.2mg of raw sample was received. Description of sample when received: Large (1/2cm) leaf, almost completely intact, with insect eggs on the leaf surface. The leaf is mostly dark brown, but with some patches where only the skeleton is left. Sample prepared by: Cut/Scrape/Picking. Pretreatment description: Used tweezers and a paint brush to remove dirt/sediment from the surface of the leaf. Chemical pretreatment was by acid, alkali, (which was repeated), acid. Weight obtained after chemical pretreatment was 6.1mg. Carbon dioxide was generated by elemental analyser combustion and 1.2mgC was obtained. Sample carbon dioxide was converted to graphite by reduction with hydrogen over iron catalyst. Photo supplied by submitter of sample. GNS Science has verified that the measured sample was taken from the photographed object.

41177/4	J75-L	66.1 mg of raw sample was received. Description of sample when received: The sample consisted of 5+ small branching leaves on fine twigs. 10.9 mg was subsampled and prepared by: Cut/Scrape, Picking. Pre-treatment description: Sediment chunks were picked off of the leaves with tweezers. Chemical pre-treatment was by acid, alkali, acid. Weight obtained after chemical pre-treatment was 6.6 mg. Carbon dioxide was generated by elemental analyser combustion and 1 mgC was obtained. Sample carbon dioxide was converted to graphite by reduction with hydrogen over iron catalyst. Photo was supplied by the submitter of the sample. GNS Science has verified that the measured sample was taken from the photographed object.
41177/6	J78A65	81.2 mg of raw sample was received. Description of sample when received: The sample consisted of a small (1 cm x 1 mm) twig with bark. 5.4 mg was subsampled and prepared by: Cut/Scrape, Picking. Pre-treatment description: Sediment was cleaned from the surface using tweezers and a scalpel. Chemical pre-treatment was by acid, alkali, acid. Weight obtained after chemical pre-treatment was 2.9 mg. Carbon dioxide was generated by elemental analyser combustion and 0.9 mgC was obtained. Sample carbon dioxide was converted to graphite by reduction with hydrogen over iron catalyst. Photo was supplied by the submitter of the sample. GNS Science has verified that the measured sample was taken from the photographed object.
41177/8	J84A2	54.2 mg of raw sample was received. Description of sample when received: The sample consisted of many small twigs, two of which were chosen for dating. Both subsampled twigs had bark, were not roots, and appeared uncontaminated by root hairs. 3.4 mg was subsampled and prepared by: Cut/Scrape, Picking. Pre-treatment description: Sediment was picked and scraped from the surface using tweezers and a scalpel. Chemical pre-treatment was by acid, alkali, acid. Weight obtained after chemical pre-treatment was 1.6 mg. Carbon dioxide was generated by elemental analyser combustion and 0.7 mgC was obtained. Sample carbon dioxide was converted to graphite by reduction with hydrogen over iron catalyst. Photo was supplied by the submitter of the sample. GNS Science has verified that the measured sample was taken from the photographed object.

Appendix C

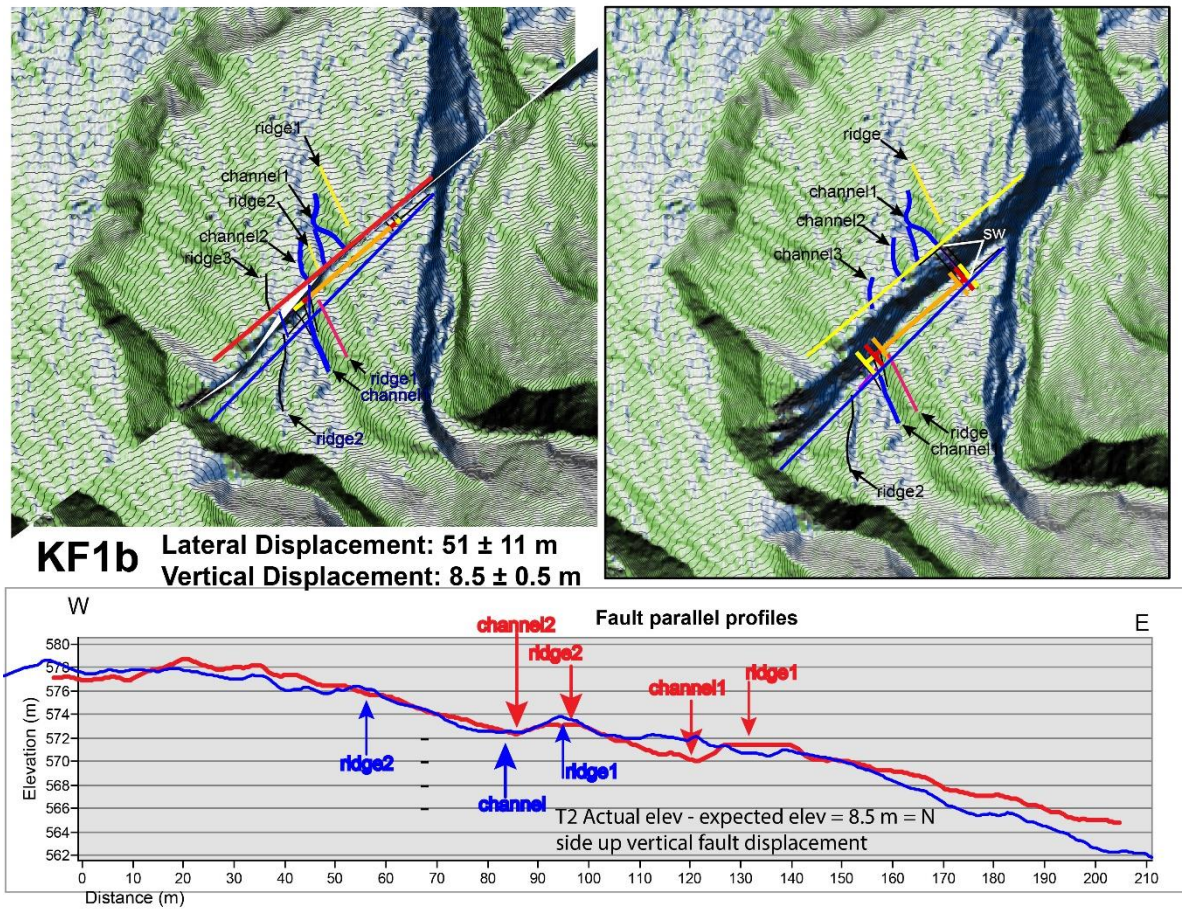

Figure C.1. Alternate displacement measurement at Site 3: Locke Stream fan.

Appendix D

Buried trees in the Deception River fan

Where the Deception River enters the Otira River valley, it has formed a wide, low profile fan which is currently mostly cattle and sheep pasture (Figure D.1). There are some remnants of the old growth forest along the active stream. South of the active stream channel, in a grassy paddock, there are many tree stumps with medium diameter (0.3-0.8 m). One of these tree stumps is along the steep bank of a small active stream, which exposes the roots and sediment (Figure D.1). The tree is rooted into fine to medium grained sediments with a faint paleosol developed (Figure A3D.1). Above the paleosol and burying the lower part of the tree stump, is ~0.8 m of fine-grained stratified sediments. We interpret these sediments as a flood deposit which buried the tree.

If the trees were killed by this burial, the outer rings of the tree would be equivalent in age to the flood deposit. This stump was too rotten to date the outer rings, but we chose another nearby stump with slightly better wood integrity, which was also buried by the flood deposit. However, the stumps have flat, apparently cut tops. We inquired with the owners and lessees of the land as to the history of the area. The fan is split in half by the Deception River, and the two halves have had different owners and lessees since the late 1800's, the Evans family have owned or leased the true-right of the river since ~1880 (personal communication with Graeme Kates via e-mail, 10 May, 2011). Between ~1900-1920, the area was logged for railway timber (personal communication with Graeme Kates via e-mail, 10 May, 2011), which is likely when the trees of interest were sawn down. The health and burial status of the trees at that time is unknown to us. However in conversations with locals, including Ed Evans

Jr. who leases the whole fan, there has been no mention of anyone remembering the flood event which deposited the 0.8 m of silt. This lack of an oral record may indicate the deposition occurred prior to European occupation here, but this is not definitive.

We dated two of the outer rings of the smaller stump located away from the stream bank, and counted 19 ± 2 rings between the dated rings. We made two separate Oxcal models to determine the death age of the tree (Figure D.2). The first OxCal model includes a constraint of tree death occuring prior to european colinization (1840); this model constrains the death age for this tree is 1762-1849 AD. This would be the minimum age for deposition of the flood deposit and likely within 0-20 years of the deposition, considering that trees can live for short times in adverse conditions (Langridge et al., 2012). However, because of the uncertainty brought by the stump being cut, we have to consider that the tree may not have been killed by the flood deposit. For this scenario the youngest limit on tree death is 1910 ± 10 years, the interval when the area was logged.

The fine-grained nature of the deposit that buried the trees indicates it is a distal, water transported deposit. It could be due to a large influx of sediment into the catchment, a large storm event which mobilized sediment, or both. Considering the wet climate, it is likely large flood events occur frequently, making the creation of new sediment a limiting factor in creating this deposit. Upstream there is a relatively young appearing landslide scar with stored sediment in the river at the base. This may have been the sediment source for the flood deposit. Since earthquakes can promote landsliding and sediment delivery and the proximity of this site to many active faults, it is possible that the sediment is sourced from co-seismic landsliding.

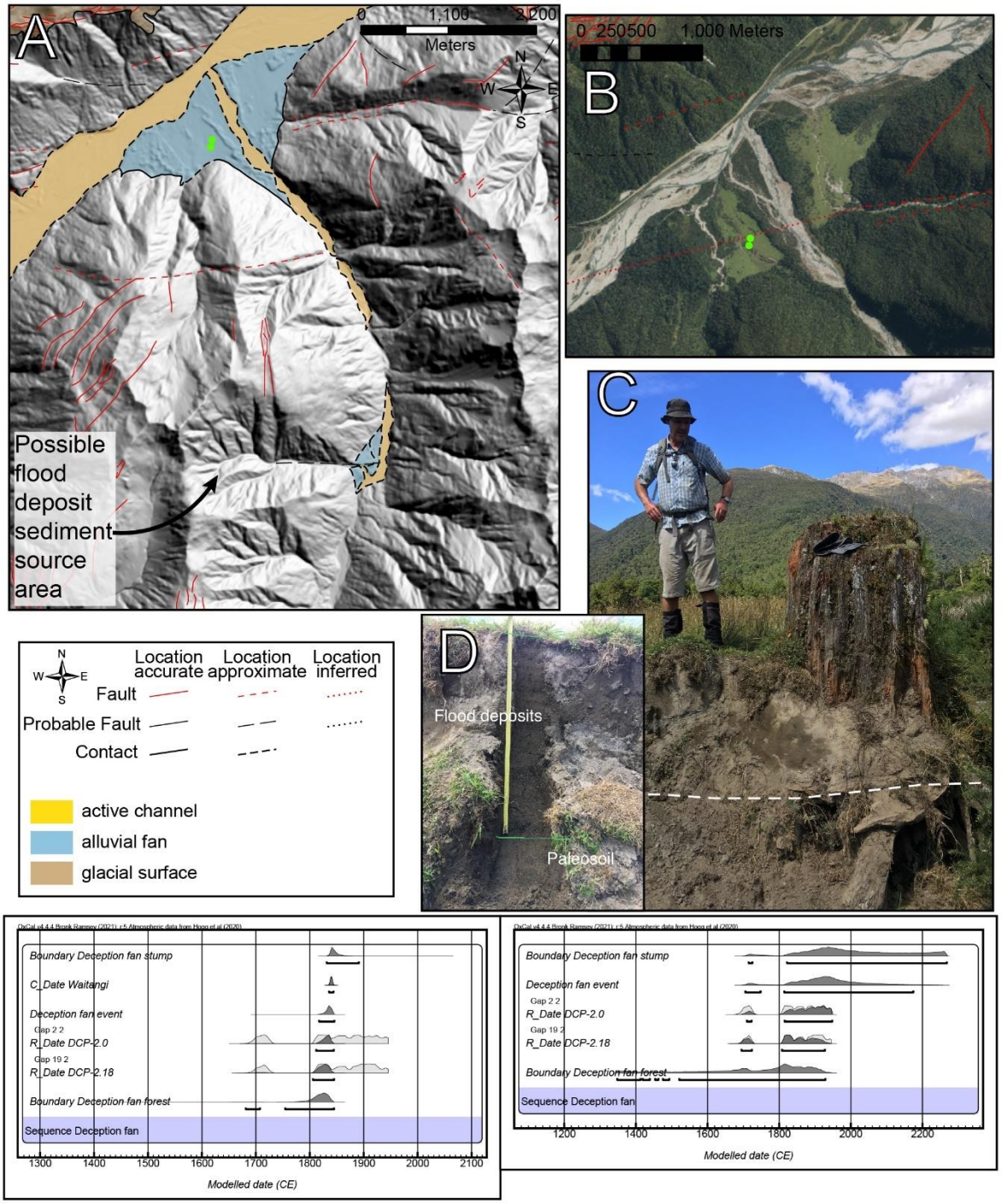

Figure D.1. Deception River fan tree stump. A) Geomorphic and fault map of Deception River fan. Green dots are tree stumps sampled. B) Airphoto and fault map of the Deception River fan. Green dots are the sampled trees. C) Photo of tree stump and exposed roots in

stream cut bank. D) Annotated photo of sediments the tree in C is buried in. Flood deposits ~80cm thick overlie paleosol which the tree in C is rooted into. E) Tree death OxCal model with 1840 CE minimum age constraint. F) Tree death OxCal model with 1920 CE minimum age constraint.